Computational Imaging with the Human Brain

Gao Wang

Submitted in fulfilment of the requirements for the
Degree of Doctor of Philosophy

Extreme Light Group
School of Physics and Astronomy
College of Science and Engineering
University of Glasgow

Sep 2024

Abstract

Human augmentation, which involves enhancing cognitive and physical abilities as a natural extension of the human body, has been significantly advanced by Brain-Computer Interfaces (BCIs). This thesis explores BCI-based human augmentation, focusing on computational ghost imaging and developing a phenomenological brain model for Steady-State Visual Evoked Potentials (SSVEPs).

Initially, the concept of BCIs as a conduit for computational imaging is introduced, demonstrating the potential to integrate brain function with external silicon-based processing systems. A key example is the ghost imaging of a hidden scene using the human visual system in conjunction with an adaptive computational imaging scheme. This technique, known as projection pattern 'carving,' utilizes real-time brain feedback to modify light projector patterns, resulting in more efficient and higher-resolution imaging. This brain-computer connectivity represents a form of augmented human computation, potentially expanding the sensing range of human vision and offering new methodologies for studying the neurophysics of human perception. An illustrative experiment is presented, highlighting how image reconstruction quality can be influenced by simultaneous conscious processing and readout of perceived light intensities.

Subsequently, the thesis delves into the phenomenon of SSVEP, which has attracted attention across various fields including neuroscience and human augmentation. The analysis of SSVEP under multiple frequency stimuli, a complex task due to frequency intermodulation terms, is addressed by proposing a phenomenological model. This model provides a mathematical framework for analysing the essential frequency mixing features in SSVEP when exposed to multi-frequency stimuli. The analysis is extended to both narrowband and broadband categories using analytical and statistical methods. Experimental results confirm the model's accuracy, shedding light on the mathematical model behind SSVEP responses to multiple frequency stimuli and offering insights for practical applications and a deeper understanding of this phenomenon.

Addressing the neuromorphic aspect of SSVEP, the thesis discusses the extensive use of SSVEP in BCIs due to their stability and efficiency in connecting the computer and the brain using simple flickering light. Moving beyond prior research that focused on low-density frequency division multiplexing techniques, this work demonstrates the feasibility of efficiently encoding informa-

tion in SSVEPs through high-density frequency division multiplexing, involving hundreds of frequencies. The capability to transmit complete images from the computer to the brain/EEG read-out within a short timeframe is also illustrated. High-density frequency multiplexing enables the implementation of a photonic neural network that leverages SSVEPs for performing simple classification tasks, showcasing promising scalability through serial brain connectivity. This research opens innovative pathways in neural interfacing, with implications for assistive technologies and cognitive enhancement, significantly advancing human-machine interaction.

Lastly, the concept of SSVEPs is extended to multi-frequency light modulation, relying on the broadband scenario of the phenomenological brain model. The research demonstrates the brain's ability to support the SSVEP read-out transmitting image. When the bandwidth spans more than an octave, the higher harmonics and nonlinear mixing between signal pairs overlap with the fundamental harmonics, creating a highly complex EEG signal. By utilizing a DNN trained on synthetic data, it is feasible to retrieve the original input signal, which can be employed to reconstruct images with each pixel encoded at a distinct single frequency. This approach facilitates precise image transmission, with each pixel encoded at a unique frequency. The BCI developed in this thesis enables multi-channel data transmission, and networked interfaces, and has potential applications in diagnostics, assistive technologies, and cognitive enhancement tools.

Contents

List of Figures

Acknowledgements

I would like to acknowledge Prof. Daniele Faccio for his supervisory guidance throughout the projects described in this thesis. I would also like to thank Dr. Giulia Marcucci, Dr Maria Chiara Braidotti for their collaboration and guidance.

I would like to acknowledge the support of the China Scholarship Council (CSC).

Declaration

All work in this thesis was carried out by the author unless otherwise explicitly stated.

This study was conducted in accordance with ethical guidelines and approved by the Ethics Committee of the University of Glasgow (approval no. 300210003). Prior to their involvement in the experiments, all participants gave written informed consent. To ensure participant privacy and confidentiality, all collected data were anonymized and securely stored, with exclusive use for research purposes. The data collection involved multiple participants, including the author, who voluntarily participated in the study. Identical data collection and analysis protocols were rigorously applied across all datasets to minimize potential biases arising from the author's dual role as researcher and participant.

I confirm that AI tools, specifically ChatGPT and Grammarly, were utilized in the preparation of this thesis. These tools were employed to proofread and polish the language or generate suggestions for phrasing and formatting. The use of such tools was limited to enhancing clarity and coherence; no AI-generated content has been included without review and substantial modification to align with the research objectives and academic standards.

List of publications and proceedings

Published manuscripts:

- **G. Wang**, G. Marcucci, B. Peters, M. C. Braidotti, L. Muckli, and D. Faccio, "Human-centred physical neuromorphics with visual brain-computer interfaces," Nature Communication, vol. 15, no. 1, p. 6393, 2024.
- H. Zheng, Y. Han, L. Qiu, et al., "Long-range imaging lidar with multiple denoising technologies," Applied Sciences, vol. 14, no. 8, p. 3414, 2024.
- **G. Wang** and D. Faccio, "Computational Ghost Imaging with the Human Brain," Intell Comput, vol. 2, p. 0014, Jan. 2023.
- S. Zhang, H. Zheng, **G. Wang**, H. Chen, J. Liu, Y. Zhou, Y. He, S. Luo, Y. Liu, and Z. Xu, "Nth-order nonlinear intensity fluctuation amplifier," Optics Communications, vol. 514, p. 128124, Jul. 2022.
- S. Zhang, H. Zheng, **G. Wang**, H. Chen, Y. He, S. Luo, J. Liu, Y. Zhou, F. Li, and Z. Xu, "Identification and generation of different statistical distributions of light using Gamma modeling," EPL, vol. 137, no. 1, p. 11001, Jan. 2022.
- X. Sun, H. Chen, B. Qiu, **G. Wang**, W. Xu, S. Luo, Y. Yuan, B. Chen, H. Zheng, Y. He, and Z. Xu, "High-speed ghost imaging by an unpredictable optical phased array," Front. Phys., vol. 10, p. 1072482, Dec. 2022.

Published proceedings:

- **G. Wang** and D. Faccio, "Computational ghost imaging with the human brain," in Computational Optical Sensing and Imaging, Optica Publishing Group, 2022, CM3A–4.

Chapter 1

Introduction

The human brain possesses remarkable potential that can be harnessed to enhance human abilities. Over the past several decades, advancements in science and technology have significantly contributed to the field of human augmentation. This thesis explores the integration of cutting-edge technologies—such as computational imaging, neural networks, and analogue computing—into EEG signal processing to unlock the brain's full potential. Before delving into the technical details, the subsequent chapters will provide an overview of these methods and their applications.

1.1 Computational ghost imaging

Over the past few decades, there has been a significant evolution in the computational imaging field. It involves optical engineering, computer science, and signal processing. The main advance is to implement computational methods to enhance or reconstruct images beyond the capabilities of traditional imaging systems, which could improve imaging parameters like resolution, depth of field, dynamic range, and sensitivity. The field of computational imaging has been applied in many fields, including medical imaging, remote sensing, surveillance, scientific imaging, and entertainment. For example, techniques like HDR (High Dynamic Range) and panorama stitching rely on computational imaging in digital photography [5,6]. Techniques like MRI (Magnetic Resonance Imaging) and CT (Computed Tomography) scans use computational methods to reconstruct images from raw data in medical imaging [7,8]. It can be used to enhance images of distant celestial bodies in astronomy [9,10]. The increasing demand for higher-quality imaging drives it. Some key techniques in computational imaging include computational photography [11], light field imaging [12], compressive sensing [13], and phase retrieval [14]. These techniques involve advanced algorithms and mathematical models to process and reconstruct the acquired data to produce high-quality images.

Ghost imaging (GI), also known as correlation imaging, derives its name from its origins in quantum optics, where the technique was first introduced. GI is a method for reconstructing an image of an object by implementing correlations between light beams. Initially, it was demonstrated using quantum-entangled beams, showcasing the unique properties of quantum entanglement [15, 16].

Subsequent advancements revealed that classical light sources can also achieve GI. By employing classical light and computational techniques, researchers demonstrated that the method does not rely solely on quantum entanglement [17]. This finding enable various implementations based on classical correlations, significantly broadened the scope of GI.

While the term "ghost imaging" initially emphasized its connection to quantum entanglement phenomena, the evolution of the technology and its applications has led to a broader definition. It now encompasses a wider range of techniques leveraging light beam correlations, including the development of computational ghost imaging (CGI) [18].

GI typically consists of two processes: 1) illuminating an object with light whose intensity varies temporally and spatially; 2) collecting all the light reflected or transmitted from the object. In the first process, to achieve GI, knowledge of the temporal and spatial variations of the illumination is essential, particularly in scenarios involving external sources of patterns or modulations, such as thermal light. In such cases, a CCD camera is typically required to record the patterns generated by the illumination. Alternatively, in scenarios where the patterns are deterministically chosen by the user, the illumination can be precisely controlled, and the patterns are known a prior, like CGI. This approach eliminates the need to measure the patterns directly, as their structure is predefined and computationally accessible. In the second process, after the modulated light field is modulated by the object, the reflected or transmitted light from the object is measured by a “bucket” detector that has no spatial resolution. Even though information from the bucket detector does not yield an image, the image can be obtained by cross-correlating signals from the bucket detector and the illuminating patterns. Due to its novel physical peculiarities and its potential applications in practice, more and more attention has been paid to GI [19–27]. GI is a technique that utilizes the intensity correlation of light fields to acquire scene information. It has a simple structure and high detection efficiency, which make it applicable in various fields.

In space remote sensing, GI proves crucial by capturing two-dimensional spatial Fourier transforms of objects with single-pixel detectors, maintaining robust imaging performance even under challenging conditions such as atmospheric turbulence, background radiation, and photodetector noise [28]. For optical encryption and secure transmission, GI enhances optical security through the creation of larger cryptographic key spaces, contributing to more secure communication [29]. In medical imaging, GI offers significant potential, especially in low-dose radiation scenarios. High-resolution imaging using pseudo-thermal light is particularly promising for applications

where minimizing exposure is critical [30]. Lidar systems benefit from GI's capabilities in detecting and identifying high-speed moving targets, offering long-range and high-resolution performance suitable for advanced detection applications [31]. In the domain of acoustic imaging, GI has been extended to utilize correlations in random acoustic patterns, enabling high-speed and high-resolution imaging while requiring fewer computational resources [32]. For 3D optical security, GI leverages random phase masks to generate larger key spaces in three-dimensional particle-like distributions, opening new avenues for secure optical data protection [29]. Real-time imaging systems have become feasible through Instant Ghost Imaging (IGI), which enables real-time image reconstruction using differential algorithms and high-speed chips, eliminating the need for offline processing and making it ideal for immediate applications. GI has also shown promise in imaging through scattering media, where deep learning methods improve imaging quality, addressing challenges in real-world scenarios involving strong scattering [33]. Lastly, in quantum microscopy, GI exhibits unique capabilities for optical measurements, such as capturing entangled light through dual imaging detectors, highlighting its advanced potential in quantum-based imaging technologies [34].

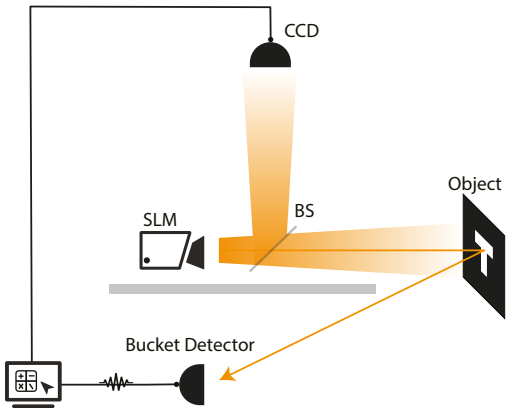

Figure 1.1: Setup for Ghost Imaging, referring the use of two detectors.

A basic GI setup is illustrated in Fig. 1.1. A spatial light modulator (SLM) projects structured/random patterns onto the object in this configuration. A reference beam, split from the main beam by a beam splitter (BS), is sampled by a spatial detector, such as a CCD camera. Meanwhile, a bucket detector collects the reflected or transmitted light from the object without spatial resolution. The object can then be reconstructed by calculating the intensity correlations between the signals recorded by the two detectors.

To simplify the basic GI setup, CGI was proposed [35], as illustrated in Fig. 1.2. In this approach, the reference beam is removed and replaced by a computational method. Meanwhile, a bucket detector collects the reflected or transmitted light from the object without spatial resolution. The object is then reconstructed by calculating the intensity correlations between the bucket detector signals and the computationally generated patterns.

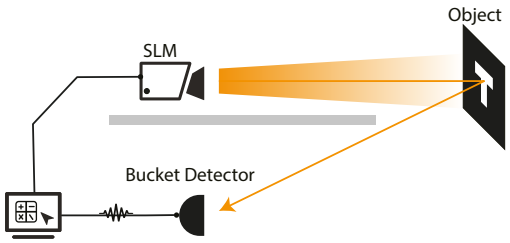

Figure 1.2: Setup for Computational Ghost Imaging: A single-pixel imaging system based on structured illumination [1].

CGI uses a light source to project a series of typically binary patterns, P_n. These are reflected from the object and collected by a bucket detector (a_n), which measures light intensity. Summing all weighted bucket values produces an image: $O = \sum a_n P_n$. This represents a computational imaging approach to the mathematical decomposition of an image into a basis of patterns P. Hadamard matrices (H) are commonly used as these patterns can be recursively defined.

In deterministic computational imaging approaches, the choice of patterns can indeed have important implications for the performance and efficiency of the system. Several properties of the patterns used for imaging are critical, such as orthogonality, compression, and adaptivity properties:

- **Orthogonality:** The patterns used in deterministic imaging are often required to be orthogonal to each other. Orthogonal patterns (e.g., after subtraction of a bias) allow for more efficient reconstruction of the object as the information captured by each pattern is independent. The reconstruction process benefits from a clearer separation of the contributions of each pattern, leading to better image quality [36].

- **Compression:** Efficient compression can reduce the amount of data needed to capture the object's image, which is especially important in cases of limited bandwidth or storage. Compression techniques can be particularly beneficial in systems using patterns that cover a large space or are computationally intensive. For instance, patterns with sparse or low-rank structures may help reduce the amount of data required without sacrificing image quality [37].

- **Adaptivity:** using an adaptive scheme enables less measurement. For example, a promising strategy for adaptive compressive sensing suggests replacing the random speckle patterns by directly using the patterns that form the sparse basis [38]. In addition, an adaptive method adjusts the pattern according to the detected bucket values, thereby boosting the imaging speed [2].

Therefore, the choice of patterns in deterministic CGI should be made with careful consideration of these factors, which can impact both the quality of the reconstructed image and the efficiency

of the imaging system.

Moreover, with the development of computational imaging, several advanced imaging techniques and algorithms have emerged, such as single-pixel imaging, single-pixel camera, computational ghost imaging, and compressed sensing. However, it is important to distinguish. While these technologies are interconnected, each has its own distinct principles, application scenarios, and significant differences.

For single-pixel imaging systems, a common scanning strategy involves using a sequence of spatially resolved patterns to record intensity measurements based on the correlations between the patterns and the object or scene. This correlation measurement can be implemented in two distinct ways. First, a light modulator placed in the image plane of a camera lens can mask images of the scene, with the filtered intensities measured by a single-pixel detector. This approach is referred to as structured detection and is frequently applied in the field of single-pixel imaging or single-pixel cameras [39]. Alternatively, the light modulator can project patterns onto the scene, with the single-pixel detector measuring the backscattered intensities. This method is known as structured illumination and is commonly employed in computational ghost imaging [1].

Although often treated as separate research fields, computational ghost imaging and single-pixel imaging are, from an optical perspective, fundamentally the same. Nonetheless, it remains practical to distinguish between the two: single-pixel imaging (or single-pixel cameras) typically employs structured detection and compressive sensing, while computational ghost imaging commonly utilizes structured illumination [1].

Compressed sensing is a new paradigm for data acquisition that allows certain signals and images to be reconstructed from far fewer samples or measurements than traditional methods require [40]. The highlight is the ability to simultaneously perform signal acquisition and data compression, thereby capturing information comparable to large arrays while using smaller, cheaper, and lower-bandwidth components [41]. In single-pixel imaging, compressed sensing effectively processes data collected by a single-pixel detector to reconstruct the object image [42].

In the chapter 2, we demonstrated CGI protocol. Although the final readout is a single time-domain signal, we model the human head as a nonlinear bucket/single-pixel detector, with the eye functioning as a lens. Additionally, we intend to adapt the structured illumination pattern in real time based on the detection feedback instead of using structured detection.

Researchers have optimized GI over time using different light sources, detectors, and algorithms. Recent approaches leverage the human visual system for detection by exploiting retinal persistence to directly perform summation [43–45]. Pre-calculated weighted patterns are visualized at high rates so that the eye perceives them as an accumulated sum.

Beyond the optical domain, researchers have developed GI methods with X-rays [46, 47], atoms

[48] and electrons [49]. Moreover, many aspects have been improved. For example, boosting the imaging speed in physics hardware [50], improving the imaging quality in matrix analysis [51] or in the development of new ghost imaging algorithms [52] and even using it as a new tool to collect new insight into how the human brain works [2], using the human brain as a detector that involving the brain's state.

The typical GI system can normally be divided into three processes: illumination, detection, and image reconstruction (algorithm).

1.1.1 Illumination

Illumination is the primary process, which determines the way of detection and the algorithm for the image reconstruction. In the very beginning, entangled photons were employed as light sources [53]. In the following ten years, researchers debated whether a quantum source was necessary for GI. In 2004, GI was successfully reproduced with pseudo-thermal sources [54,55] and thermal light [56]. Since thermal sources are quite easy to prepare in the lab, people started to put effort into the application of GI for remote sensing. In addition, computational GI (CGI) was proposed by Shapiro [35], where the reference beam is replaced by a computed field pattern and thus the setup is further simplified. Starting at 2016, the group in which I have been working at in China, proposed a light source made of an LED array running at 100 MHz modulation rate, enabling high-speed ghost imaging [57, 58]. Apart from a variety of hardware for illumination, different types of illumination patterns have been studied and investigated. Besides the most widely-used random speckle patterns, Fourier-Transform [59] and Hadamard [60] are also popularly used, which can be combined with Fast Fourier transform (FFT) and Fast Walsh-Hadamard transform (FWHT). Recently, patterns inspired by wavelet transform were introduced into ghost imaging [51].

1.1.2 Detection

In the initial stage, ordinary commercial detectors were employed to simply measure the intensity or photon number of the light from an object, such as single-photon detectors, PMT, photodiodes, CCD and so on.The detection process is simpler than the illumination process. Usually, a bucket detector with a fast enough response time is good for a ghost imaging experiment. Along with the development of ghost imaging, different types of detection schemes have been created. For example, multiple bucket detectors configuration was used to obtain 3D information [61] or even 3D video [62] via shape-from-shading. By exploiting time of flight, ghost imaging was extended to a new type of radar [63, 64]. To implement high-speed imaging under low light levels, a single-photon detector array with lens intensers was prepared [58]. Moreover, the first-photon detection scheme was introduced to increase the imaging efficiency for weak light scenarios [65]. Additionally, spatial ghost imaging has also been extended to time-varying objects [66, 67].

1.1.3 Reconstruction

For reconstructing the ghost imaging result, a simple correlation algorithm can be realised. However, to achieve a high standard of imaging, recently, more and more algorithms have been introduced into ghost imaging to increase the image quality and imaging speed.

In 2010, F. Ferri et al. introduced a differential ghost imaging (DGI) technique, which significantly improves the signal-to-noise ratio (SNR) of ghost imaging by effectively suppressing background noise. This approach allows for clearer reconstructions of the object, even in the presence of significant interference [68]. The key innovation of DGI is its ability to distinguish the object's signal from unwanted background, which is especially useful in environments with substantial noise or when weak signals need to be detected.

In 2012, B. Sun et al. presented an experimental comparison between various iterative ghost imaging algorithms, with a focus on a normalized weighting algorithm, called normalized GI (NGI). Their work demonstrated that NGI could achieve performance levels comparable to DGI, especially in terms of enhancing SNR and improving image reconstruction quality under noisy conditions [69]. NGI applies a normalization technique to the iterative reconstruction process, ensuring that the most informative patterns are given higher importance, thereby optimizing the reconstruction accuracy without the need for complex modifications to the imaging setup [69].

Building upon these advancements, in 2014, Xu-Ri Yao et al. introduced a novel technique for denoising ghost images, called iterative denoising of ghost imaging (IDGI) [70]. IDGI extends the concept of iterative processing by focusing on reducing noise throughout the reconstruction process, ensuring that the final image is not only free from background interference but also retains high clarity despite the presence of noise. This technique further refines the ghost imaging process by integrating denoising into the iterative framework, enhancing its robustness in real-world applications where noise levels can fluctuate and are often unpredictable. These three methods—DGI, NGI, and IDGI—share the common goal of improving the robustness of ghost imaging in practical scenarios, especially in situations where noise and background interference are significant challenges. By leveraging advanced computational techniques, such as background suppression, iterative reconstruction, and denoising, these algorithms make ghost imaging more reliable and applicable to a wider range of environments. Together, they represent significant steps forward in making ghost imaging more effective in both laboratory and real-world conditions, particularly when dealing with complex imaging environments.

Moreover, Katz et al. proposed a compressive sensing computational ghost imaging(CSGI) scheme based on a compressive sensing technique, which reduced the required acquisition samples significantly [13]. The key advantage of CSGI lies in its ability to achieve high-quality reconstructions with fewer pattern measurements, which can lead to faster data acquisition and lower computational costs. By leveraging the inherent structure of the object being imaged, com-

pressive sensing makes it possible to capture the essential features of the image from a smaller subset of patterns, thus improving the efficiency of the imaging process. This technique is particularly beneficial in applications where time or resources are limited, and it has opened up new possibilities for faster and more efficient ghost imaging systems.

In recent years, many advanced algorithms for imaging quality enhancement have been proposed [52,71–73], with a particular focus on deep learning-based techniques [72,73]. These algorithms have significantly improved the performance of ghost imaging systems, enabling more accurate and faster image reconstructions under a variety of conditions. Among the various approaches, deep learning has emerged as a powerful tool for enhancing imaging quality by learning complex mappings between input patterns and the reconstructed object from large datasets.

Deep learning, particularly convolutional neural networks (CNNs), have been shown to outperform traditional computational methods in terms of both accuracy and efficiency [52,71]. These models can automatically learn and extract features from data, bypassing the need for handcrafted image reconstruction algorithms. The application of deep learning to ghost imaging has led to improved robustness against noise, reduced reconstruction time, and the ability to recover high-quality images even in low-light or noisy environments. This trend reflects the growing importance of AI-driven techniques in the field of computational imaging, as they continue to push the boundaries of what is possible in real-time imaging applications.

1.2 Deep Neural network

Neural networks are a class of artificial intelligence designed to mimic the structure and function of the human brain. They possess remarkable capabilities for solving complex tasks such as classification, regression, and segmentation. Numerous neural network architectures have been proposed, but their fundamental building blocks consist of layers of interconnected nodes, or neurons, that process and transmit information in a manner similar to neurons in the human brain. Taking advantage of this, Deep neural networks (DNNs), characterized by their many layers, are particularly suited for tackling complex tasks. Empowered by the backpropagation theory, DNNs can efficiently learn and perform intricate operations. These networks have found applications in diverse fields [74], including image processing, signal processing, text analytics, and computational finance.

Making the most of DNN involves understanding how to train them, what applications they are suited for, and where to implement them. In the subsections below, we will introduce the foundational training algorithms, general use cases, and state-of-the-art hardware implementations.

1.2.1 Backpropagation Theory

Backpropagation (BP) theory is a fundamental learning algorithm in artificial neural networks (ANNs), primarily used to train multi-layer feedforward neural networks. This algorithm adjusts the weights and biases in the network by minimizing the error between the network's output and the expected output, thereby enabling the network to learn and make predictions from input data. The main concept of backpropagation involves using the gradient of the error, calculated via the chain rule, to determine the partial derivatives of the error with respect to the weights and biases of each layer. These derivatives are then used to iteratively update the weights and biases, reducing the overall error [75].

Since its introduction in 1986, the backpropagation algorithm has found widespread applications in various domains, including image compression, pattern recognition, time-series prediction, sequence recognition, and data filtering. It is capable of handling continuous data and differentiable functions across single-layer or multi-layer models [75]. Despite its effectiveness, the algorithm faces challenges such as slow convergence and susceptibility to local minima during training [76]. However, incorporating strategies like second-order methods and adaptive gain can significantly enhance its learning speed and accuracy [76, 77].

Research on backpropagation remains active, with ongoing efforts to refine the algorithm and expand its applications. For instance, combining the artificial bee colony algorithm with backpropagation neural networks improves the recognition capabilities of nonlinear models and the accuracy of inverted pendulum control [78]. Similarly, integrating an improved particle swarm optimization algorithm with backpropagation neural networks enhances the accuracy and stability of geological electromagnetic data inversion. Furthermore, backpropagation has demonstrated remarkable utility in high-resolution remote sensing image classification [79], CT image segmentation [80], and other fields, showcasing its robust learning capabilities and extensive application potential.

1.2.2 Signal Processing with DNN

Signal processing via DNN typically encompasses both spatial and temporal domains. The main focus in the spatial domain is image processing, while in the temporal domain, it is time Sequence Processing.

Image processing is a fundamental area in various fields, including computer vision, medical imaging, Lidar processing, and automated driving. Deep neural networks (DNNs) have significantly advanced this field, enabling a wide range of applications.

DNNs can approximate complex image processing tasks. For instance, a Multiscale Context Aggregation Network (CAN) has been used to produce deionized images [81,82], and Denoising

Convolutional Neural Networks (DnCNN) have been trained to remove noise and deblock JPEG images [83]. Additionally, deep learning-based style transfer [84, 85] has broadened the use of image processing techniques in the art field. For generating high-resolution images from low-resolution inputs, Very Deep Super-Resolution (VDSR) networks have been implemented with great success [86]. Furthermore, semantic segmentation techniques [87] have proven effective in processing multispectral images in remote sensing [88–90].

In the medical field, DNNs have greatly enhanced imaging techniques, improving diagnostic accuracy and speed. Examples include brain tumour segmentation [91], CT image denoising [92], and cell nuclei detection [93].

In the domain of automated driving, DNN-based semantic segmentation and vehicle detection using camera images have been standard practice for years [94, 95]. More recently, deep learning methods have advanced 3D Lidar processing, including semantic segmentation [96], object detection [97], and data augmentation [98], further accelerating developments in autonomous driving technologies.

Time sequence processing, a critical aspect of signal processing, encompasses various tasks including classification, regression, anomaly detection, and even specialized hardware implementation for AI systems.

Classification in time sequence processing involves mapping a sequence to a specific label, while regression is applied in various fields such as signal recovery [99], source separation [100], and denoising [101].

Beyond general signal processing, DNNs are also employed in specialized areas like audio processing, wireless communications, and radar systems.

In audio processing, for instance, deep learning techniques have significantly enhanced human-computer interaction. Examples include Speaker Recognition [102], Speech Dereverberation [103], Speech Separation [104], Speech Denoising [105], Speech Enhancement [106], and Speech-to-Text Transcription [107].

1.2.3 Hardware Implementation

The development and optimization of AI systems necessitate specialized hardware implementations. As artificial intelligence technology rapidly advances, so does the demand for computational power, driving the development and application of tailored hardware solutions. This section highlights the applications and advantages of various types of specialized hardware in AI systems based on available research.

Tensor Processing Units (TPUs): TPU is a specialized ASIC designed to accelerate the in-

ference phase of neural networks. Deployed in data centres since 2015, the TPU features a 65,536 8-bit MAC matrix multiplication unit capable of delivering up to 92 TeraOps/second peak throughput, complemented by a 28 MiB software-managed on-chip memory [108]. Its deterministic execution model caters to the stringent 99th percentile response time requirements of neural network applications, outperforming the time-varying optimizations of CPUs and GPUs. Despite its small size and low power consumption, the TPU achieves performance speeds approximately 15 to 30 times faster than contemporary GPUs or CPUs, with a TOPS/Watt efficiency that is 30 to 80 times higher [108].

Field Programmable Gate Arrays (FPGAs): FPGAs offer adaptability and customized hardware efficiency critical for AI applications. While FPGA designs require deep hardware expertise and face challenges such as lengthy compilation and debugging times, these barriers can be mitigated by enabling developers to write AI algorithms in high-level programming languages. These high-level codes can then be compiled into instructions executable on AI-specific soft processors implemented on FPGAs, significantly improving accessibility for software-oriented AI developers [109].

Application-Specific Integrated Circuits (ASICs): ASICs are favoured for AI applications due to their low power consumption and cost advantages. Compared to GPUs and FPGAs, ASICs provide superior cost efficiency and energy savings while maintaining the flexibility needed for various AI algorithm implementations. Their design is particularly well-suited for large-scale AI deployments where power and cost efficiency are paramount [110].

Neuron Machines: Neuron machines represent specialized hardware architectures designed for neural network simulations, making them highly effective for neuromorphic computing. These systems consist of a digital hardware neuron implemented as a large-scale fine-grained pipeline circuit and a memory unit referred to as a network unit. By leveraging extensive pipelines and significant memory resources, neuron machines harness the inherent parallelism of neural networks while maintaining the flexibility of network topology [111].

In summary, neural networks have emerged as powerful tools for learning and prediction, becoming increasingly popular in recent years. They are particularly effective at handling complex, non-linear problems that are difficult to address using traditional algorithms. Additionally, neural networks are driving innovations across various domains, contributing to the development of technologies such as virtual assistants, chatbots, and personalized medicine.

The rapid advancement of neural networks has been fuelled by the growing availability of data and computing power. As vast amounts of data are generated across fields ranging from healthcare to finance to social media, neural networks have proven indispensable for processing and analysing this information.

In this thesis, we demonstrate various applications of neural networks or DNN as a useful tool:

- In **Chapter 2**, a regression-based DNN is trained for reconstruction mapping and denoising tasks, showcasing its capability to extract meaningful information from noisy data.
- In **Chapter 4**, the mathematical model of the brain is leveraged to design convolution layers, resulting in both single-layer and double-layer neural network architectures tailored to specific classification tasks.
- In **Chapter 5**, a DNN is employed as a brain decoder to reconstruct information from brain signals, illustrating its potential for brain-computer interface applications.

These examples highlight the versatility and effectiveness of neural networks in addressing a range of challenges, further underscoring their importance in modern computational approaches.

1.3 Neuromorphic computing

Neural networks have been achieving remarkable achievements and breakthroughs. Yet, the development has not slowed down, and it persists as a dynamic field of research, offering continuous opportunities for comprehending optimal design and optimization across various applications. Moreover, in recent years, the expanding size of network models and datasets has heightened the computational power required for large-scale neural network calculations, especially, Large language models (LLM) [112]. The rapid evolution of information technology has concurrently intensified the need for increased efficiency and ultra-low power consumption within this domain. To overcome the challenge, many methods have been proposed, and one of them, called neuromorphic computing, has garnered extensive attention for its promising ability to process massive data with exceptionally low power consumption.

Neuromorphic computing is a new technology inspired by the brain to implement information processing within energy-efficient hardware. The general way to realize this is to map AI or neuroscience concepts to physical systems [113]. It has been successfully implemented onto different physical mechanism systems, such as magnetic, photonic, electronic, and more [114].

1.3.1 Physical Neural Networks

Physical Neural Networks (PNNs) aim to implement neural networks through hardware-based physical transformations. To be more specific, PNNs can be utilized for a variety of tasks, such as mathematical operations (e.g., accelerators) and physical information processing (e.g., in hardware neural networks or reservoirs). By leveraging hardware-based transformations, PNNs offer distinct advantages over conventional software-based neural networks:

- **Energy Efficiency**: PNNs operate with significantly lower power consumption by directly utilizing physical processes, eliminating the overhead associated with digital computation.
- **Parallelism**: They naturally support parallel processing, enabling faster execution of tasks such as classification, optimization, and signal processing.
- **Scalability**: By integrating multiple physical systems (e.g., human brains or other hardware), PNNs can dynamically scale to support distributed and collaborative computation.
- **Novel Computational Capabilities**: PNNs take advantage of the nonlinear and complex dynamics inherent in physical systems, offering the potential to solve problems that are inefficient or intractable for traditional digital implementations.

These advantages make PNNs a compelling alternative for applications that demand high efficiency, parallelism, and innovative computational approaches.

When focusing on the mathematical part realization, the physical system can be appropriately designed to execute trained DNN transformations, based on direct mathematical isomorphism. It implements the mathematical operations within the DNN via a physical system. It can also be called DNN 'accelerators' beyond conventional electronics for its energy-efficient and fast performing [115, 116].

When focusing on the physical processing part, trainable physical parameters can be incorporated, allowing for post-fabrication training [117]. Especially, the whole physical system is treated as a "black box" and then the software-based DNN in the computer is trained by an input-output dataset of this system, to guide the adjusting of the physical parameters via back-propagation algorithm.

1.3.2 Physical Reservoir Computing

PNN regards partial input as the adjustable/trainable parameters of the PNN, while physical reservoir computing uses a physical system as a computational resource only, with fixed parameters.

In Reservoir Computing (RC), it is a type of machine learning, that maps the input data into a high-dimensional spatiotemporal pattern via a fixed reservoir, followed by a final layer which is a full-connected layer with trainable weights as a readout. The reservoir is typically a large network of randomly connected artificial neurons, like recurrent neural networks. In short, it uses a fixed, randomly generated system called a "reservoir" to process data, like classification and regression.

As the simplicity of the training for RC, like ridge regression or gradient descent algorithm, has been rapidly improving in recent years because of its low training cost and real-time processing.

The realization of RC can not only be achieved via computer (called software-based computations) but also by a real physical system/device as a computational reservoir. Two methods were highlighted, one is using Physical Neural Networks directly as reservoirs and another is implementing dynamical systems.

For good implementation, normally four requirements for the reservoir are needed. High-dimension and non-linear mapping make sure the key features can be obtained. Short-term memory and robustness can ensure it focuses more on current input data as well as being insensitive to unessential small fluctuations, applying only to specific tasks (e.g., time-series prediction).

To take advantage of the physical system, many kinds of physical reservoirs have been proposed in recent years, for example, photonics [118–120], spintronics [121, 122], quantum dynamics [123,124], nanomaterials [125] reservoirs. In addition, analogue circuits and field programmable gate arrays [126,127], mechanics [128], fluids [129], and biological materials [130–132] has been also applied [133, 134].

1.4 Brain-computer interface

Neuromorphic computing draws inspiration from the brain's architecture and operational principles to develop hardware and algorithms that mimic neural processes, while Brain-Computer Interfaces (BCI) enable direct communication between the human brain and external devices by translating neural activity into actionable commands.

Brain-computer interface (BCI) technology [135] is a field of study that focuses on developing communication pathways between the brain and external devices, such as computers or prosthetic devices.

It is a trend that more and more artificial intelligence implemented into BCI system which uses sensors to measure brain activity (electrophysiological or hemodynamic) (electrophysiological or hemodynamic) [135], such as electroencephalography (EEG) or functional near-infrared spectroscopy (fNIRS), to translate that activity into control signals that can be used to operate a device or perform a specific task. Normally, electrophysiological or hemodynamic activities may be monitored.

Electrophysiological Electrophysiological activity refers to the electrical activity that occurs in living cells, generated by electro-chemical transmitters exchanging information between the neurons. It can be measured via Electrical or Magnetic field by electroencephalography (EEG), electrocorticography (ECoG), magnetoencephalography (MEG), and Intracortical Neuron recording – electrical signal acquisition in single neurons.

Hemodynamic The hemodynamic response is a series of physiological changes in blood cir-

culation that occur in response to neural activity in the brain. When neurons become active, they require more oxygen and nutrients to support their increased metabolic demands. It can be measured by Functional Magnetic Resonance Imaging (fMRI) and Near Infrared Spectroscopy (NIRS)

In summary for these brain activities, the detail is shown in the Table 1.1 [135].

Table 1.1: Summary of neuroimaging methods.

Method	Activity	Measure	Temporal	Spatial	Invasive	Portable
EEG	Electrical	Direct	∼0.05 s	∼10 mm	N	Y
MEG	Magnetic	Direct	∼0.05 s	∼5 mm	N	N
ECoG	Electrical	Direct	∼0.003 s	∼1 mm	Y	Y
Intracortical Neuron Recording	Electrical	Direct	∼0.003 s	∼0.5 mm (LFP) ∼0.1 mm (MUA) ∼0.05 mm (SUA)	Y	Y
fMRI	Metabolic	Indirect	∼1 s	∼1 mm	N	N
NIRS	Metabolic	Indirect	∼1 s	∼5 mm	N	Y

BCI technology has the potential to significantly enhance the quality of life for individuals with disabilities or medical conditions that limit their ability to communicate or control their environment. For example, BCIs can be used to control prosthetic limbs, allowing amputees to perform a range of tasks that were previously impossible.

In addition to medical applications, BCIs are also being explored for use in other fields, such as gaming and entertainment. For example, some video games are being developed that can be controlled using brain signals, allowing players to interact with the game in new and innovative ways.

Despite the potential benefits of BCI technology, there are still significant challenges to be addressed, such as improving the accuracy and speed of brain signal processing and developing devices that are comfortable and easy to use for extended periods. However, with continued advancements in technology and research, BCIs are expected to become an increasingly important tool for enhancing human communication and interaction with the world around us.

1.4.1 Electroencephalography

Electroencephalography (EEG), as a neuroimaging method, has already been applied in the BCI field, which aims to monitor the electrical activity on the scalp. Due to its high resolution in the time domain (around 0.05s), and low risk (Non-invasive), it has developed into a very portable way to monitor brain activity.

The EEG is recorded based on the International 10-20 system, which indicates the location of the electrodes [136].

As for the device components, there are four main items consisting of a standalone EEG device: electrodes, signal amplifiers, analog-to-digital converter (ADC), and logging device. Firstly, the EEG signal from the scalp is conducted into electrodes, and then it will go through the signal amplifier to enlarge the amplitude. After that, the amplified EEG signal can be converted to a digital signal by ADC more accurately. Lastly, the digitalized data will be logged into the storage device for future usage or just be put into computing for online processing. So, this is the basic data flow of the EEG.

In the frequency domain, EEG component can be divided into several frequency bands, including delta (δ)$\sim$(0.5-4 Hz), theta(θ)$\sim$(4-8 Hz), alpha (α)$\sim$(8-13 Hz), beta (β)$\sim$(14-30 Hz), and gamma (γ)$\sim$(>30 Hz) [137].

Event-related potentials (ERPs) are electrical signals generated by the brain in response to specific stimuli, such as sounds or visual cues. They are defined as time-locked electrical responses of the brain to specific sensory, cognitive, or motor events. These responses are typically characterized by distinct waveform components (e.g., P300, N400) that reflect different neural processes. ERPs are important tools in cognitive neuroscience and are used to study a wide range of cognitive processes, such as attention, memory, language, and perception. They can provide insights into how the brain processes information and how different brain regions work together to perform complex tasks. One of the key advantages of ERPs, as derived from EEG, is their millisecond-level temporal resolution, which allows researchers to track the timing of specific neural processes associated with cognitive or sensory events. This capability enables a detailed understanding of the temporal dynamics of brain activity during tasks like attention, decision-making, or perception.

Another advantage of using ERPs is that they leverage the non-invasive and cost-effective nature of EEG technology. Since ERPs are computed from EEG data, they share the same experimental accessibility, making them suitable for a wide range of settings without the need for expensive equipment like fMRI or PET scanners.

As a kind of ERPs, Visual Evoked Potentials (VEPs) are a kind of visual-related EEG signal created by brain activity, which is one main potential involved in this research. To be more specific, after being stimulated by visual signals, the activity of the visual cortex area will be modulated, which is also called brain activity modulation. More importantly, if the visual stimulus is getting closer to the central visual field, the voltage of VEPs will be larger. When it comes to stimulus, three main methods can be classified: morphology, frequency, and the field of visual stimulation [138]. In this research, the frequency of optical stimuli is the main focus. So, according to this, VEPs can be divided into two main types based on the frequency of visual stimulation, one is transient VEPs (TVEPs) with a frequency below 6 Hz, one is steady-state VEPs (SSVEP) with a frequency higher than 6 Hz [139, 140].

TVEPs are frequently used in three ways: flash TVEPs, pattern onset/offset TVEPs, and pattern reversal TVEPs. In detail, flash TVEPs show two peaks: negative peak (N2, around 90ms) and positive peak (P2, around 120ms); pattern onset/offset TVEPs show three peaks: positive peak (C1,75ms), negative peak (C2, 125ms), and positive peak (C3, 150ms); Pattern reversal TVEPs also show three peaks: negative peak (75ms), positive peak (100ms), and negative peak (135ms) [141].

Here, we will discuss the application of BCI control based on the VEP before introducing different types of VEP. The information transfer rate (ITR) is commonly used as a standard metric to evaluate the performance of BCI control systems. The ITR is defined as:

$$\mathrm{ITR} = \left(\log_2 N + P\log_2 P + (1-P)\log_2 \frac{1-P}{N-1}\right)\frac{60}{T} \tag{1.1}$$

Where: N is the number of classes, P is the accuracy, and T is the time in seconds required for one prediction. The unit of ITR is given in bits per minute (bit/min) [142, 143].

There are three main types of VEP modulations, distinguished by the nature of the stimulus and the characteristics of the evoked response: t-VEP, f-VEP, and c-VEP [135, 144]. The details are as follows:

- **t-VEP (Transient VEP)**
  - Relatively low information transfer rate (<30 bits/min)
  - Synchronous signal is necessary
  - No user training required
  - **Explanation:** t-VEP stands for Transient Visual Evoked Potential. In this type, the visual stimulus is presented as discrete, brief flashes. The evoked response is characterized by distinct, time-locked peaks following each stimulus. The response is usually measured in terms of latency and amplitude of these peaks.
- **f-VEP (Steady-State VEP)**
  - High information transfer rate (30–60 bits/min)
  - Simple system configuration
  - No user training required
  - More suitable for applications with few options
  - **Explanation:** f-VEP stands for Frequency-modulated Visual Evoked Potential. Here,

the visual stimulus is presented at a constant, repetitive frequency, leading to a continuous, sinusoidal evoked response that is synchronized with the frequency of the stimulus. The steady-state nature of the response allows for efficient signal detection and analysis.

- **c-VEP (Code-modulated VEP)**
  - Very high information transfer rate (>100 bits/min)
  - Synchronous signal is necessary
  - User training required
  - More suitable for applications with many options
  - **Explanation:** c-VEP stands for Code-modulated Visual Evoked Potential. This type uses a sequence of binary codes (e.g., m-sequences) to modulate the visual stimulus. The evoked response is a complex waveform that corresponds to the specific code sequence. The high complexity of c-VEPs enables very high information transfer rates, but it also requires the user to undergo training to achieve reliable signal interpretation.

While the c-VEP requires user training, t-VEP and f-VEP require no user training, which is an advantage. Besides, as f-VEP can achieve a higher information transfer rate than t-VEP, we prefer to use f-VEP, so-called Steady-state visually evoked potentials (SSVEPs), in the research. In practice, light-emitting diodes (LEDs), cathode-ray tube (CRT) monitors or liquid crystal displays (LCD) are normally used as stimulators to elicit SSVEP, and the user can gaze at the flashing stimuli that can be flashing digits or letters, to implement BCIs control or send commands to computer [145]. Besides, LED stimulators can be controlled independently for multiple targets application [146], so LED performs well for high complexity use, while LCD or CRT is for medium complexity use.

1.4.2 Steady-state visually evoked potentials

SSVEPs are electrical signals generated by the brain in response to visual stimuli that flicker at a specific frequency. These signals can be detected using electroencephalography (EEG), a non-invasive technique that records the electrical activity of the brain through electrodes placed on the scalp.

SSVEPs are similar to TVEPs but under a higher frequency (> 6 Hz). When it comes to flashing stimulus, SSVEP will present a sinusoidal-like waveform, with the same fundamental frequency. When it comes to reversal pattern stimulus, the SSVEP occurs at the reversal rate and their harmonics [147]. In contrast to TVEP, the amplitude and phase of constituent discrete frequency

components can keep for over long periods [148]like, 50 s or 100 s [149]. The artefacts produced by blinks and eye movements [150], as well as electromyographic noise contamination [151], can less influence the SSVEPs but may significantly affect the TVEPs. Therefore, TVEPs are not typically used for BCI and this is the reason why we chose SSVEP.

SSVEPs are important tools in cognitive neuroscience and are used to study visual perception and attention. They have also gained increasing attention in the field of brain-computer interfaces (BCIs), as they can be used to control external devices, such as computers or robotic systems.

SSVEP-based BCIs work by presenting visual stimuli that flicker at different frequencies to the user, who is instructed to focus on the stimulus corresponding to a specific task or command. The user's brain generates SSVEPs in response to the flickering stimuli, and these signals can be detected by the EEG electrodes and used to control the external device.

One of the advantages of SSVEPs is their high signal-to-noise ratio, which allows for accurate detection and decoding of brain signals. They also have a relatively high information transfer rate, which makes them suitable for real-time control of external devices.

Despite their advantages, SSVEPs also have limitations. For example, they require a high level of user attention and can be affected by factors such as fatigue, distraction, and participant movement. Additionally, they have limited spatial resolution compared to other imaging techniques, such as fMRI or MEG. This is an area worth discussing separately. Beyond technical considerations (e.g., illumination schemes, detection rates), it would be valuable to explore how different stimulation schemes and approaches impact the participants of the experiment.

Overall, SSVEPs represent an important tool in cognitive neuroscience and have significant potential for applications in the field of BCIs. As technology continues to evolve, SSVEP-based BCIs are expected to become increasingly sophisticated and versatile and have the potential to significantly enhance human communication and interaction with the world around us.

1.4.3 Mechanism of Light-Induced EEG Responses

To provide a rigorous explanation accessible to a typical physicist, we discuss how changes in light illumination produce a chain of signals, starting from light incident upon the eye, passing through the pupil, transduced by the retina, and processed by the brain, ultimately leading to changes observable in EEG. Key factors such as pupil diameter, human visual system (HVS) adaptation, room illumination, photobleaching, and field-of-view control are detailed below.

1. Light Incident on the Eye and Pupil Dynamics: Light enters the eye through the cornea, passes through the pupil, and is focused by the lens onto the retina [152]. The pupil diameter, regulated by the iris muscles, plays a crucial role in controlling the amount of light entering

the eye, directly influencing the intensity and quality of light reaching the retina [153]. This adjustment ensures optimal operation of the visual system under varying illumination conditions.

2. Retinal Transduction and Neural Encoding: The retina, a thin membrane at the back of the eye, contains photoreceptors (rods and cones) responsible for converting light into neural signals [154]. Rods are highly sensitive to low-light (scotopic) conditions, while cones are active under bright (photopic) conditions and are responsible for colour vision [155]. This transduction process is supported by a complex network of retinal neurons that perform preliminary image processing and transmit signals to the brain via the optic nerve [156].

3. Visual Adaptation and Photobleaching: The HVS adapts to varying illumination levels through adjustments in photochemical reactions in the retina. During dark adaptation, photoreceptors regenerate light-sensitive pigments to enhance sensitivity to faint light. Conversely, exposure to intense light can cause photobleaching, where these pigments are temporarily depleted, reducing retinal sensitivity [157]. This adaptation plays a critical role in modulating the neural response to visual stimuli.

4. Room Illumination and Environmental Factors: Room illumination significantly influences the visual system's sensitivity and adaptation state. Optimal lighting conditions enhance visual performance, while suboptimal conditions may induce fatigue or impair perception [158]. Prolonged exposure to high-intensity light can exacerbate photobleaching effects, further affecting visual sensitivity [157].

5. Control of the Field of View: The illuminated field of view can be controlled using a uniform illumination scheme, such as the Ganzfeld technique, which ensures consistent light distribution across the visual field [159]. This approach minimizes variations in retinal responses due to uneven illumination, thereby enhancing the reproducibility of EEG measurements. However, in this thesis, we maintain the distance and area of the stimulus to ensure that the field of view for the stimulus remains consistent.

Impact on Results: The nonlinearities introduced by pupil dynamics, photopigment bleaching, and adaptation mechanisms may influence the amplitude and phase stability of SSVEP responses. For example, prolonged high-intensity stimulation might lead to reduced responsiveness due to photobleaching, while low-intensity stimuli might not sufficiently activate cone pathways. These effects were minimized by careful control of stimulus intensity, duration, and field-of-view uniformity. Nevertheless, future work should explore these nonlinearities in more detail to refine SSVEP-based applications.

In conclusion, the eye plays a dual role as both an extension of the brain and an adaptive filter, introducing nonlinearities into the SSVEP response. The chain of processes initiated by changes in light involves pupil regulation, retinal phototransduction, neural encoding, and environmental

influences such as illumination and photobleaching. These effects are vital considerations for experimental design and result interpretation in studies involving light-induced EEG responses.

1.5 Thesis Layout

Chapter 2: Computational Imaging and the Human Brain. This chapter explores the feasibility of using the human brain as a nonlinear detector, focusing on leveraging its linear range when possible. A computational imaging protocol is developed to enable computational tasks, with ghost imaging as a key demonstration. An adaptive algorithm is proposed to enhance imaging speed, while a trained DNN ensures effective denoising for improved imaging results. Furthermore, this chapter investigates how the brain state, particularly conscious and unconscious states, influences the quality of reconstructed images, offering a novel way to differentiate between these states.

Chapter 3: Brain Phenomenological Model. This chapter introduces a phenomenological model of the human brain, starting with the experimental setup. A frequency-sweeping experiment is presented to illustrate the brain's nonlinear effects, which induce harmonics. The chapter then examines multi-frequency input stimuli and develops mathematical formulations to explain the SSVEP spectrum in both narrowband and broadband scenarios.

Chapter 4: Human-Centred Physical Neuromorphics. Building on the brain phenomenological model, this chapter focuses on the narrowband scenario. It demonstrates how the intermodulation band of SSVEP can be used to implement convolution operations, enabling the construction of single-layer and double-layer neural networks. These networks are applied to classification tasks using the SSVEP spectrum. Additionally, the chapter examines how brain states, such as focus and disruption, influence classification performance.

Chapter 5: Image Transmission Through the Human Brain. This chapter presents an innovative method for image transmission via the human brain, utilizing a brain decoder based on the broadband phenomenological model. Handwritten images are used as input stimuli via frequency-division multiplexing (FDM). The resulting SSVEP responses are collected, and a DNN-based brain decoder, trained on synthetic data derived from the brain model, is employed to reconstruct the transmitted images.

Chapter 6: Conclusion. This chapter summarizes the key findings and contributions of the thesis, highlighting its implications and achievements.

Chapter 7: Limitations and Future Work. The final chapter discusses the limitations of the studies conducted in this thesis and proposes potential directions for future research.

Chapter 2

Computational ghost imaging with the human brain

2.1 Introduction

Neurotechnologies, particularly brain-computer interfaces (BCIs), offer promising pathways for enhancing human cognitive abilities, with potential applications ranging from decision-making to memory improvement [160–169].

One specific example of BCI technology is visual control, which typically relies on steady-state visual evoked potentials (SSVEPs). These potentials can be detected either through implanted electrodes or, more commonly, using electroencephalography (EEG) [146,170–172]. In this context, the visual system serves as both a sensor for the surrounding environment and a controller for the computer. SSVEPs are generated by periodically repeating illumination patterns or light modulations, usually within the frequency range of 3-4 Hz to 30-40 Hz, to induce a steady-state response in the brain. A notable feature of SSVEPs is their pronounced nonlinearity, especially, high-order harmonics, which manifests as multiple harmonics in the power spectrum [173–175].

This study explores the integration of BCIs, based on visually evoked brain responses, into computational imaging systems. Specifically, we investigate whether such integration can advance computational imaging techniques.

A key aspect of computational imaging and related techniques is their dependence on machine-based detection methods, such as cameras or single-pixel sensors, combined with computational algorithms to reconstruct scene images.

In this work, we propose an innovative approach to computational imaging using brain-computer interfaces. We introduce a ghost imaging protocol that utilizes light-intensity information re-

flected from a surface, which is detected as an SSVEP from the brain. This information is processed by a computer algorithm and an artificial neural network to reconstruct an image from the SSVEP power spectrum. The imaging process is further optimized by an adaptive computational loop, where the SSVEP signal guides the selection of appropriate illumination patterns for the scene being imaged. We present preliminary findings that the quality of reconstructed images can serve as an evaluative measure to discern between nonconscious processing of light intensity, as detected through EEG signals, and conscious processing. The participants actively engage by either verbally communicating or typing the perceived light intensity.

It will detail the stimulus and EEG setups, followed by an explanation of the general ghost imaging protocol. To address the limitations of previous methods, we also present an Adaptive Ghost Imaging Protocol, which offers improved speed and noise reduction. Additionally, we propose a new protocol for assessing brain states, termed the Conscious/Nonconscious Measurement Protocol.

2.1.1 Stimulus Setup

The stimulus is managed through a monitor or projector, utilizing the Psychophysics Toolbox Version 3 (PTB-3). PTB-3 is a freely available MATLAB toolbox designed for vision and neuroscience research. It offers the advantage of precise control over visual and auditory stimuli, facilitating their synthesis and presentation.

Monitor

Modulated light intensities are delivered either by a Digital Light Projector (DLP) or a standard Liquid Crystal Display (LCD) computer screen. For calibrating the SSVEP readout, the screen displays uniform greyscale intensities with alternating 'on' and 'off' states, creating a flickering stimulus with a square waveform, as shown in Fig. 2.1. The subject, wearing the EEG headset, observes the screen flashing at a fixed frequency ($f = 1/T$) and a duty cycle of 50%.

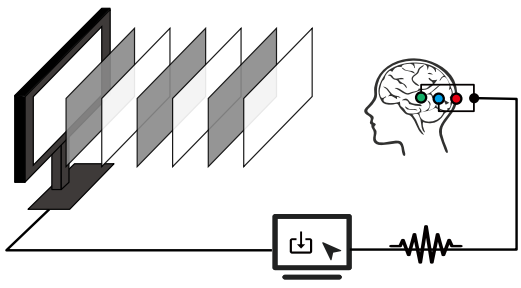

Figure 2.1: EEG system with LCD screen stimulus. Figure taken from Ref. [2]

Two key features must be considered: the frame rate (F_{rate}) of the screen, measured in frames per second (FPS), and the bit depth of the image. Typically, computer screens operate at a frame rate

of 60 Hz and an 8-bit intensity range. This allows for a flickering or flashing image frequency ranging from 0 to 30 Hz, with intensity levels spanning from 0 to 255. Mathematically, the parameters and flicker rate can be expressed as follows:

$$\begin{aligned} &I_{screen}[j] = A \times \text{Square}(2\pi f t[j], Duty); \\ &A \in \{0, 1, 2, 3, ..., 255\}; \\ &f = [3, F_{rate}/2); \\ &Duty = (0\%, 100\%); \\ &t[j] = j/F_{rate}; j \in \mathbb{W}; \end{aligned} \tag{2.1}$$

where A represents the illumination intensity, f denotes the flicker frequency, and $Duty$ is the duty cycle. The Square() function describes the square wave and $t[j]$ indicates the timestamp of each frame.

Additionally, accurate target identification in a time-domain visual evoked potential (t-VEP) BCI requires averaging over multiple epochs. To avoid overlap between consecutive t-VEPs, these BCIs generally operate at low stimulus rates (below 4 Hz). Although such low frequencies are necessary for t-VEP experiments, for the SSVEP experiment, the range $f = [3, F_{rate}/2)$ is employed in this context to differentiate between various stimuli.

DLP projector

It is similar to controlling a monitor, but with a slight difference, as a monitor typically uses an LCD, while a DLP system is based on a digital micromirror device (DMD) chip. Hence, the Tile-based intensity modulation was used here.

In a DLP-based projector, pulse-width modulation (PWM) is commonly used to adjust the intensity in 8-bit images, affecting the time-domain waveform of the stimulus. This work introduces an alternative approach, termed 'Tile-based intensity modulation,' which modulates intensity at the expense of resolution. As depicted in Fig. 2.2, each macro-pixel (or 'tile') within a 16×16 grid (the main image) is composed of 32×32 sub-pixels. The intensity of each macro-pixel is controlled by adjusting the percentage (p) of active pixels within the tile. For example, with $p = 0.5$, half of the total pixels in the tile are randomly selected and illuminated.

As illustrated in Fig. 2.2, this method allows a single tile macro-pixel to achieve 1025 distinct intensity values, ranging from 0 to 1024.

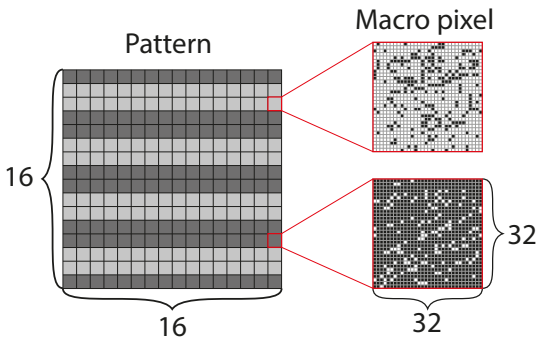

Figure 2.2: Tile macro-pixel modulation for the digital light projector (DLP). Each macro pixel in the 16×16 image array consists of 32×32 physical pixels in the DLP. The total number of physical pixels in each macro-pixel that are switched on, will determine the total luminosity of the macro-pixel with a range from 0 (no pixels on) to 1024 (all pixels on). Once the intensity and thus the total number of on-pixels is decided, these pixels are then chosen with a random pattern within the 32x32 macro-pixel array to avoid any possible aliasing or unwanted light patterning due to structure within the macro-pixel. Figure taken from Ref. [2]

2.1.2 EEG Setup

The EEG setup consists of three main elements: EEG click [3], 3D printed Electrodes and Analog-to-digital converter (ADC). The skull is attached to the 3D-printed electrodes and its signal is fed into the EEG click, namely an amplifier. Then the amplifier EEG signal is sampled by ADC and stored for further analysis.

EEG Click

EEG Click is a Click board™ designed for monitoring brain activity [3]. It amplifies faint electrical signals from the brain using a high-sensitivity circuit, allowing these signals to be sampled by a host microcontroller unit (MCU). An MCU is a compact integrated circuit designed to govern specific tasks in embedded systems, such as processing signals and controlling devices.

EEG Click employs the INA114, a precision instrumentation amplifier known for its very low offset voltage and high common mode rejection ratio. The INA114 provides sufficiently high gain while minimizing signal interference, ensuring accurate amplification of brain signals.

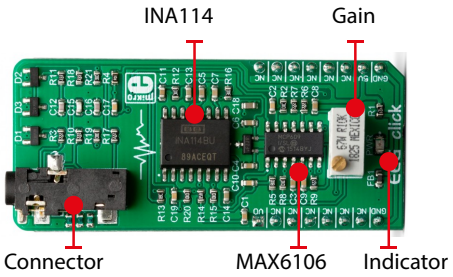

Figure 2.3: The layout of EEG click. Figure taken from Ref. [3]

This EEG click contains a 5V pin power supply, GND pin, and VO pin Readout. The VO pin is EEG signal OUT, ranging from 0V to 5V. The 3.5mm electrode connector is connected to the skull electrodes (3-electrode setup), which works as the input brain signal. 3-electrode setup is connected over a 3.5mm Jack connector on the Click, which is the activity electrode, reference electrode, and ground electrode.

Since the EEG signal fluctuates between positive and negative, so this device uses a virtual GND at the potential of 2.048V. The great advantage of this is to reduce the noise and improve the readout quality. The Gain Adjustment is to change the amplifier's gain.

3D printed Electrodes.

The electrode consisted of two main parts: 3D printed Holder and Sensor Felt. The 3D printed Holder is shown in Fig. 2.4(a), it is designed in FreeCAD and there are four holes around the object for faster air removal when adding the salt water. In the centre of the bottom is a hole to fix an M4 screw connecting with wire (or DuPont Line). The Sensor Felt needs to be filled into the Holder and the final eletrode is shown in Fig. 2.4(b). Before implementing it, it needs to be moistened with salt water for good conductivity. At the bottom of the electrode, a DuPont Line is connecting with the sensor felt via M4 screw and linking the sensor with the amplifier.

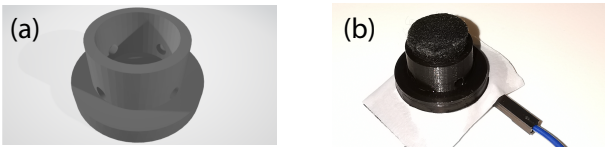

Figure 2.4: (a)3D printed electrodes Holder, (b)3D printed electrodes.

ADC Device

For ADC in the experiment, a standard computer sound card is used. This sound card, connected via the computer's input jack, serves as the ADC device. The microphone input of the sound card has a sample rate of up to 48 kHz with 16-bit depth. In the setup, the VO readout pin and GND pin from the EEG amplifier are connected to one channel of the sound card. It is important to note that the sound card's microphone input includes a high-pass filter, or AC coupling, which removes the DC component of the signal and ensures that only the AC components are sampled.

EEG Device.

A schematic overview is presented in Fig. 2.5. The setup employs a three-electrode EEG device, featuring a single active electrode placed at the Oz site (medial occipital electrode location) to capture SSVEP from the primary visual cortex Oz [171]. The EEG system also includes a reference electrode positioned above the left ear at the M1 location and a ground electrode situated

above the right ear at the M2 location. An audio cable leads the 3 pole signal into an amplifier

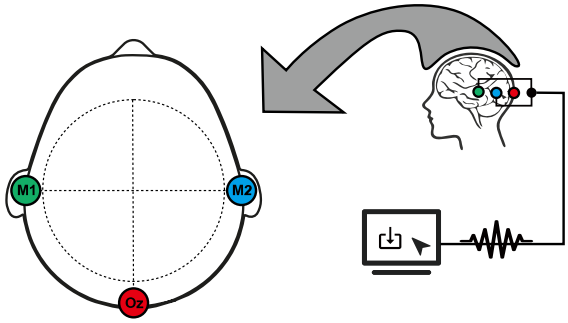

Figure 2.5: The layout of EEG recording system. Figure taken from Ref. [2]

before being imported into the microphone port of a computer which works as an EEG recorder.

EEG signal processing

The amplified SSVEP signal is sampled at 48 kHz and captured by directly connecting the electrode to the computer's sound card (Startech C-Media, ICUSBAUDIO). To reduce the amount of calculation, the signal is downsampled to 1 kHz and then processed with a bandstop filter (49 Hz-51 Hz) to remove common frequency noise.Fig. 2.6a) illustrates a typical SSVEP signal when the screen flashes at 12 Hz. The corresponding power spectral density (PSD) is shown in Fig. 2.6b), where distinct peaks are observed at the fundamental frequency (12 Hz), the second harmonic (24 Hz), and the third harmonic (36 Hz).

The SSVEP energy heatmap and calibration with three different people

The calibration curves from different people are shown in Fig. 2.8. All three graphs [(a), (b) and (c) refer to subjects 1, 2 and 3] have in common a series of features that despite the variation in terms of quantitative values, still allow us to define some general operating rules for computational ghost imaging with the brain. Specifically, all three show that at 15 Hz, the SSVEP increases monotonically for the intensity range used here. For 6 Hz modulation, all three SSVEP show a general trend to increase up to about one-third of the total illumination intensity and then show a decrease or non-monotonic dependence. For example, subject 2, (b), shows a monotonic increase up to higher light intensities. We conclude that a conservative approach of limiting light intensity to values corresponding to ~ 50 Lumens should guarantee a monotonic SSVEP dependence in most individuals.

This monotonic relationship is crucial because it ensures that the EEG readout intensity consistently corresponds to the light intensity, without ambiguity. In the context of data transmission, image processing, or other computational tasks described in this thesis, a monotonic or at least

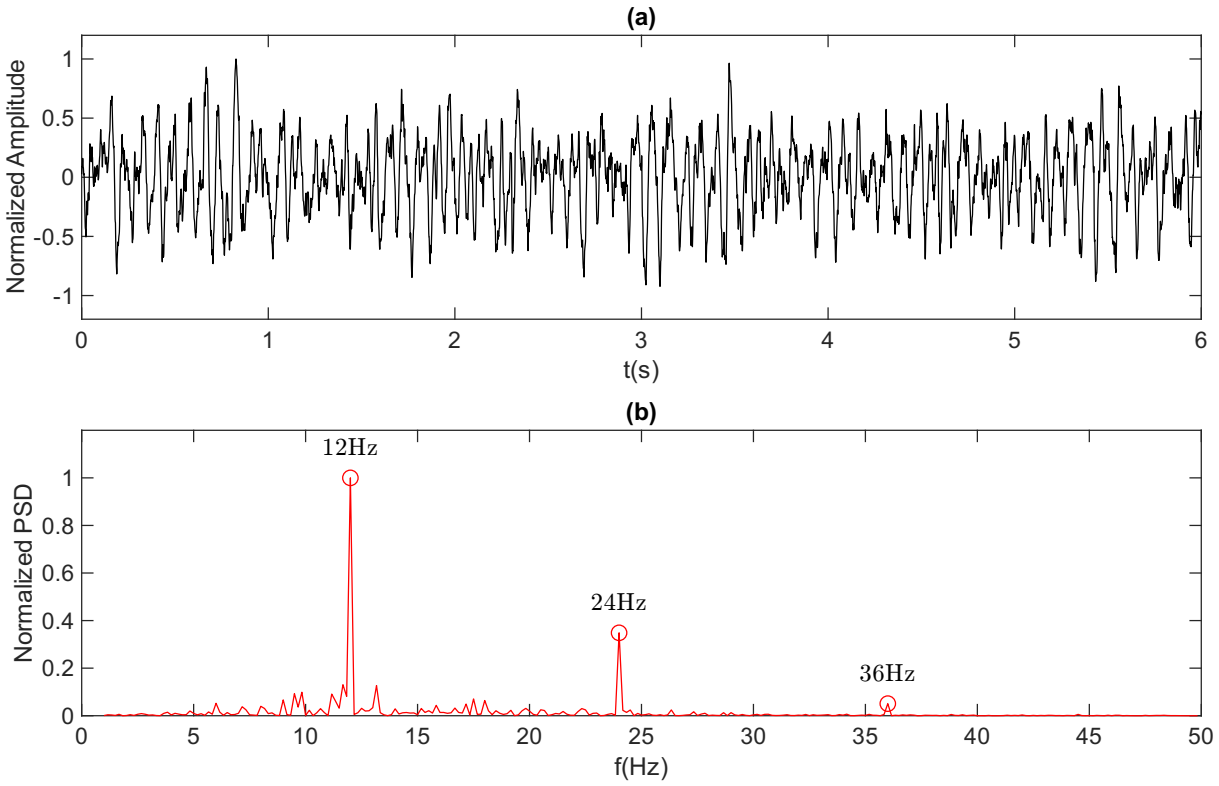

Figure 2.6: The waveform and PSD of a typical SSVEP signal under 12 Hz stimulus. a) is the waveform; b) is the power spectral density. Figure taken from Ref. [2]

a single-valued relationship between the emitted light intensity and the EEG response is essential. If the relationship were non-monotonic, the same EEG signal could correspond to different light intensities, leading to errors in interpretation and processing. This could compromise the accuracy and reliability of data transmission and processing tasks, as the system would struggle to decode the correct information from the EEG signals. Therefore, maintaining a monotonic relationship is key to achieving consistent and accurate results in applications relying on SSVEP-based BCIs.

A comprehensive study involving a larger and more statistically representative sample was beyond the scope of this work but will be addressed in future research.

2.1.3 Ghost Imaging with the brain

A schematic overview of the experiments is illustrated in Fig. 2.9. Using a standard DLP, we project a series of binary Hadamard patterns onto an object. The light that passes through the object is reflected off a secondary white surface (e.g., a white wall). Each binary pattern is alternately illuminated and extinguished at a frame rate within the 3-30 Hz range. We capture the SSVEP induced by visual cortex activity with a single electrode placed at O_z, the medial visual cortex region. This SSVEP is analysed in the spectral domain to extract both the fundamental

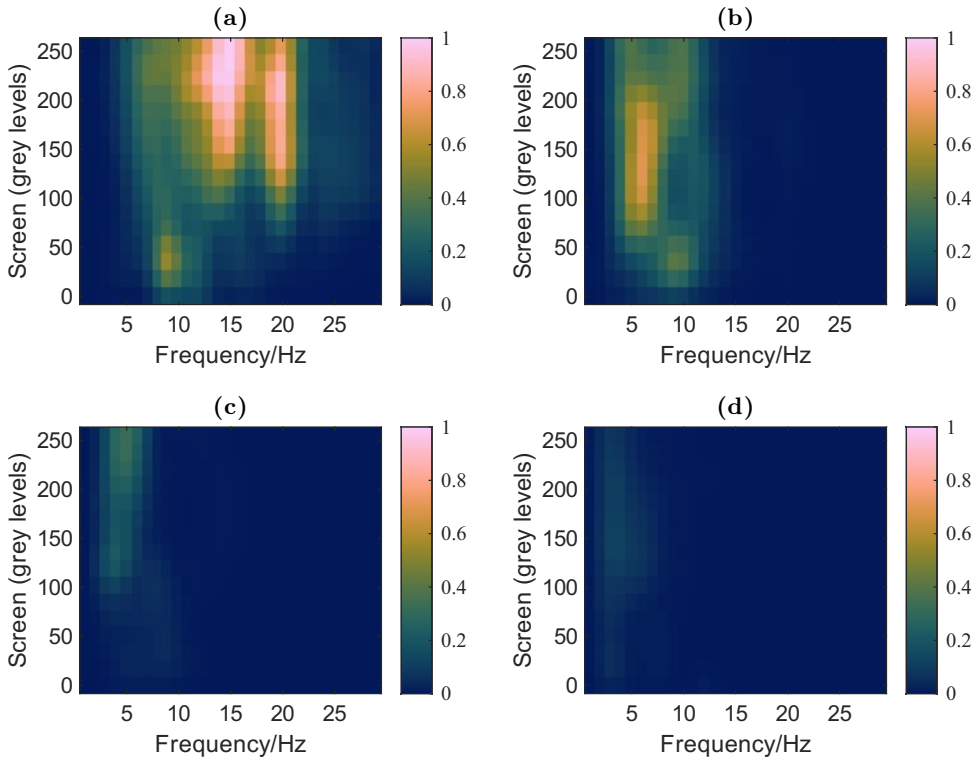

Figure 2.7: Measured SSVEP Harmonic heat maps for varying light modulation frequency and illumination for the, (a) fundamental, (b) second harmonic, (c) third harmonic and, (d) fourth harmonic. The SSVEP signals in all four figures are normalised to the maximum recorded value for the fundamental signal in **a**. Figure taken from Ref. [2].

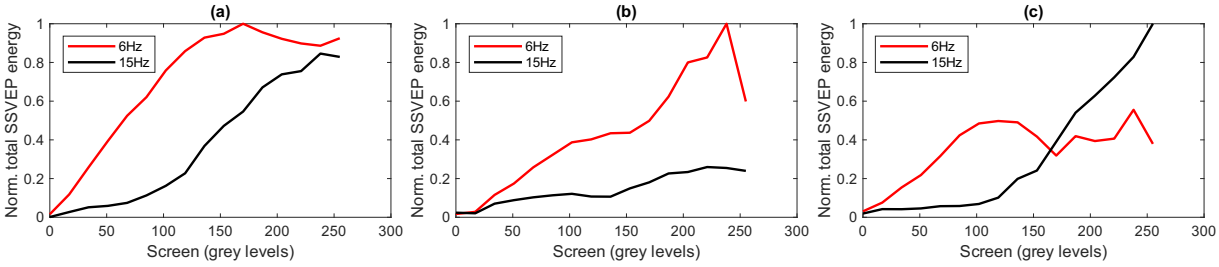

Figure 2.8: Measured total SSVEP energy at 6 Hz and 15 Hz from three subjects. Figure taken from Ref. [2]

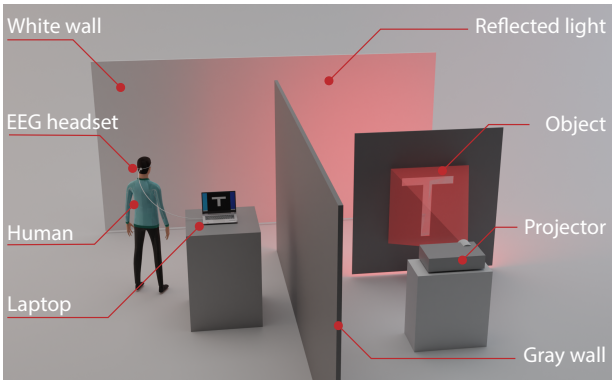

Figure 2.9: The setup used for adaptive ghost imaging. A light projector illuminates an object cut out from a cardboard support. Transmitted light is diffused by a ground glass that is in contact with the cardboard support and illuminates a white, observation wall. This part of the setup is obscured from the observer by a wall. The distance of both the object and the observer from this secondary wall is $\sim 0.5 - 1$ m. The EEG signal from the observer is recorded and processed on a computer. Figure taken from Ref. [2]

frequency (corresponding to the light modulation frequency) and higher harmonics (resulting from neuronal nonlinearity). These extracted components are then used to reconstruct an image of the object, which, as depicted in the schematic overview, is concealed behind a wall.

In the experiment, each column of the object is illuminated sequentially. For example, a single-column vector from the Hadamard matrix is used as a pattern to illuminate a horizontal pixel location on the object, starting from the left side. After projecting all Hadamard patterns at this initial horizontal position, we shift the projection one pixel to the right and repeat the sequence. This process is iteratively continued until the entire object has been fully scanned.

The initial step in any imaging process is the calibration of the detection system, which involves identifying the linear regions or, at the very least, the regions where the system response exhibits a monotonic relationship with increasing input intensity. This calibration is crucial for ensuring the accuracy and reliability of the imaging system.

In this case, the 'system' refers to the visual system and its SSVEP readout, which is known to exhibit notable nonlinearity. We characterized the (non)linearity of the SSVEP readout using a standard LCD screen. The screen displayed a flickering uniform intensity with frequencies ranging from 3 to 30 Hz, and the intensity was varied across the full 8-bit range of the screen, from 0 to 255. These values correspond to completely black (no light) and very bright (corresponding to 125 Lumens), respectively.

The EEG signal is analysed using a Fourier transform [176, 177], revealing clear harmonic peaks [171]. We then extract the maximum values of the individual harmonics (up to the fourth) and compute the total SSVEP energy, which is the sum of these values. The resulting SSVEP energy heatmap for each harmonic exhibits a complex and typically non-monotonic relationship with

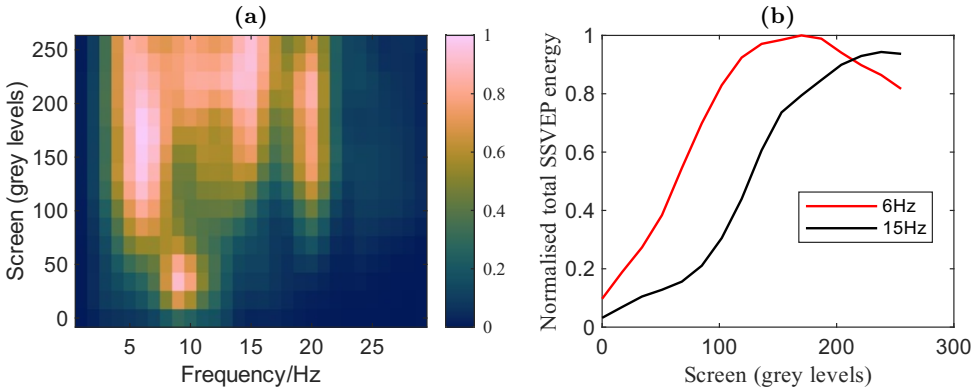

Figure 2.10: **(a)** Heatmap of the measured total SSVEP energy (sum of all harmonic peaks). **b** Total SSVEP energy at 6 Hz and 15 Hz. Figure taken from Ref. [2]

varying screen intensity and flicker frequency.

The SSVEP energy from different harmonics illustrates in Fig. 2.7. The origin of the 10 Hz signal observed under low illumination conditions in Fig. 2.7(a) and Fig. 2.7(b), as well as Figure 2.10(a), is attributed to the presence of an alpha wave peak at 10 Hz. When the light is weak, this alpha peak dominates. As shown in Figure 4.2(h), This figure presents the measured signal with the participant blindfolded (no stimulus), where only the alpha peak at 10 Hz is observable. This observation confirms that the recorded signals in other figures are authentically generated by the brain.

Moreover, the screen stimulus levels are labelled as grey levels rather than intensity to more accurately describe the stimulus properties. This change reflects that the displayed values correspond to the Digital Number (DN) or grey levels assigned to each pixel, which are proportional to, but not equivalent to, the actual light intensity. It is important to note that the relationship between the grey levels and the perceived intensity is influenced by various factors, including the gamma correction of the display screen. However, when it comes to DLP, we can solve this problem via tile macro-pixel modulation as shown in Fig. 2.2 and applied onto measuring calibration curve, as shown in Fig. 2.11.

While Fig. 2.7 illustrates the SSVEP energy from different harmonics, Fig. 2.10a illustrates the total SSVEP energy. Two optimal flicker frequency regions are identified: 6 Hz and 15 Hz, as shown in Fig. 2.10b. The 15 Hz region demonstrates a clear, monotonic increase in SSVEP energy with increasing illumination. Similarly, the 6 Hz region exhibits a monotonic increase, but only within a more restricted intensity range (from 0 to approximately 125 grey levels, or 0 to about 75 Lumens). Similar calibration measurements conducted across three different individuals showed consistent behaviour in Fig. 2.8. Consequently, most of our experiments are carried out at either 15 Hz (utilizing the full 0-125 Lumens intensity range) or 6 Hz (using a limited intensity range).

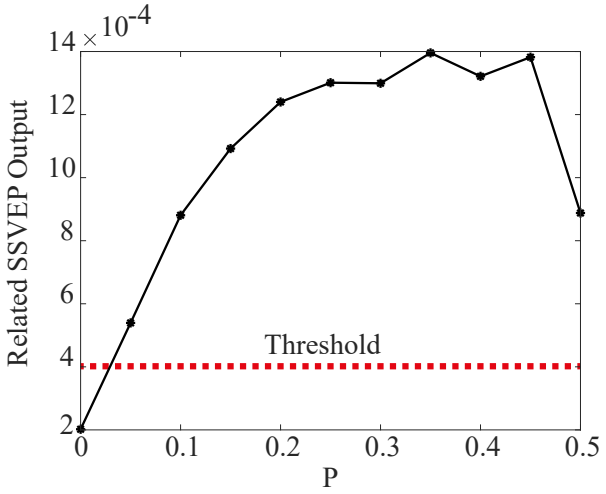

Figure 2.11: Total SSVEP energy (measured in arb. units) that is used as a calibration curve for adaptive feedback ghost imaging. The red dashed line indicates the threshold at which we attributed signals to be consistently above the noise level. This threshold is used in the Hadamard carving step to distinguish 'zero' SSVEP output (bucket) from non-zero values. Figure taken from Ref. [2]

2.1.4 Calibration of GI with the brain

When employing a digital light projector for computational ghost imaging, the same setup is used for both calibration and illumination of a target object. As described above, we vary the projected light intensity and monitor the output (SSVEP intensity) in order to verify a monotonic or close-to-linear response for the various objects we wish to illuminate.

In the calibration experiment, the projector is set to flash at a fixed frequency with varying intensities. Each illumination period lasts for 4 seconds, followed by a brief 0.5-second pause before the next illumination. The SSVEP is recorded during each illumination period to assess the brain's response.

The resulting calibration curve (In-Out intensity curve) is shown in Fig. 2.11.
A linear range is found for $0 < P \lesssim 0.3$. This linear range then guides the design of the patterns, which is used to re-scale and bias the binary patterns to ensure that the SSVEP is acquired in the linear range.
We also define a threshold that is used to distinguish whether the pattern has any overlap with the object. The threshold value in Fig. 2.11 is set to 4×10^{-4} and is determined by an empirical relationship that is based on our data and is described in more detail below.

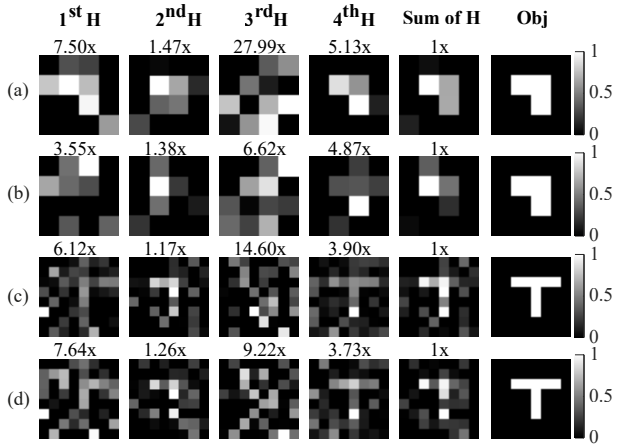

Figure 2.12: Standard ghost imaging results. (a) Inverted "L" shape (4 sec/pattern illumination time; total acquisition (illumination) time of 84 seconds). (b) Inverted "L" shape (2 sec/pattern illumination time; total acquisition time of 42 seconds). (c) Letter "T" (8 sec illumination time; total acquisition time of 512 seconds). (d) Letter "T" (4 sec illumination time; total acquisition time of 256 seconds). The columns, from left to right, show the ghost images that are reconstructed from the SSVEP fundamental (1^{st}H), second harmonic (2^{nd}H), third harmonic (3^{rd}H), fourth harmonic (4^{th}H) and total energy (sum over all 4 harmonics). The last column shows the ground truth object shape. Each image is normalised to the 'Sum of harmonics' total intensity (rescaling factors are shown above each image). Figure taken from Ref. [2]

2.1.5 GI results

Using the setup depicted in Fig. 2.9, objects are illuminated with Hadamard patterns, which are each periodically flickered. Figures 2.12(a) and (b) present results from the standard ghost imaging method applied to a 4×4 pixel object using a 6 Hz flicker frequency. The illumination times were 4 seconds and 2 seconds for each of the first 16 Hadamard patterns. The columns in these figures illustrate the ghost image reconstructions achieved with each individual harmonic SSVEP energy, as well as with the total energy (the sum of all harmonics).

Only the total SSVEP energy allows to reconstruction a clear image, in keeping with the calibration tests. More complicated images require more pixels. For example, Figs. 2.12(c) and (d) show the attempts to image the letter "T" on an 8×8 pixel grid. At 4 s illumination time (Fig. 2.12(d)), we obtain only a very noisy image. Increasing the illumination time to 8 s for each pattern (Fig. 2.12(c)), provides a marginally better image where the letter "T" is starting to emerge, hinting that significantly increasing illumination times could lead to better images. However, this strategy would lead to impractical experiment times that could then lead to other problems, including fatigue for the viewer.

2.2 Adaptive ghost imaging protocol

2.2.1 Image segmentation

In standard ghost imaging (GI), the image resolution is governed by the number of patterns used to illuminate the object. If t represents the acquisition time for each pattern, the total acquisition time is given by $T \propto N \times t$. This acquisition time t also influences the overall signal-to-noise ratio (SNR) of the final image.

Assuming a constant light source intensity and illumination area, an increase in the number of pixels N results in a decrease in the signal—specifically, the number of photons collected per pixel and, consequently, the SNR decreases inversely with N. To counteract this reduction in SNR, t must be increased proportionally to N. Thus, to maintain a consistent SNR as the number of pixels increases, the total acquisition time must scale as $T \propto N^2$. This relationship is elaborated further by Johnson et al. [178]. This implies that segmenting a higher-resolution image into q smaller sub-images, each of size N/q, offers a significant advantage. By doing so, a fixed SNR can be achieved with a total acquisition time of $T \propto q \times (N/q)^2 = N^2/q$.

Thus, in all our measurements, we illuminate the object one column or stripe at a time. Specifically, we project the column vectors of the Hadamard matrix as single-line patterns, which illuminate the object at a horizontal pixel location, starting from the left of the object. After projecting all patterns from the current set of Hadamard patterns (H_c) at this fixed horizontal position, we shift one pixel to the right and repeat the projection and scanning sequence. This process is iteratively continued until the entire object has been thoroughly scanned.

Hadamard matrices and image reconstruction. The Hadamard matrices, H_m are $2^m \times 2^m$ matrices that can be defined recursively:

$$H_m = \frac{1}{\sqrt{2}} \begin{pmatrix} H_{m-1} & H_{m-1} \\ H_{m-1} & -H_{m-1} \end{pmatrix}; H_0 = 1; \tag{2.2}$$

Hadamard patterns used in ghost imaging typically consist of binary values (0 and 1), as light intensities cannot be negative. Therefore, $\hat{H}_m$ matrices are employed, where any negative values in the original H_m matrices are replaced with zeros. The bucket value B measured by a standard bucket detector (or equivalently, in our work, by the human visual system) can be expressed as:

$$B_{N\times 1} = \hat{H}^T_{N\times N} \cdot O_{N\times 1}; \tag{2.3}$$

where $\hat{H}^T_{N\times N}$ is the transpose of the Hadamard pattern matrix and $\hat{H}_{N\times N}$ consist of N column vectors (patterns), namely, $\hat{H}_{N\times N} = [\hat{H}_1, \hat{H}_2, \ldots, \hat{H}_N]$.

Equation 2.3 can be inverted to reconstruct the object O from the measured bucket values by

multiplying to the left and right by $\hat{H}_{N\times N}$ and then inverting to obtain

$$O_{N\times 1} = (\hat{H}_{N\times N} \cdot \hat{H}^T_{N\times N})^{-1} \hat{H}_{N\times N} \cdot B_{N\times 1}. \tag{2.4}$$

If one uses the conventional Hadamard patterns with values of -1 and 1, then $(\hat{H}_{N\times N} \cdot \hat{H}^T_{N\times N})^{-1}$ simplifies to the identity matrix, leading to the standard reconstruction formula $O = \sum a_n H_n$, where a_n represents the components of the bucket vector B.

However, since we do not measure negative intensity values and instead redefine the Hadamard matrix by replacing negative values with zeros, we employ a more generalized formula for image reconstruction, as given by Eq. 2.4. This general formula, which is also provided in the main text, accounts for the redefined Hadamard matrix.

2.2.2 Hadamard matrix carving

N measurements (patterns) are necessary for standard GI, but this approach becomes impractical with increasing pixel count because the total acquisition time scales with N^2, as previously discussed. To address this issue, we introduce a "Hadamard matrix carving" method. This approach reduces the imaging time by dynamically carving (i.e., simplifying) the Hadamard matrix during the measurement phase.

Crucially, there is no need for prior knowledge of the object to select the necessary illumination patterns. The method adapts to the object automatically: for sparser objects, the parameter p increases, resulting in a shorter acquisition time. Thus, the technique dynamically optimizes the number of patterns based on the object's features.

The starting point is the standard Hadamard matrix, H, with N patterns. This is transformed to $H_c = RHC$, where the 'row carving matrix', R, and the 'column carving matrix', C, are diagonal matrices:

$$\begin{aligned} R_{i,i} &= \mathrm{U}(-H_{i,j}); \\ C_{i,i} &= \begin{cases} 0 & r(i) \le r(i-1) \\ 1 & otherwise \end{cases} \\ r(i) &= Rank((RH)_{:,1:i}); \end{aligned} \tag{2.5}$$

where $r(i)$ stand for the rank of the first i columns of the matrix and U is the unit step function: $\mathrm{U}(x) = \mathbf{1}_{x>0}$.

Beyond the formal definitions, the operations can be understood by following the work flow of the Hadamard matrix carving, shown in Fig. 2.13. This example explicitly works out, step by

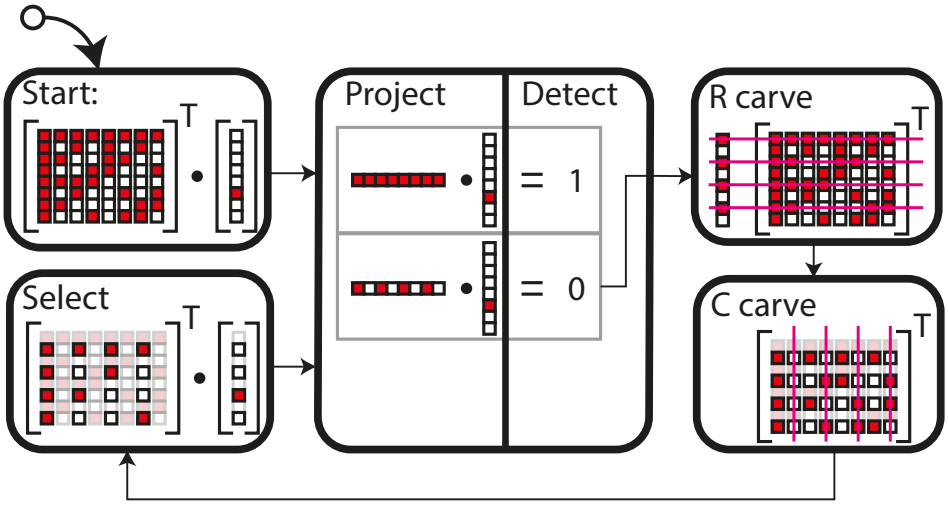

Figure 2.13: Flow chart with a worked-out example of Hadamard carving applied to the case $N = 8$. Figure taken from Ref. [2]

step, an example for the case $N = 8$.

The standard Hadamard matrix H, with each column representing an unwrapped Hadamard pattern (adjusted so that negative values are replaced with 0), is applied to the object, represented as an unwrapped single-column vector. We then project the first column of H onto the object. The result of the row-column multiplication provides a value indicating the overlap between the Hadamard pattern and the object. In practice, this value corresponds to the bucket measurement, which can be obtained using a photodiode or, in our case, by recording the SSVEP response from the human brain.

If this value is non-zero (indicating overlap), we retain the associated pattern. For instance, if the second column (transposed) multiplied by the object results in zero, there is no overlap, and we proceed to "carve" this pattern out of H , as the corresponding pixel locations are all set to zero, eliminating the need to project light onto them in subsequent projections. This is done by first performing "row carving," which involves removing all rows corresponding to non-zero elements in the pattern. The resulting matrix RH is no longer square and contains redundant columns. We then apply "column carving" C, where we calculate the rank by sequentially adding each column into consideration and remove columns that do not contribute to the rank. which reduces RH to a square matrix of rank $N/2$. The C operation involves retaining only those columns that contribute to increasing the matrix rank, and removing columns that do not. In the example shown in Fig. 2.13, the final rank of the carved matrix $H_c = RHC$ is $N/2 = 4$ after removing columns 2, 4, 6, and 8.

At this stage, the carved Hadamard matrix H_c is applied to the object once more, and the process is repeated. In the specific example provided, this results in a second carving process, reducing

the rank of the final carved H_c to $N/4 = 2$.

This example illustrates that the total reduction factor scales as 2^p, where each carving step reduces the rank by a factor of 2. The value of p depends on the specifics of the object being imaged. For instance, a uniform object that spans the entire field of view will overlap with all Hadamard patterns, resulting in $p = 0$ and no advantage from carving. Conversely, very sparse objects, such as a single pixel in the field of view, will have minimal overlap with most patterns, thereby maximizing p. As demonstrated in the main manuscript, this carving approach typically achieves a reduction in the number of patterns and thus in the total acquisition time by approximately $\sim 73\%$.

In practice, SSVEP measurements are influenced by noise, implementing a threshold to differentiate between bucket values that are zero (within the noise limit) and those that are greater than zero. This threshold, as described earlier, is determined during the calibration process.

An adaptive feedback loop is employed to dynamically adjust the projected Hadamard patterns during the measurement process, enhancing both imaging speed and image quality. The 'Hadamard matrix carving' method is employed as the underlying principle. This method is based on the observation that when projecting Hadamard (or other) patterns onto an object, not all patterns will exhibit significant overlap with the object. This allows for the dynamic adjustment of successive projections based on the observed overlap.

In brief, patterns are extracted from the Hadamard matrix H, where each column represents a Hadamard pattern vector of length N, the total number of pixels in the image. Consequently, H has a rank of N. These patterns (columns of H) are projected one at a time. When a bucket value measured falls below a certain threshold, it indicates minimal or no overlap between the pattern and the object. We then apply a 'row carving' operator, R, which removes all rows corresponding to the non-zero elements of the pattern. This results in a matrix with a reduced rank of $N/2$. Next, a 'column carving' operator, C, is applied to eliminate columns that do not contribute to increasing the matrix rank, yielding a new square, carved matrix $H_c = RHC$ with rank $N/2$. This process is repeated on the matrix H', with further carving applied each time a pattern shows no overlap with the object. Each iteration, triggered by the threshold, reduces the matrix rank by a factor of 2, thereby decreasing the number of required illumination patterns. Consequently, the final matrix H_c will contain $N/2^m$ patterns instead of N, resulting in a corresponding reduction in measurement time. The specific value of m and the extent of the measurement time reduction depend on the characteristics of the object being imaged. In general, sparse binary objects can lead to substantial reductions in both the number of patterns and the measurement time, as illustrated in the results below.

Noise distribution of the SSVEP energy. The Hadamard carving procedure requires determin-

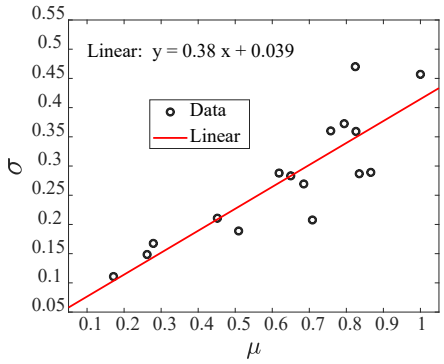

Figure 2.14: Plot showing the linear relationship between the mean (μ) and standard deviation (σ) of the SSVEP read-out.

ing if a pattern has a zero overlap with the object, i.e. if the measured intensity is also zero. However, in the presence of noise, we must instead determine a threshold value, below which we consider the measured signal to be zero. We therefore first characterised the actual noise present in the SSVEP measurements.
We repeated the calibration with the LCD screen 30 times. The average of the SSVEP read-out, μ, increases with light intensity up to around 150-grey levels (half maximum intensity) illumination, in agreement with Fig. 2(b) in the main text.

We also find that the noise standard deviation scales as $\sigma \sim 0.4\mu$, as shown in Fig. 2.14. We therefore use this scaling to model noise for the DNN synthetic data (see below).

Threshold relation. The threshold value for the experiments that are used to distinguish between "zero" and "non-zero" SSVEP output is given by $\mu_0 + 2\sigma$, where μ_0 is the SSVEP with zero illumination intensity and we use $\sigma = 0.5\mu_0$.

2.2.3 Image reconstruction

Several methods can be employed to reconstruct the final image. As noted, standard ghost imaging (GI), where the image is reconstructed as $O = \sum a_n H_n$, often results in noisy images. An alternative approach is to use the carving method described previously and reconstruct the image with $O = (H_c \cdot H_c^T)^{-1} \cdot H_c \cdot B$, where B represents the vector of all measured SSVEP values. Additionally, the patterns that were removed can be used as masks to indicate regions where the image is expected to have zero intensity. This 'carved ghost imaging' (CGI) technique significantly improves the image quality by reducing noise from pixels outside the object.

Finally, we implemented an end-to-end deep neural network (DNN-GI) for image reconstruction and denoising. The DNN consists of a linear layer trained to reconstruct the image based solely

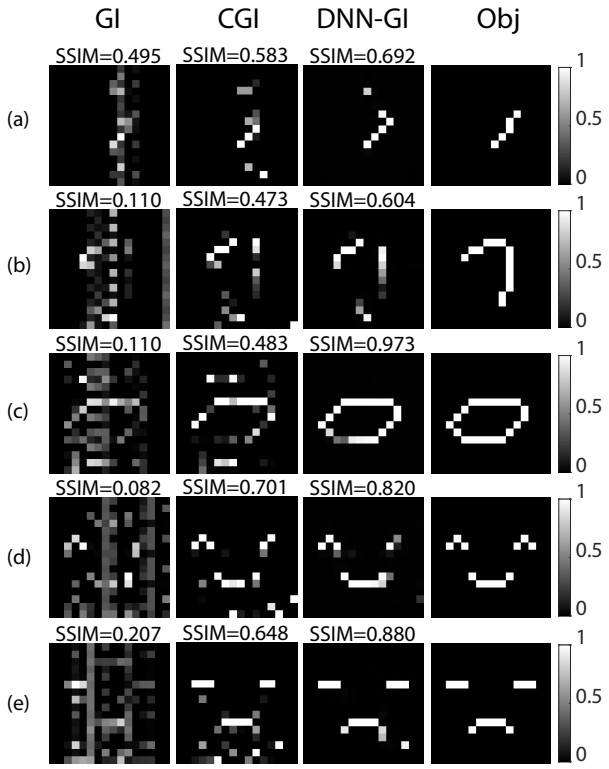

Figure 2.15: Adaptive feedback ghost imaging results. The four columns indicate results (from left to right) using the standard GI approach, carved GI (CGI), DNN GI reconstruction and the ground truth object. Row (a) is for the number "1" with 42 projected patterns; (b) for the number "7" with 60 patterns; Row (c) for the number "0" with 87 patterns; Row (d) for a smiley face with 74 patterns; and Row (e) for a sad face with 76 patterns. Figure taken from Ref. [2]

on the detected bucket (i.e., SSVEP) values, followed by a series of nonlinear layers for denoising [83].

Deep Neural Network ghost image (DNN-GI) reconstruction.

We implement an end-to-end deep neural network (DNN) for denoising, specifically the "denoising network" DnCCN, which is based on the architecture described in Ref. [83]. This DNN is a convolutional neural network (CNN) with 59 layers, and full details of its architecture can be found in Ref. [83]. Although originally designed for denoising noisy images, we apply transfer learning to this network to process a 16×16 matrix of SSVEP total energy values as input and produce a denoised image.

MNIST digit images are resized from 28×28 to 16×16 to match the dimensions of the images used in our experiments. These resized images are then used to simulate CGI on a computer, generating synthetic data. Noise is added to this data using the noise model described above. The resulting dataset is then used for training. Examples of reconstructed images are shown in Fig. 2.15. Rows (a) and (b) display examples of hand-written digits: a 1 and a 7, respectively. Rows (c), (d), and (e) present results similar to those shown in the main text, illustrating how the

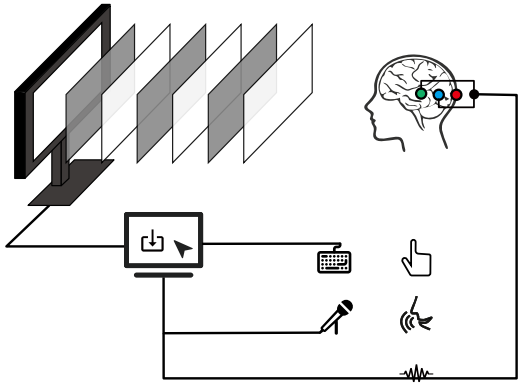

Figure 2.16: conscious/nonconscious (explicit/non-explicit) setup with LCD screen stimulus. The human actuator and the human EEG will be recorded as the response. Figure taken from Ref. [2]

imaging technique generalizes beyond the MNIST digits used for training the DNN.

In the experiment, objects are illuminated with 16×16 pixel Hadamard patterns, with each pattern having a 2 s illumination time and a flicker frequency of 6 Hz. After applying Hadamard carving as described, image reconstruction is performed using standard GI, carved GI, and DNN-GI methods. Fig. 2.15 illustrates the results obtained with these three approaches for three different examples: a geometric shape and two simplified face objects. The quality of image reconstruction is quantified using the Structural Similarity Index Measure (SSIM), which is indicated above each image. Carved GI (CGI), which uses carved patterns, shows improved performance over traditional GI, as the carved patterns effectively set parts of the background to zero, enhancing the overall image quality.

The best results are achieved with the DNN-GI method, owing to the additional noise reduction incorporated into the network structure. Notably, while the standard GI method often fails to reconstruct the image accurately, applying the DNN reconstruction after carving yields high-quality images and results in an average reduction of approximately 70% in the total number of patterns required.

For reference, the standard GI approach (first column in Fig. 2.12) required a rather prohibitive observation time for the full 256 pattern set of around $256 \times 2 \times (16/4)^2/60 = 137$ minutes for the digit "0" in row (a), whereas the CGI and DNN-GI approaches required a total of only $87 \times 2/60 = 3$ minutes.

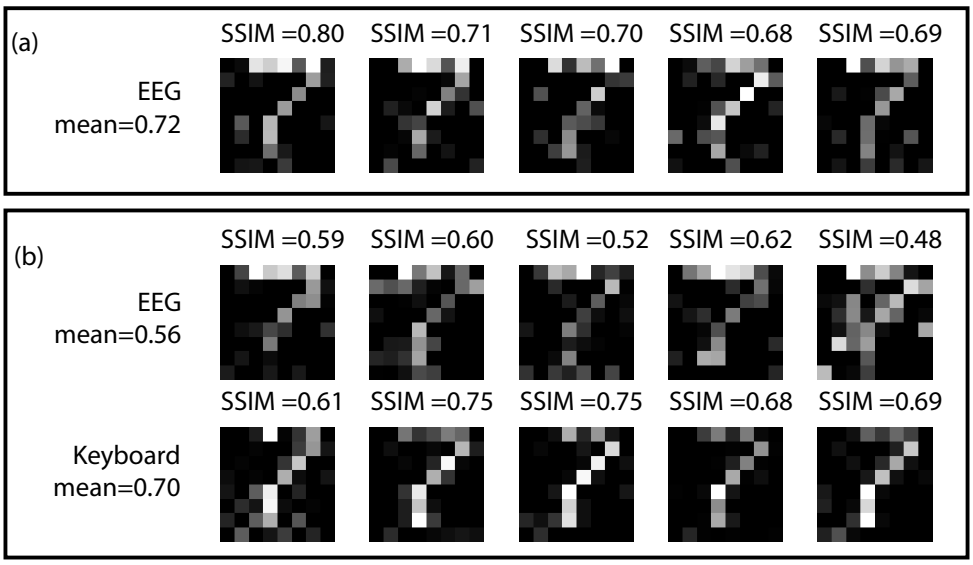

Figure 2.17: Nonconscious versus conscious ghost imaging: (a) shows 5 repetitions of 'standard' (full Hadamard pattern projection) ghost imaging of the digit "7" using only the EEG as a read-out. The mean SSIM across the 5 repetitions is 0.72. (b) shows the case for concomitant EEG read-out and conscious read-out in the form of perceived intensity values evaluated by the participant in the range 0-15 and then typed into a keyboard (without shifting eye contact from the screen). The 'conscious' processed information provides image quality similar to that of the EEG alone (mean SSIM = 0.70). However, the EEG reconstruction is now systematically worse and has a mean SSIM = 0.56, indicating an apparent interference between the conscious processing of the data and the EEG read-out from the visual cortex. Figure taken from Ref. [2]

2.3 Conscious/nonconscious measurement protocol

The conscious explicit response is the human actuator via keyboard or microphone while the nonconscious non-explicit response is the EEG read-out via EEG headset.

The experimental setup is illustrated in Fig. 2.16. Instead of applying a sweeping intensity with a 6 Hz flickering stimulus, the intensities are set to match the bucket values from the ghost imaging simulation, as described in Equation 2.3. In this simulation, an 8-by-8 object (digit "7") is used, resulting in 64 distinct intensity values. The subject, wearing the EEG headset, observes the screen and performs one of three tasks: EEG-only, EEG-Keyboard, or EEG-Mic.

In the EEG-only experiment, each flickering stimulus lasts for 2 seconds, with a 0.5-second interval between stimuli to minimize the other effects, like pupil diameter change. . In the EEG-Keyboard experiment, the subject is asked to type the perceived intensity, ranging from 0 to 15. In the EEG-Mic experiment, the subject is prompted to speak the perceived intensity within an additional 2 seconds to avoid the disruption caused by speaking. . The spoken responses are recorded and transcribed into numerical values (from 0 to 15) after the experiment.

The numerical inputs from the human actuator and the harmonic sum of the EEG-only readings

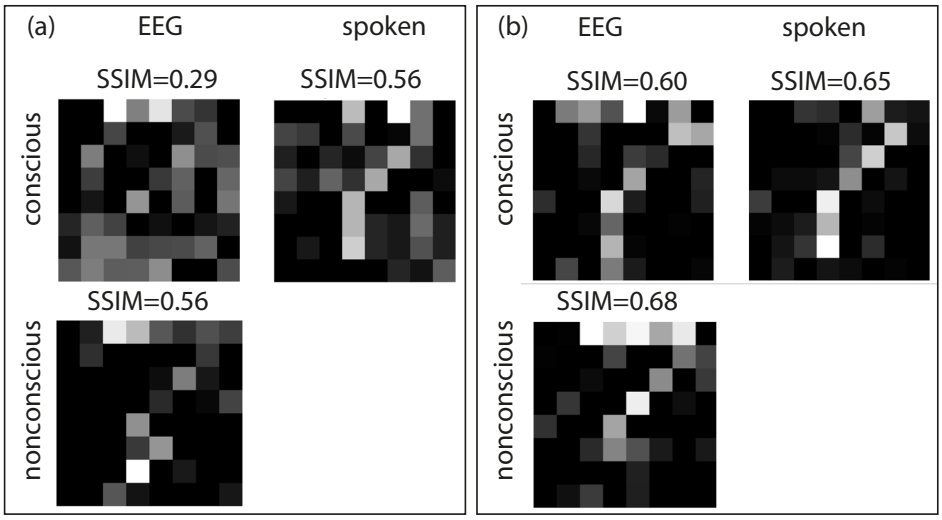

Figure 2.18: Nonconscious versus conscious (explicit) ghost imaging: (a) and (b) show the same experiment, repeated by two different subjects. Greyscale values corresponding to simulated ghost imaging bucket intensity values for the digit "7" are projected on a screen that is observed by the subject. Each experiment is then composed of two sessions. In one session (labelled as "nonconscious"), only the EEG readout is used to reconstruct the final ghost image. In the second session (labelled as "conscious"), the subject is asked to verbally communicate a numerical value between 0 and 15 that represents their estimate of the projected intensity. This is performed in parallel with an EEG recording, specifically, after each single illumination period and during the 2-second rest time before the next illumination). We then compare the ghost image retrieval using the verbally communicated values and the EEG readout. The "nonconscious" EEG ghost image and the "conscious" verbally communicated-values ghost image correspond well and have very similar SSIM. However, for both subjects, the EEG read-out ghost image deteriorates considerably in the "conscious" case, in agreement with other measurements shown in the main paper. Figure taken from Ref. [2]

are used as bucket values to reconstruct the object's image and estimate the SSIM for both conscious and nonconscious responses. Results for the case where the bucket values are typed on a keyboard are presented in the main paper. Fig. 2.18 shows additional results from the same test performed with two different subjects, where intensity values are communicated verbally instead. These results are compared to those obtained using EEG readout in ghost imaging. As observed in the previous one, the explicit verbal responses seem to interfere with the nonconscious EEG readout.

The added complexity of encoding images onto modulated light intensities, as performed in the ghost imaging protocol, provides significant advantages over simply measuring changes in the SSVEP.

The correlation-based reconstruction inherent to ghost imaging provides robustness to noise and artifacts. By integrating responses over multiple intensity-modulated patterns, the process inherently suppresses uncorrelated noise, thereby enhancing the reliability of the reconstructed image.

In contrast, SSVEP measurements can be more susceptible to interference from unrelated neural activities or environmental artifacts.

2.4 Conclusions

We have demonstrated that simple computational tasks can be performed using brain-computer connectivity. Specifically, we have explored a form of ghost imaging combined with an adaptive feedback approach that effectively 'carves' out low-signal illumination patterns. This method significantly reduces both illumination time and image noise. While the same approach could be applied with a conventional detector, our focus has been on utilizing SSVEP recordings to establish an adaptive computational imaging scheme where the brain serves as the sensor for image reconstruction. This work lays the groundwork for future research into alternative forms of computation, potentially extending to other types of computational imaging or even different sensory inputs, such as the auditory system.

As a further illustration of potential applications, we note that the ghost imaging protocol presented here represents a form of non-explicit (or nonconscious) information processing. This can be contrasted with explicit processing, where the participant directly evaluates the light intensities observed on the screen. Fig. 2.17 presents results from an experiment comparing imaging quality, quantified using the Structural Similarity Index Measure (SSIM), between 'nonconsciously' acquired data (EEG) and 'consciously' acquired data (explicit verbal or typed responses). Two separate ghost imaging experiments were conducted: (a) EEG only (4-second illumination intervals with EEG readout, separated by 2-second rest periods), and (b) EEG with simultaneous explicit readout (4-second illumination intervals with EEG readout, with explicit readout performed during the 2-second rest periods). We observed that while EEG and explicit readout generally yield similar SSIM image reconstruction qualities, the EEG-reconstructed images deteriorated significantly in the presence of simultaneous explicit readout.

This study suggests that the brain can be integrated into a computational imaging system, potentially acting as a unique type of sensor. However, the observed degradation in image quality from EEG readout when explicit (spoken or typed) responses are also collected points to more complex dynamics. We do not attribute this degradation to the physical effects of vocalizing or typing, as these activities occurred during the rest period between illumination intervals. Instead, we speculate that the degradation may stem from changes in neurological processing, where conscious information processing (such as heightened neural attention in anticipation of an explicit readout) interferes with non-explicit readout. This hypothesis warrants further investigation and suggests that the computational imaging approach demonstrated here—and potentially others—could serve as a valuable tool for exploring information processing within the human brain.

Chapter 3

Brain Phenomenological Model

3.1 Introduction

In the preceding chapter, we demonstrated the utilization of the human brain as a form of "light power" detector. This capability can be harnessed to accomplish ghost imaging tasks and extend its application to various conscious or unconscious experiments. However, exploring the brain's nonlinear effects remains an area that has not been delved into deeply. Consequently, the focus of this chapter shifts towards an in-depth examination of the human brain as an input-output phenomenological model. This study is grounded in empirical SSVEP data and aims to elucidate the brain's response to input stimuli, emphasising the frequency domain analysis.

In general, the SSVEP technique is valuable for investigating cognitive and clinical neuroscience paradigms [160–169]. At the same time, SSVEP-based brain-computer interfaces (BCIs) hold significant potential for communication and control applications [146, 170–172]. Given its importance in these fields of study, it is crucial to understand the key features of SSVEP and its generalization from single to multiple stimuli for practical applications and a deeper understanding of this phenomenon.

However, traditional SSVEP utilizes single-frequency stimuli as a probe, which results in the brain response producing frequency doubling or harmonics. [174, 179–181]. Linear or nonlinear models have been proposed to understand better these phenomena [173, 175, 182–187], which accurately describe many characteristics of SSVEP such as amplitude and phase. However, recent studies have introduced multi-frequency stimuli, aimed at improving BCI performance [188–190], basic frequency intermodulation terms have been found. These include two frequencies of stimulation along with their harmonics and linear combinations using integer coefficients, but its underlying mathematical model remains unclear. Further research is needed to analyse the mathematical model behind this.

Thus, here we present a "Phenomenological model" to address the challenge at hand, which is close to the Hammerstein-Wiener Model, especially Hammerstein Model [191]. Firstly, it introduces a mathematical formula to analyse the essential features of SSVEP when exposed to single-frequency stimuli. This analysis is then extended into two categories: narrowband and broadband. The narrowband approach uses analytical approximation, while statistical methods are employed in the broadband approach. The experimental results demonstrate that the proposed model fits well with the data obtained from experiments.

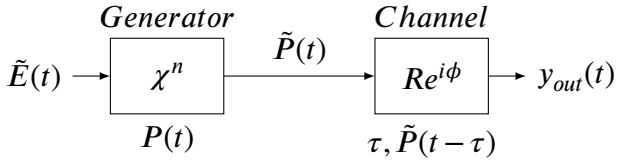

Figure 3.1: The brain model comprises two systems: a generator for explaining SSVEP's nonlinear effects, and a channel model for explaining statistical frequency-domain properties and temporal delays.

To capture the essence of the brain's nonlinearity and the transmission of brain signals, we have conceptualized the brain as comprising two distinct systems, as illustrated in Figure 3.1. The first system is a nonlinear component, called the 'generator,' which can be effectively analysed using models derived from nonlinear optics. Concurrently, the second system, which accounts for the multipath propagation of signals, can be suitably approximated using the fading channel model. Furthermore, this channel model incorporates a delay, represented by the average value τ.

In the subsequent sections, we will delve into frequency sweeping, and then go deeper into the model applied to narrowband and broadband conditions. The experimental result in each subsection, verify the model well, which is the justification and evidence to support the use of this model

3.2 Setup

The setup for the light stimulus is illustrated in Figure 3.2. A computer controls a Digital-to-Analog Converter (DAC) to produce a signal that modulates an LED bulb. A white wall reflects the modulated light from the LED and is then detected by the human eye, stimulating the brain to generate an SSVEP signal originating from the primary visual cortex. This SSVEP signal is sampled by an EEG device and sent to a computer for further analysis. Initially, we employ frequency sweeping to examine the brain signal's response to different frequency stimuli.

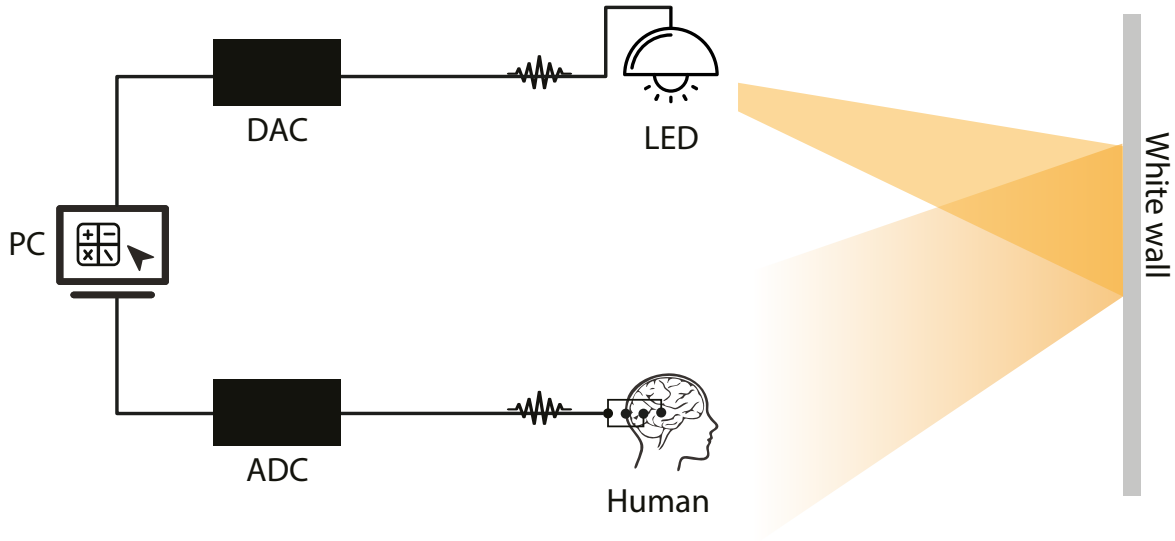

Figure 3.2: Schematic overview of the setup used for steady-state visually evoked potential frequency-division multiplexing.

3.3 Frequency sweeping

The frequency sweeping experiment is implemented to study the effect of SSVEP under different stimulus frequencies. In detail, we implement the setup illustrated in Fig. 3.2, where the LED is controlled to flash with a cosine wave at varying frequencies, a process referred to as frequency sweeping. The frequencies range from 3 to 24 Hz, with each frequency maintained for 80 seconds. During this time, the SSVEP is recorded. The collected SSVEP data is then processed to calculate the amplitude spectrum with a resolution of 1 Hz.

We find the output amplitude also changes dramatically when the frequency changes. The heatmap, as shown in Fig.3.3, is a frequency sweeping experiment result where the input single frequency is sweeping from 3 Hz to 24 Hz and a list of output spectrum will form a heatmap. Several harmonics were shown in this heatmap, and the frequency of harmonics increases when the input frequency increases. Most amplitude spectra obey the descent phenomenon.

In addition, when the input frequency is within $[6, 8]$ Hz, the fundamental frequency of the output is weaker, but the second harmonic is stronger, compared to other's input frequency. For example, the related amplitude spectrum under 7 Hz stimuli is shown in Fig.3.4a), where the first harmonic amplitude is weaker than the third harmonic amplitude. It did not match the descent phenomenon due to the filter effect of the H function. Fig.3.3 shows that the output frequency between 10 Hz to 20 Hz is stronger than others.

When the input is a cosine wave with frequency sweep, the nonlinear function will induce comb frequency sweep to scan the H function in the frequency domain. The comb frequency sweep

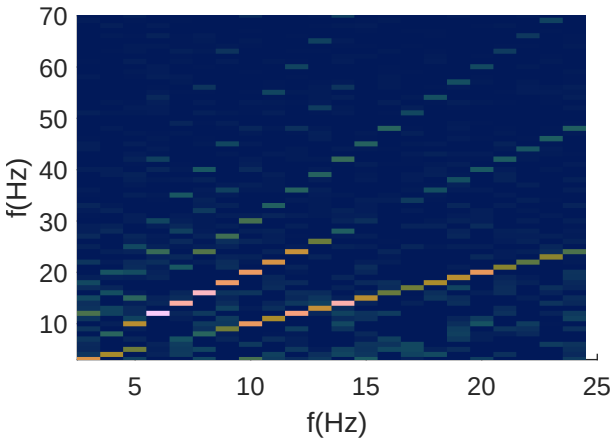

Figure 3.3: The amplitude spectrum of SSVEP under stimulus, sweeping from 3 Hz to 24 Hz.

consists of harmonics, and it is to do a multi-frequency sweeping scan of the frequency response of the H function. So, if we pick up the first or second harmonic frequency response, it will form the frequency response of the H function, reflecting the filter effect's features.

When it comes to harmonics' sweeping, the first harmonics and second harmonics amplitude of the response is shown in Fig.3.4b). Both show a bandpass effect in the H function, from 10 Hz to 20 Hz. In addition, the $[6,8]$ Hz valleys show that the amplitude of the first harmonic at low-frequency range $[3,5]$ Hz is affected by the low-frequency noise background.

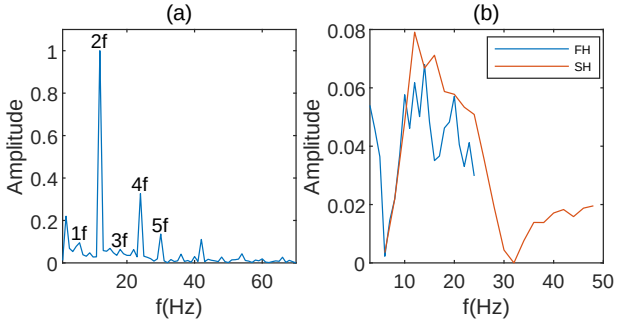

Figure 3.4: a) The amplitude of the spectrum of SSVEP under 7 Hz; b) The amplitude spectrum harmonics removed background energy.

These effects may be caused by the filter effect of the brain, which is called the H function. To describe the H function properly, we need to show some phenomena first.

When we take stimulus, the frequency peaks' location in the EEG spectrum is the same as the input signal $u_s(t)$. Then, when we withdraw the stimulus, the amplitude of EEG will oscillate back to a lower level amplitude, which could be referred to as the system's response delay. So, we tried to use an RLC model, similar to the second-order filter model mentioned in Ref [187], as shown in Fig.3.5, to approach these phenomena.

Finally, the differential equation of the RLC circuit is $R \cdot i(t) + L \cdot \frac{di(t)}{dt} + \frac{1}{C} \cdot \int i \cdot dt = u_s(t-\tau)$.,

where R stands for energy consumption; L and C stands for signal oscillation in the brain; τ is the time delay.

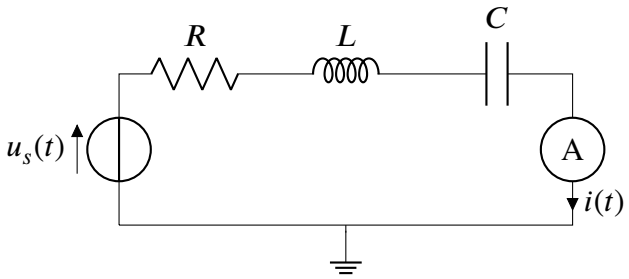

Figure 3.5: RLC circuit.

After considering these factors, we have devised an approach to estimate the H function. To eliminate the impact of the nonlinear function f(), we suggest using a step function, $x(t) = \text{Step}(t)$ as illustrated in Eq.3.1.

$$\begin{aligned} x(t) &= \text{Step}(t); \\ y(t) = \text{f}(x(t)) &= A \times \text{Step}(t); \\ y_{out}(t) &\sim h(t) * \text{Step}(t) \end{aligned} \tag{3.1}$$

$y(t)$ is the output of $\text{f}(x)$, which will also be a Step function; $y_{out}(t)$ the final readout/response, will be linear to the convolution between $h(t)$ and $\text{Step}(t)$.

So, in the experiment, we used a 1 Hz square wave (50% duty) as the stimuli, and then we acquired the VEP signal. As shown in Fig.3.6, a clear pulse is shown after around, $120ms$ with duration

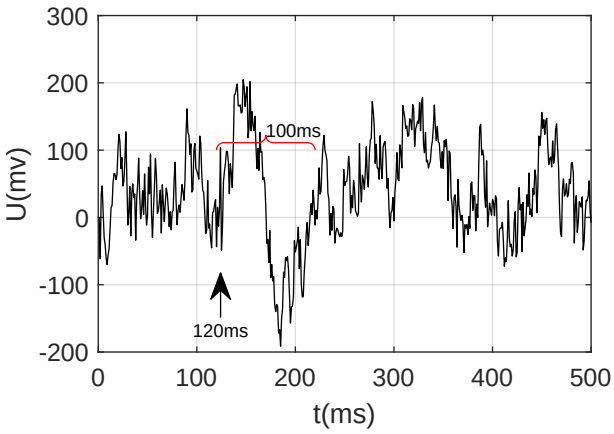

Figure 3.6: The VEP waveform under 1 Hz square stimuli.

about $0.1s$. To fit the data, the model was built in Eq.3.2.

$$\begin{aligned} \mathrm{H}(s) &= e^{-\tau s}\frac{s/L}{s^2+2\zeta w_n s+w_n}; \\ w_n &= \sqrt{\frac{1}{LC}}; \zeta = \frac{R}{2\sqrt{\frac{L}{C}}}; \\ y_{out}(t) &= \mathscr{L}^{-1}[\frac{H}{s}] \\ &= \frac{\mathrm{e}^{-\zeta w_n (t-\tau)}\sin\left(\sqrt{1-\zeta^2}\, w_n (t-\tau)\right)}{L w_n \sqrt{1-\zeta^2}}. \end{aligned} \tag{3.2}$$

Where $\mathrm{H}(s)$ is the transform function of the defined RLC circle, simulating the filter effect of the brain; $y_{out}(t)$ is the readout signal.

The data of the VEP waveform shown in Fig. 3.6 between 120ms and 250ms can be fitted using $y_{out}(t)$, as shown in Fig.3.7. The fitting result shows that $\tau = 125.5ms$, $\frac{w_n}{2\pi} = 11.25$ Hz, and

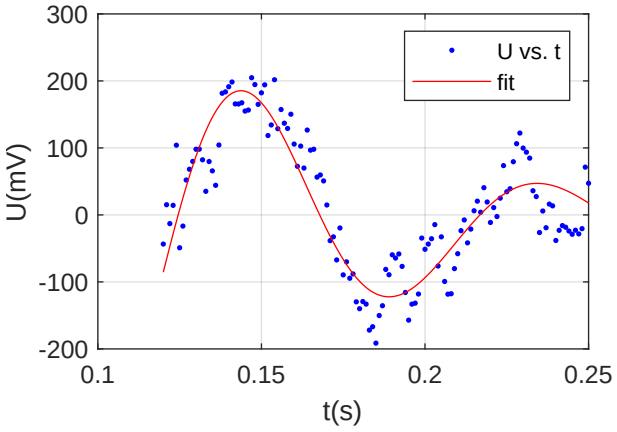

Figure 3.7: The curve fitting result of $y_{out}(t)$.

$\zeta = 0.19$, and the step response and frequency/phase response are shown in Fig.3.8.

Finally, the H function is defined, which is a second-order bandpass filter, and the bandpass centre is around 11 Hz.

3.4 Narrowband

3.4.1 Generator model

Before discussing the nonlinear effects of the brain, we first introduce the nonlinear model described in the nonlinear optics book by Boyd [192]. This model characterizes optical nonlinear-

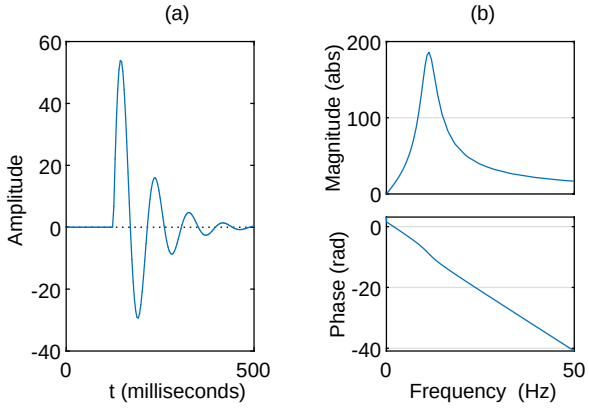

Figure 3.8: a) The step response of H function, |H(w)|; b) Frequency response of H function.

ities directly in the time domain by considering the polarization, as shown in Eq. (3.3).

$$\begin{aligned} P(t) &= \tilde{P}^{(1)}(t) + \tilde{P}^{(2)}(t) + \tilde{P}^{(3)}(t) + ... + \tilde{P}^{(n)}(t); \\ \tilde{P}^{(n)}(t) &= \epsilon_0 \int_0^\infty d\tau_1 \int_0^\infty d\tau_2 ... \int_0^\infty d\tau_n \\ & R^{(n)}(\tau_1, \tau_2, ..., \tau_n) \\ & \times \tilde{E}(t-\tau_1)\tilde{E}(t-\tau_2)...\tilde{E}(t-\tau_n); \end{aligned} \tag{3.3}$$

where $\tilde{P}^{(1)}(t)$ is the linear polarization; $\tilde{P}^{(2)}(t)$ is the second-order polarization; $\tilde{P}^{(3)}(t)$ is the third-order polarization; $\tilde{P}^{(n)}(t)$ is the nth-order polarization; $R^{(1)}$, $R^{(2)}$ and $R^{(3)}$is the linear, second-order and third-order response functions, respectively.

$$\begin{aligned} & \chi^{(n)}(w_{\Sigma_n}; w_1, w_2, ..., w_n) = \int_0^\infty d\tau_1 \int_0^\infty d\tau_2 ... \int_0^\infty d\tau_n \\ & R^{(n)}(\tau_1, \tau_2, ..., \tau_n) e^{i(w_1\tau_1 + w_2\tau_2 + ... + w_n\tau_n)}; \\ & w_{\Sigma_n} = \sum_{j=1}^{n} w_j; \end{aligned} \tag{3.4}$$

After considering Eq. (3.4) and $\tilde{E}(t)$, $\tilde{P}^{(1)}(t)$ and $\tilde{P}^{(2)}(t)$ can be transformed into the frequency domain by applying Fourier transforms of $\tilde{E}(t)$, so the simplified one is shown in Eq. (3.5).

$$\begin{aligned} E(w) &= E\int_{-\infty}^{\infty}\tilde{E}(t)e^{iwt}dt; \\ \tilde{E}(t) &= \frac{1}{2\pi}\int_{-\infty}^{\infty}E(w)e^{-iwt}dw; \\ \tilde{P}^{(n)}(t) &= \epsilon_0\int_{-\infty}^{\infty}\frac{dw_1}{2\pi}\int_{-\infty}^{\infty}\frac{dw_2}{2\pi}...\int_{-\infty}^{\infty}\frac{dw_n}{2\pi} \\ &\quad\times\chi^{(n)}(w_{\Sigma_n};w_1,w_2,...,w_n) \\ &\quad\times E(w_1)E(w_2)...E(w_n)e^{-iw_{\Sigma_n}t}; \\ w_{\Sigma_n} &= \sum_{j=1}^{n}w_j. \end{aligned} \tag{3.5}$$

When considering the narrowband condition where $w_1, w_2, \ldots, w_n$ are very close and fall within a narrow frequency range, we make an approximation as shown in Eq. (3.6) to simplify the calculations, which is based on $w_1 \approx w_2 \approx \cdots \approx w_n$. This allows Eq. (3.5) to be reduced to the more manageable form shown in Eq. (3.7).

$$\begin{aligned} &\chi^{(n)}(w;w_1,w_2,...,w_n) \approx \chi^{(n)}(w) = \chi_n\chi(w); \\ &\chi^{(n)}(w) = \int_0^{\infty}R^{(n)}(t)e^{iwt}dt; \\ &R^{(n)}(t) = \chi_n R(t); w = \sum_{j=1}^{n}w_j. \end{aligned} \tag{3.6}$$

$$\begin{aligned} \tilde{P}^{(n)}(t) &= \epsilon_0 R^{(n)}(t) * (\tilde{E}(t)^n); \\ P(t) &= \sum_{n=1}^{N_H}\tilde{P}^{(n)}(t) = h(t) * \mathrm{f}(\tilde{E}(t)); \\ h(t) &= \epsilon_0 R(t); \\ \mathrm{f}(x) &= \sum_{n=0}^{N_H}\chi_n x^n; \\ \mathrm{H}(w) &= \mathscr{F}(h(t)); \end{aligned} \tag{3.7}$$

where, the generator has two operations, nonlinear mapping $\mathrm{f}(x)$ and filtering $\mathrm{H}(w)$. $\mathrm{f}(x)$ maps input stimuli to the corresponding response within the brain, represented by $y(t)$. The filter effect of the brain is denoted as $h(t)$ or its transform function $\mathrm{H}(w)$.

To describe the nonlinear response of the brain, we would like to build an analytical model of the nonlinear transfer function of the system. This is a similar problem to the one encountered

in optics when modelling the nonlinear response of a medium to the interaction with light. A possible approach is to expand perturbatively the nonlinear transfer function as a Taylor series. In optics, this leads to the perturbative nonlinearities. In our model, we follow a similar approach

When it comes to the brain response, the brain response is represented by $y_{out}(t)$ and the input stimulus is denoted by $x(t)$. Equation 3.8 displays both the general expression for $y(t)$ and its Taylor expansion.

$$\begin{aligned} y(t) &= \mathrm{f}(x(t)) = \sum_{n=0}^{N_H} \chi_n x(t)^n; \\ y_{out}(t) &= h(t) * y(t); \\ Y_{out}(w) &= \mathrm{H}(w) \sum_{n=0}^{N_H} \chi_n \underbrace{X(w) * X(w) * ... * X(w)}_{n}. \end{aligned} \tag{3.8}$$

where χ_n is the coefficient for $n\,th$ item in Taylor expansion; $x(t)$ and $X(w)$ are the input stimulus signal in the time domain and frequency domain respectively; $y_{out}(t)$ and $Y_{out}(w)$ are the brain response signal in the time domain and frequency domain respectively.

In addition, if we consider the $\tilde{P}^{(n)}(t)$ and $w_{\Sigma_n} = \sum_{j=1}^{n} w_j$, the frequency mixing from the brain response can be expressed in Eq. (3.9).

$$\begin{aligned} F_{mix} &\in \{\sum_{j=1}^{n} f_j\}; \\ f_j &\in \{-F_N ..., -F_2, -F_1, 0, F_1, F_2, ..., F_N\}; \end{aligned} \tag{3.9}$$

where f_j is one frequency from the frequency list with N input cosine wave. For example, when $\tilde{E}(t) = \cos(2\pi f t)$, $f_j \in \{-f, 0, f\}$, and when $n = 3$, then $F_{mix} \in \{-3f, -2f, -f, 0, f, 2f, 3f\}$.

In the narrowband frequency range, the filtering effect of the brain can be considered constant. To simplify our expression, we make an autocorrelation approximation and define $\{X(w)\}^{\pm m}$ notation as shown in Eq.3.10.

$$\begin{aligned} &\underbrace{X(w) * X(w) * ... * X(w)}_{m} = \{X(w)\}^m; \\ &\underbrace{X(-w) * X(-w) * ... * X(-w)}_{m} = \{X(-w)\}^m = \{X(w)\}^{-m}; \\ &\{X(w)\}^m \{X(w)\}^{-m} = \{X(w)\}^0 \approx \delta(w);; \end{aligned} \tag{3.10}$$

where $X(w)$ represents the Fourier transform of a signal, m denotes the number of convolutions performed. The expression $\delta(w)$ represents the Dirac delta function, which approximates the

result of convolving a function with its inverse in the frequency domain.

3.4.2 Single band

In the single narrowband frequency, we consider the input stimulus $x(t)$ to have a frequency band consisting of a series of discrete frequencies, with N pixels and a bandwidth of w_{band}. This is illustrated in Eq.3.11.

$$\begin{aligned} x(t) &= \sum_{n=1}^{N} A_n \cos(w_n t); \\ X(w) &= \mathcal{F}[x(t)] = \left(X_p(w) + X_p(-w)\right); \\ X_p(w) &= \sqrt{\frac{\pi}{2}} \sum_{n=1}^{N} A_n \delta(w - w_n); \\ \mathcal{F}[x(t)^n] &= \{X(w)\}^n \approx \sum_{m=0}^{n} C_n^m \{X_p(w)\}^{n-2m}. \end{aligned} \tag{3.11}$$

Since $w_{band} \ll w_0$, the set $\{X_p(w)\}^n$ will consist of narrowband frequencies around nw_0 that do not overlap with each other. Furthermore, the amplitude spectrum's envelope takes on a Gaussian-like shape due to the presence of the C_n^m term in Eq.3.11. Finally, one simple conclusion can be drawn in Eq.3.12

$$|Y(w)| \approx \sum_{n=0}^{\infty} K_n \{X_p(w)\}^n. \tag{3.12}$$

In short, the frequency band shape around nw_a is marked as $|Y(nw_a)| \sim \{X_p(w)\}^n$.

In the single narrowband experiment, the signal starts from 12Hz as shown in Eq.3.13, where $N = 10$ frequencies will be encoded into $f_{band} = 0.5Hz$ frequency band. In addition, the measurement time was 160 seconds.

$$\begin{aligned} f_{band} &= 0.5Hz; \\ N = 10; \delta f &= f_{band}/N; \\ f_a &= 12Hz; \\ A &= [0,0,1,1,0,0,1,0,0,0]; \\ \frac{w_n}{2\pi} &= f_a + (n-1)\delta f; \\ x(t) &= \sum_{n=1}^{N} A_n \cos(w_n t). \end{aligned} \tag{3.13}$$

f_{band} is the frequency bandwidth; N is the number of frequencies used in each narrowband; δf is the frequency resolution; f_a is the start frequency point for the first narrowband; A is the amplitude vector for the first narrowband; $x(t)$ is the final signal encoded, which will be fed into LED via DAC.

After feeding LED the signal $x(t)$ and measuring the EEG signal, the amplitude spectrum of EEG is shown in Fig.3.9a), where three bands with high values were marked with corresponding frequency: $|Y(w_a)|$, $|Y(2w_a)|$, and $|Y(3w_a)|$. The cosine similarity (COSS)of the amplitude spectrum between EEG and brain model is also shown in Fig.3.9.

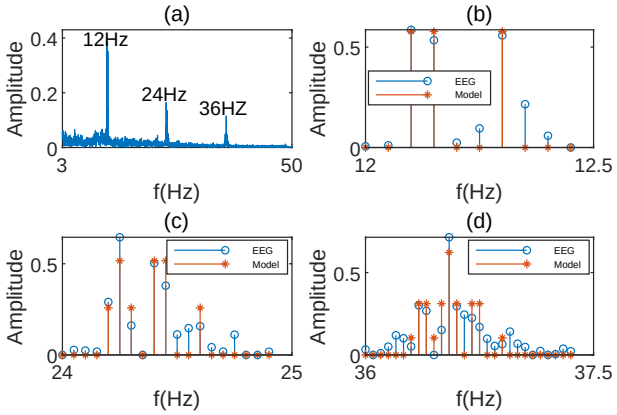

Figure 3.9: The amplitude spectrum vs brain model. a) is the amplitude spectrum of the SSVEP signal; b) is the $|Y(w_a)|$ results with $COSS = 0.97$; c) is the $|Y(2w_a)|$ results with $COSS = 0.95$; d) is the $|Y(3w_a)|$ results with $COSS = 0.90$;

3.4.3 Double bands

Regarding the two narrow bands illustrated in Eq. 3.14, they are defined as $[w_a, w_a + w_{band}]$ and $[w_b, w_b + w_{band}]$, where $0 < w_a < w_b$.

$$
\begin{aligned}
x(t) &= \sum_{n=1}^{N} A_n \cos(w_n t) + \sum_{m=1}^{N} B_n \cos(w_m t); \\
\sum_{n=1}^{N} A_n^2 &= \sum_{m=1}^{N} B_n^2; \\
X_a(w) &= \sqrt{\frac{\pi}{2}} \sum_{n=1}^{N} A_n \delta(w - w_n); \\
X_b(w) &= \sqrt{\frac{\pi}{2}} \sum_{m=1}^{N} B_m \delta(w - w_m); \\
X(w) &= \big(X_a(w) + X_a(-w) + X_b(w) + X_b(-w)\big) \\
&= (X_a(-w) + X_b(-w)) \\
&\quad * (\delta(w) + X_a(w) * X_b(w)); \\
\mathscr{F}[x(t)^n] &= \{X(w)\}^n \\
&\approx \sum_{j=0}^{n} \sum_{m=0}^{n} C_n^j C_n^m \{X_a(w)\}^{n_a} * \{X_b(w)\}^{n_b}; \\
n_a &= m - n + j; n_b = m - j;
\end{aligned}
\tag{3.14}
$$

$Y(w)$ has multiple frequency bands at $n_a w_a + n_b w_b$, where $n_a, n_b \in \mathbb{Z}$.

First To avoid overlaps between adjacent frequency bands ($n_a w_a + n_b w_b$ and $(n_a + 1)w_a + n_b w_b$), we require that $(n_a + n_b)w_{band} < w_a$. Therefore, this condition is met by satisfying the narrow-band requirement$w_{band} \ll w_a$.

Second To avoid multiple solutions of $n_a w_a + n_b w_b = W$, For example, multiple solutions exist When $w_a = 6Hz, w_b = 12Hz$, the $18Hz$ band can be expressed as either $1 \times w_a + 1 \times w_b$ or $3 \times w_a + 0 \times w_b$, indicating at least two overlapping mixing bands. So, to find a non-overlapping frequency band with only one solution for $n_a = a$ and $n_b = b$, the relationship between w_a and w_b needs to be considered. The ratio of $\frac{w_b}{w_a}$ is defined as being between 0 and k, which helps solve for the upper bound of k in equation 3.15. This reduced result is shown in equation 3.16.

$$
\begin{aligned}
n_a w_a + n_b w_b &= a w_a + b w_b; n_a, n_b \in \mathbb{Z}; \\
1 < \frac{w_b}{w_a} &< k.
\end{aligned}
\tag{3.15}
$$

$$\begin{aligned}(n_b - b_1)(n_b - b_2) < 0;\\ b_1 = a + b - n_a;\\ b_2 = \frac{a + bk - n_a}{k}.\end{aligned} \tag{3.16}$$

To keep only one solution ($a = n_a, b = n_b$) for Eq.3.15, the distance between two roots must be less than 1, as shown in Eq.3.17. The final result is illustrated in Eq.3.18.

$$|b_1 - b_2| < 1; \tag{3.17}$$

$$1 < k < 2. \tag{3.18}$$

Third is identifying the relationship between $\mathcal{F}[x(t)^n]$ and the amplitude of $n_a w_a + n_b w_b$. This can be achieved by solving Eq. 3.19 where n, m, and j is from Eq.(3.14). The solution is unique and given by Eq.3.20. This implies that $\{X_a(w)\}^{n_a} * \{X_b(w)\}^{n_b}$ corresponds to the frequency band of $n_a w_a + n_b w_b$. It also provides additional information as m and j should be integer. Specifically, when n_a and n_b are both odd or even so that $n_a \pm n_b$ will be even and only n is even, $n = 2k$ will make m and j to be an integer. As a result, the term $\{X_a(w)\}^{n_a} * \{X_b(w)\}^{n_b}$ is contributed by $x(t)^{2k}$. On the other hand, when one of n_a and n_b is odd and the other is even so that $n_a \pm n_b$ will be odd and only n is odd, $n = 2k + 1$ will make m and j to be an integer. As a result, the term $\{X_a(w)\}^{n_a} * \{X_b(w)\}^{n_b}$ is contributed by $x(t)^{2k+1}$.

$$\begin{aligned}0 \le m \le n;\\ 0 \le j \le n;\\ m - n + j = n_a;\\ m - j = n_b;\end{aligned} \tag{3.19}$$

$$m = \frac{n_a + n_b + n}{2}; j = \frac{n_a - n_b + n}{2}; \tag{3.20}$$

Finally, under these two conditions: narrowband $w_{band} < \frac{w_a}{n_a + n_b}$ and unique $0 < k < 2$, the amplitude spectrum shape can be expressed in Eq.3.21.

$$\begin{aligned}|Y(w)| \approx \sum_{n_a=-\infty}^{+\infty} \sum_{n_b=-\infty}^{+\infty} K_{n_a,n_b} \{X_a(w)\}^{n_a} \{X_b(w)\}^{n_b};\\ |Y(n_a w_a + n_b w_b)| \sim \{X_a(w)\}^{n_a} \{X_b(w)\}^{n_b}.\end{aligned} \tag{3.21}$$

This technique has multiple applications. For instance, it can be used to calculate the correlation between two signals when $A(t)$ and $B(t)$ are changing in the time domain and $N = 1$. Addition-

ally, it is useful for performing a correlation between a pattern ($A(x,y,t)$) that changes in the time domain and a scale value ($B(t)$) that also changes in the time domain. This application is particularly relevant for ghost imaging reconstructing algorithms.

Moreover, if either $w_a = 0, w_b > 0$ or $w_b = 0, w_a > 0$, it means one band is a DC component x_0 and the other is an AC component $x(t)$. When it satisfies $x(t) \ll x_0$, then Eq. 3.8 can be simplified to Eq. 3.22.

$$y(t) = \mathrm{f}(x(t) + x_0) \approx \mathrm{f}(x_0) + \mathrm{f}'(x_0)x(t); \tag{3.22}$$

According to Frequency doubling model [182], $\mathrm{f}(x)$ was assumed to be $log(x)$. For simplify, we assume $\mathrm{f}(x) = ln(x)$

$$\begin{aligned} &y(t) = \mathrm{f}(x(t) + x_0) \approx \mathrm{f}(x_0) + \frac{x(t)}{x_0}; \\ &A_{y(t)} \sim \frac{A_{y(t)}}{x_0}; \\ &Contrast = \frac{\sigma}{\mu} = \frac{A_{x(t)}}{x_0}; \\ &A_{y(t)} \sim Contrast. \end{aligned} \tag{3.23}$$

where $A_{y(t)}$ stands for the related amplitude of $y(t)$; $A_{x(t)}$ stands for the related amplitude of $x(t)$; $Contrast$ is the contrast of luminance; σ is the luminance difference, standing by amplitude of $x(t)$; μ is the average luminance, which is equal to x_0. So, it means that the SSVEPP amplitude vs. contrast function was approximately linear, which is consistent with the experimental results [193].

In two narrowband experiments, two narrowband signals, starting from 12Hz and 15Hz respectively, were defined in Eq.3.24, where $N = 10$ frequencies will be encoded into $f_{band} = 0.5Hz$ frequency band. In addition, the unique condition, Eq.3.18, was met, as $1 < \frac{15}{12} < 2$, and the

measurement time was 160 seconds.

$$
\begin{aligned}
f_{band} &= 0.5Hz; \\
N = 10; \delta f &= f_{band}/N; \\
f_a = 12Hz; f_b &= 15Hz; \\
A &= [0,0,1,1,0,0,1,0,0,0]; \\
B &= [1,1,0,0,0,0,1,0,0,0]; \\
\frac{w_n}{2\pi} &= f_a + (n-1)\delta f; \\
\frac{w_m}{2\pi} &= f_b + (m-1)\delta f; \\
x(t) = \sum_{n=1}^{N} A_n \cos(w_n t) &+ \sum_{m=1}^{N} B_n \cos(w_m t).
\end{aligned}
\tag{3.24}
$$

f_{band} is the frequency bandwidth; N is the number of frequencies used in each narrowband; δf is the frequency resolution; f_a and $f_b$is the start frequency point for the first and second narrowband, respectively; A and B are the amplitude vectors for the first and second narrowband, respectively; $x(t)$ is the final signal encoded, which will be fed into LED via DAC.

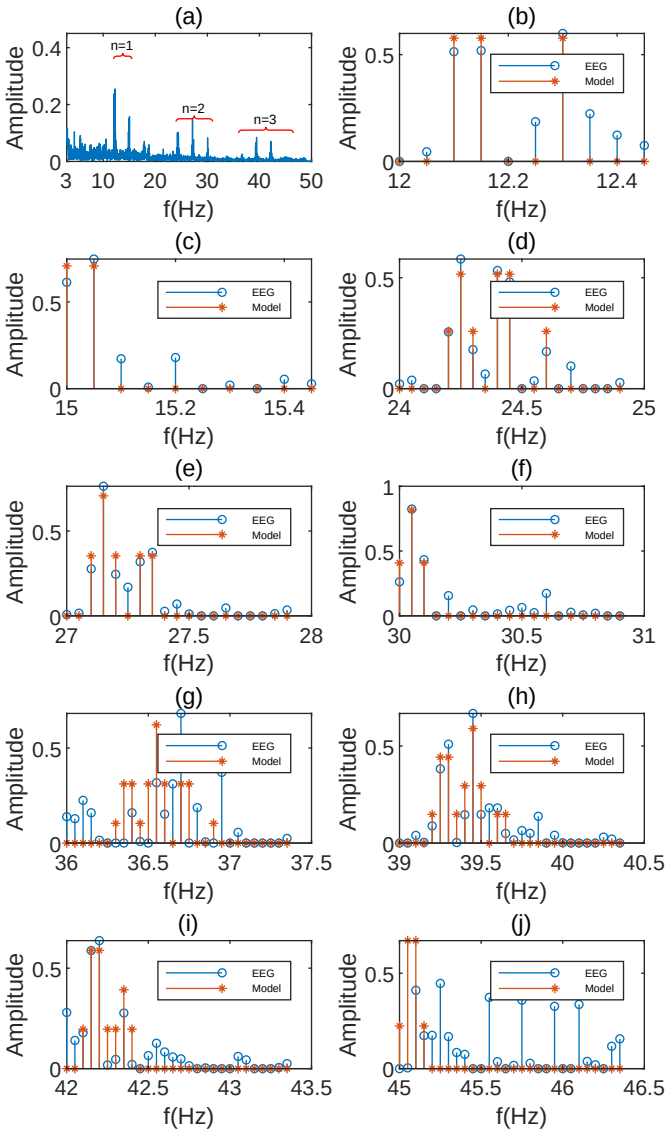

Figure 3.10: The amplitude spectrum vs brain model. b) and c) is in $n = 1$ band area; d), e) and f) is in $n = 2$ band area; g), h), i) and j) is in $n = 3$ band area; a) is the amplitude spectrum of the SSVEP signal; b) is the $|Y(1 \times w_a + 0 \times w_b)|$ results with $COSS = 0.94$; c) is the $|Y(0 \times w_a + 1 \times w_b)|$ results with $COSS = 0.96$; d) is the $|Y(2 \times w_a + 0 \times w_b)|$ results with $COSS = 0.98$; e) is the $|Y(1 \times w_a + 1 \times w_b)|$ results with $COSS = 0.97$; f) is the $|Y(0 \times w_a + 2 \times w_b)|$ results with $COSS = 0.96$; g) is the $|Y(3 \times w_a + 0 \times w_b)|$ results with $COSS = 0.51$; h) is the $|Y(2 \times w_a + 1 \times w_b)|$ results with $COSS = 0.92$; i) is the $|Y(1 \times w_a + 2 \times w_b)|$ results with $COSS = 0.88$; j) is the $|Y(0 \times w_a + 3 \times w_b)|$ results with $COSS = 0.32$;.

After feeding LED the signal $x(t)$ and measuring the EEG signal, the amplitude spectrum of EEG is shown in Fig.3.10a), where three band area,$n = n_a + n_b = \{1, 2, 3\}$. The cosine similarity (COSS)of amplitude spectrum between EEG and brain model is also shown in Fig.3.10. The average COSS of these three bands is 0.94, 0.94, and 0.71, respectively. Because $|Y(n_a w_a + n_b w_b)| \sim X(w_a)^{n_a} X_b{}^{n_b}$, Fig.3.10b) and c) stand for the amplitude vectors A and B; Fig.3.10d),

e), and f) stand for the second harmonics of two narrowband inputs, stands for $A * A$, $A * B$ and $B * B$, respectively; Fig.3.10g), h), i) and j) stand for $B * BastB$, $A * B * B$, $A * A * B$, and $A * A * A$. In conclusion, when it comes to narrowband, the nonlinear function can be used to do convolution.

3.5 Broadband

3.5.1 Channel model

In densely populated urban areas, the transmission of signals often encounters obstructions such as buildings and other structures. This environment is characterized by the Rayleigh fading model, which accounts for the signal strength variations caused by multiple reflections off these obstacles [194]. When direct line-of-sight between the transmitter and receiver is blocked, the signal undergoes numerous reflections, scattering in various directions and leading to fluctuations in the received signal strength. This phenomenon is particularly relevant for wireless communications in city centres, where the complex urban landscape necessitates robust communication systems that can adapt to the ever-changing signal conditions imposed by Rayleigh fading.

Drawing a parallel to this concept, we assume the presence of multipath propagation in neural pathways due to the complex neural connections and the lack of a direct line of sight between the transmitter("eye") and receiver("SSVEP"). This assumption is encapsulated by the multipath propagation model described by Eq. 3.25. In this context, the average propagation delay is represented by τ.

$$x_o(t) = \frac{1}{\sqrt{N}} \sum_{n=1}^{N} c_n x_i(t - \tau_n). \tag{3.25}$$

where $x_i(t)$ is the input signal; $x_o(t)$ is the output signal; c_n represents the complex amplitude; τ_n is the delay in the n-th path;

Typically, the fading process is characterized by a Rayleigh distribution for a non-line-of-sight path and a Rician distribution for a line-of-sight path [194]. So, the amplitude of each frequency obeys Rayleigh distribution, as shown in Eq. (3.26)

$$\begin{aligned} R &\sim \text{Rayleigh}(\sigma); \\ |X_o(w)| &= R|X_i(w)|. \end{aligned} \tag{3.26}$$

where $|X_i(w)|$ and $|X_o(w)|$ are the amplitude spectrum of $x_i(t)$ and $x_o(t)$, respectively.

So, We can apply the Rayleigh channel, or Rayleigh fading models between f and H function. The envelope of the channel response will therefore be Rayleigh distributed. Here, we are focusing on the amplitude at w, which has been modulated by the Rayleigh channel.

Typically, the longer the acquisition time, the smaller the standard deviation. For starters, like a short acquisition time $t = \tau_0$, the distribution is shown in Eq.3.27.

$$\begin{aligned} Y &= |Y(w)| \sim \text{Rayleigh}(\sigma); \\ Z_{\tau_0} &= |Y(w)|^2 \sim \text{Exp}(\lambda), \lambda = \frac{1}{2\sigma}; \end{aligned} \tag{3.27}$$

To conclude, ensuring an adequate measurement duration is essential for obtaining a power spectrum of brain signals that conforms to the exponential distribution, which is a particular case of the Gamma distribution. An insufficient measurement length can result in inaccurate spectrum estimates, primarily due to the influence of noise. Thus, selecting an appropriate measurement length is critical for precise signal analysis and the reliability of subsequent interpretations.

3.5.2 Statistical Analysis

When it comes to EEG spectra, if the EEG spectra are measured under the stimulus, it is called stimulus state and if under no stimulus, it is called baseline state or baseline. To figure out the relationship between the input stimulus spectrum and output response spectrum, it is a good choice to start with several frequencies to reduce complexity, instead of encoding an image into the light stimulus, which may induce hundreds of different frequencies.

So, 12Hz+16Hz stimulus was used in this experiment with 4 seconds measuring the duration and repeated 20 times to calculate the mean and Standard deviation (Std) of each frequency in the spectrum. Both states are shown in Fig.3.11.

As shown in Fig.3.11a1) the alpha wave around 10Hz is clear to figure out as the subject is under no stimulus, while Fig.3.11b1) shows several frequency mixing peaks, including sum frequency 4Hz and difference frequency 28Hz. However, the Mean and Std curves are similar in Fig.3.11a1) and b1), so the Mean vs Std curve are shown in Fig.3.11 a2) and b2), illustrating that they show a linear relationship for both state: $Mean = Std$. So, we can find a distribution function to present the state. The main stage is to figure out the correlation between frequencies for a Multivariate distribution.

Correlation coefficients analysis is shown in Fig.3.12a1) and b1). And most absolute values of correlation coefficients are less than 0.8. To simplify, We can assume that the power variation at each frequency is independent of the same type of distribution, regarding $X \sim \text{Exp}(\lambda)$, according to the linear fitting result in Fig.3.11a2) and b2). So, the next step is to find the parameter of

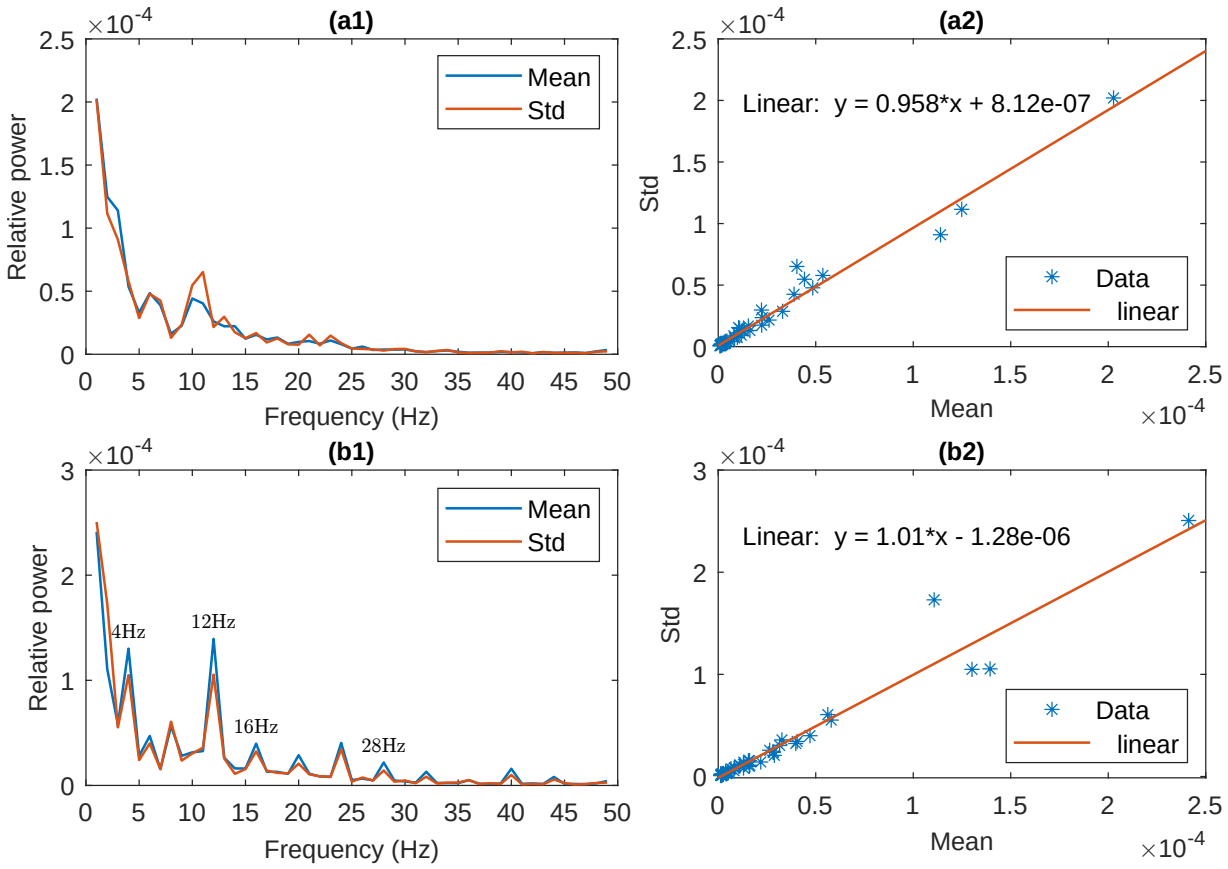

Figure 3.11: EEG spectrum under baseline state and stimulus state (12Hz+16Hz). a1) is the Mean and Std of spectrum under baseline state; a2) is the fitting between the Mean and Std of the spectrum under the baseline state; b1) is the Mean and Std of spectrum under stimulus state; b2) is the fitting between the Mean and Std of the spectrum under stimulus state. (More kinds of stimulus can be found in the Appendix)

the distribution. As $Mean = Std$, the histogram of normalized X, $\frac{X}{X_{Mean}} \sim \text{Exp}(1)$, are shown in Fig.3.12a2) and b2). The histogram graph shows a long tail similar to an exponential distribution. And exponential distribution also meets $\mu = \sigma$. So, we can assume that each frequency's power is exponential distribution – $\frac{X}{X_{Mean}} \sim \text{Exp}(1)$.

3.5.3 Statistical model

Due to the nonlinear effect of the brain, several peaks can be figured out in Fig.3.11b1) and these frequencies with peaks we called mixing frequencies. So, all possible mixing frequency peaks formula are shown in Eq.(3.9). As shown in Fig.3.11a1) and b1), the signal is mainly in the area of the peak. So, to augment the peaks the spectrum of the stimulus state is divided by the spectrum of the baseline state, as shown in Fig.3.13. It indicates that all the peaks are marked, and verified the Eq.3.9.(More verification can be found in the Appendix).

When it comes to Ratio (R) comparing stimulus state spectrum to baseline state spectrum, as

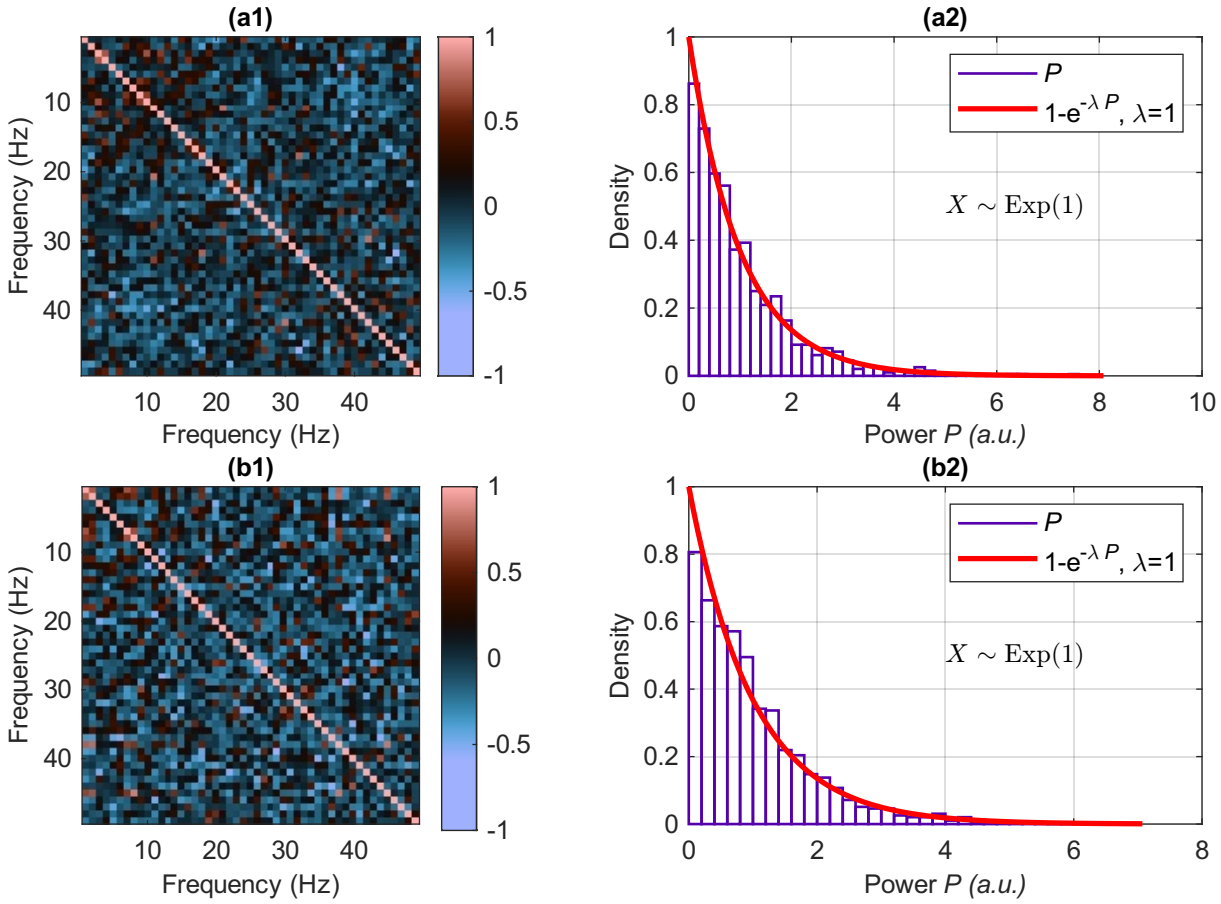

Figure 3.12: EEG spectrum correlation coefficients and histogram. a1) EEG spectrum correlation coefficients under baseline state; a2) Normalized EEG spectrum histogram under baseline state; b1) EEG spectrum correlation coefficients under stimulus state; b2) Normalized EEG spectrum histogram under stimulus state.

shown in Fig.3.13. the peak part is higher than the others. So, the histogram of Non-peak part Ratio(R_N) and Peak Ratio (R_P) are shown in Fig.3.13b) and c). The distribution fitting results are shown in Eq.3.28.

$$R(f) = \begin{cases} R_P \sim \text{Exp}(\lambda_P), \frac{1}{\lambda_N} = 5, & f \in F \\ R_N \sim \text{Exp}(\lambda_N), \frac{1}{\lambda_P} = 1, & f \notin F \end{cases} \tag{3.28}$$

The fitting results show that the Peaks value is 5 times higher than the baseline on average, while the Non-Peaks value is equal to the baseline on average. As mentioned above, the key parameters shown below are used to build the brain model, which can be used to create synthetic data.

So, the EEG spectrum power distribution $S(f)$ is shown in Eq.3.29, where f is the frequency in the spectrum. If $f \in F$, as a frequency mixing peak, $S(f) = R_P B(f)$. If not, as a background,

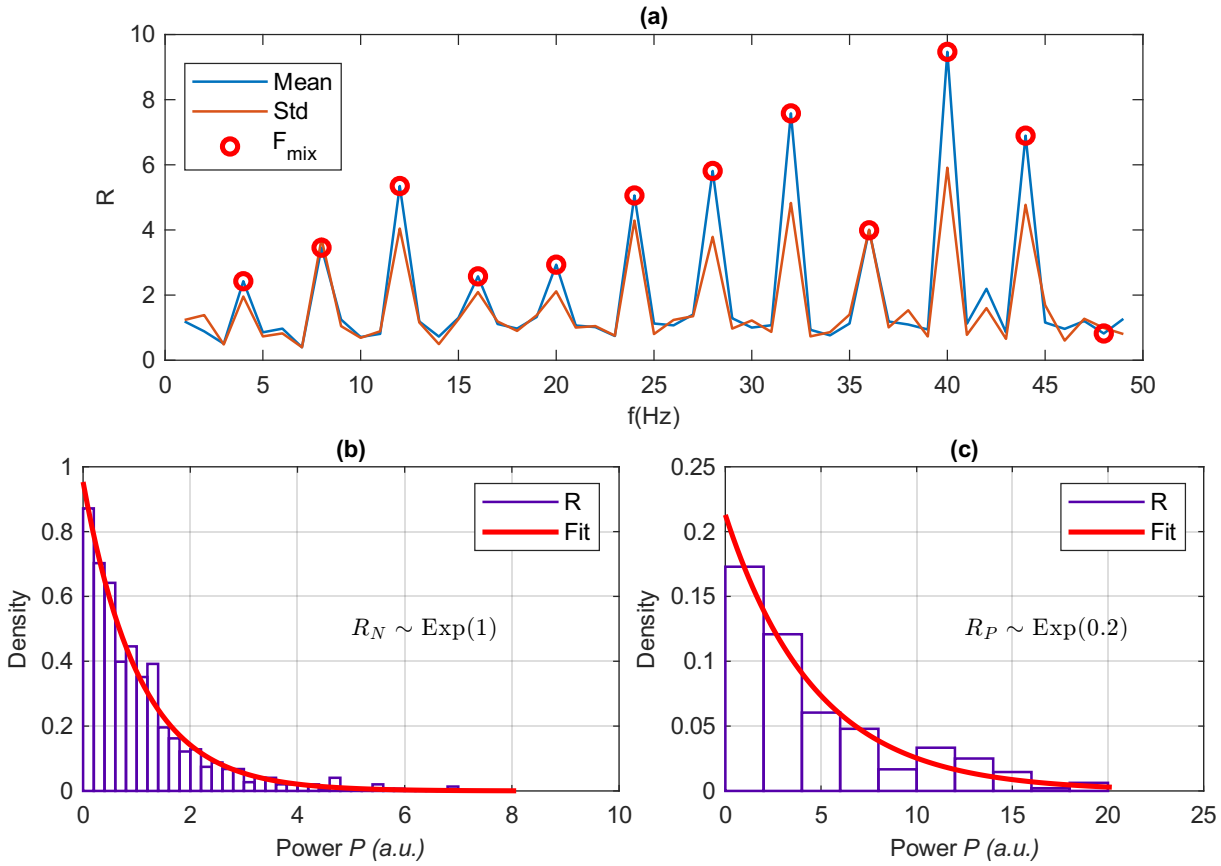

Figure 3.13: EEG spectrum Ratio and distribution under baseline and stimulus state. a) EEG spectrum Mean and Std of Ratio for each frequency, and Ratio is comparing stimulus state to baseline state; b) EEG spectrum Ratio histogram at Non-Peak parts; c) EEG spectrum Ratio histogram at Peak parts.

$S(f) = R_N B(f)$.

$$S(f) = \begin{cases} R_P B(f) \sim \text{Exp}(\frac{\lambda_P}{B(f)}), & f \in F \\ R_N B(f) \sim \text{Exp}(\frac{\lambda_N}{B(f)}), & f \notin F \end{cases} \tag{3.29}$$

where $B(f)$ is baseline from the brain in Fig.3.11; F is mixing frequency set in Eq.3.9; R_p and R_n are peak ratio and Non-peak ratio, respectively, illustrated in Eq.3.28.

In this way, the mapping function of input frequency and its output frequency distribution is obtained. In addition, the number $\frac{1}{\lambda_P} = 4.7$ in Eq.3.29 can be a random number that fluctuates around 4.7, such as $\frac{1}{\lambda_P} \sim U(3,6)$, which makes it more robust for creating synthetic data for deep learning.(more detail about $\frac{1}{\lambda_N}$ and $\frac{1}{\lambda_P}$ in Appendix).

3.6 Conclusion

Starting from the basic frequency sweeping experiment, we identified the nonlinearity of the SSVEP response and the time delay inherent in brain signal transmission. To delve deeper into the study of this nonlinearity, we established two distinct conditions: the narrowband and the broadband. The narrowband condition simplifies the mathematical description, while the broadband condition employs a statistical approach to manage complex outcomes and avoid intricate mathematical challenges.The experimental results under each condition validate the model, providing justification and evidence to support its use.

For narrowband conditions, we began with a straightforward scenario where the input was a single-frequency cosine signal. Our research focused on the output spectrum, particularly the amplitude at each frequency. We discovered that the distribution of peaks in the output spectrum varies with the input frequency, a result of the numerous harmonics present in the output. Furthermore, we demonstrated the brain's filtering effect, where higher frequencies generally correspond to weaker amplitudes.

We then assigned specific frequencies to a narrow band, encoding several peaks into this band as input to the nonlinear function. After applying some approximations, the experimental results of the output spectrum's peak distribution effectively verified our derived equations. Additionally, we extended this analysis to the double bands condition, and the experiments confirmed the accuracy of our derived equations.

In the case of broadband conditions, predicting the location of peaks can be achieved using a generator model. However, deriving analytical expressions for the amplitude of each frequency is complex, as it can be influenced by the human state. Therefore, we applied statistical analysis to each amplitude. Our findings indicate that the power of each frequency in the output spectrum follows an exponential distribution, albeit with different parameters. These parameters can be determined through calibration, especially by measuring the baseline.

Chapter 4

Human-Centred Physical Neuromorphics

4.1 Introduction

In the preceding chapter, we introduced various brain models, encompassing both narrowband and broadband conditions. In this chapter, we narrow our focus to the narrowband condition, which has potential applications in simple image transmission and the construction of a physical neural network.

Brain-computer interface (BCI) research is gaining increasing significance, particularly in the study of visual evoked potentials (VEPs). VEPs play a crucial role in establishing a connection between the human brain and external devices, such as computers [165, 195–197]. Among the various types of VEPs, steady-state visual evoked potentials (SSVEPs) stand out for their robustness and stability. These neural responses are generated in the visual cortex in reaction to periodic visual stimuli [171,172]. SSVEPs exhibit higher-order harmonics of the stimulus frequency, making them particularly effective for extracting specific signals from the brain. Techniques like FFT (Fast Fourier Transform) are commonly used to extract features from these responses, allowing for the extraction of meaningful information. For instance, by spatially separating lights flickering at different frequencies, SSVEPs corresponding to these frequencies can indicate the user's focused attention on a specific spatial region. Typically, a single frequency is used to tag the target, which corresponds to identifying the SSVEP frequency. However, there is a growing trend among researchers to use multi-frequency tagging to enhance the accuracy of classification. For example, by utilizing two frequencies, f_1 and f_2, "inter-modulation" occurs, leading to the appearance of spectral peaks at $f_1 \pm f_2$ in the SSVEP spectrum. Although this phenomenon is well-known, the physical origins of these inter-modulation components are not yet fully understood. They are generally modelled as arising from the intrinsic nonlinear response of individual neurons [175].

To date, SSVEPs have been excited using low-density frequency division multiplexing (FDM) techniques, where only a few light-modulation frequencies are employed with a single flickering light stimulus [171, 188, 198, 199]. The information rate of these systems is of order ~ 1 bit/second [195], with recent work showing information transfer rates up to 5 bits/second [197]. Whilst this is acceptable for some applications, it is still very far from the estimated ~ 10 Mb/s information capacity rate of the human visual system [200], implying that there may be room for applications beyond relatively simple '1-bit' BCI decision tasks. Indeed, it has been noted that whilst BCIs for machine control appear to be limited by a ceiling in terms of the information rate that actually translates into useful commands, the information transfer rate can be significantly larger and does not seem to have similar limitations [197].

Recent studies have demonstrated that the human visual system can be employed for tasks traditionally associated with computational imaging, such as single-pixel or ghost imaging [2, 43]. These findings suggest that an SSVEP-based BCI can, in principle, transmit and process enough information to reconstruct greyscale images.

In this study, a high-density frequency-division multiplexed SSVEP system is presented , which utilizes hundreds of frequencies to simultaneously encode and transmit information. Additionally, two applications were validated here, one is image transmission, which serves to test the effectiveness of the BCI, and another is simple classification tasks. The latter is achieved through the implementation of a physical neural network (PNN) that leverages SSVEPs. This PNN demonstrates strong performance in classification tasks, highlighting the potential of SSVEP-based BCIs for image processing and pattern recognition. Additionally, our results indicate that extending the SSVEP-PNN from a single-layer (i.e., a single brain) to a two-layer (i.e., two connected brains) configuration enhances classification performance, suggesting that our approach has inherent scalability potential.

4.2 High-density frequency division multiplexing of SSVEPs

Fig. 4.1 illustrates the experimental approach, where the input of the LED signal, called visual stimulus, can consist of an image (e.g., a handwritten digit) intended for transmission and subsequent decoding through the SSVEP from the BCI. Moreover, the input data is not limited to an image array and can include a set of values, which may be combined with a set of parameters. This latter scenario will be employed when utilizing the BCI as a physical neural network. Frequency division modulation is utilized in this approach, where each value is assigned as the amplitude of a specific frequency component. Consequently, the information is embedded into a time-domain signal composed of multiple frequencies. Specifically, for image data, each pixel index m is associated with a frequency f_m, and the value A_m corresponding to the pixel is used to modulate this frequency.

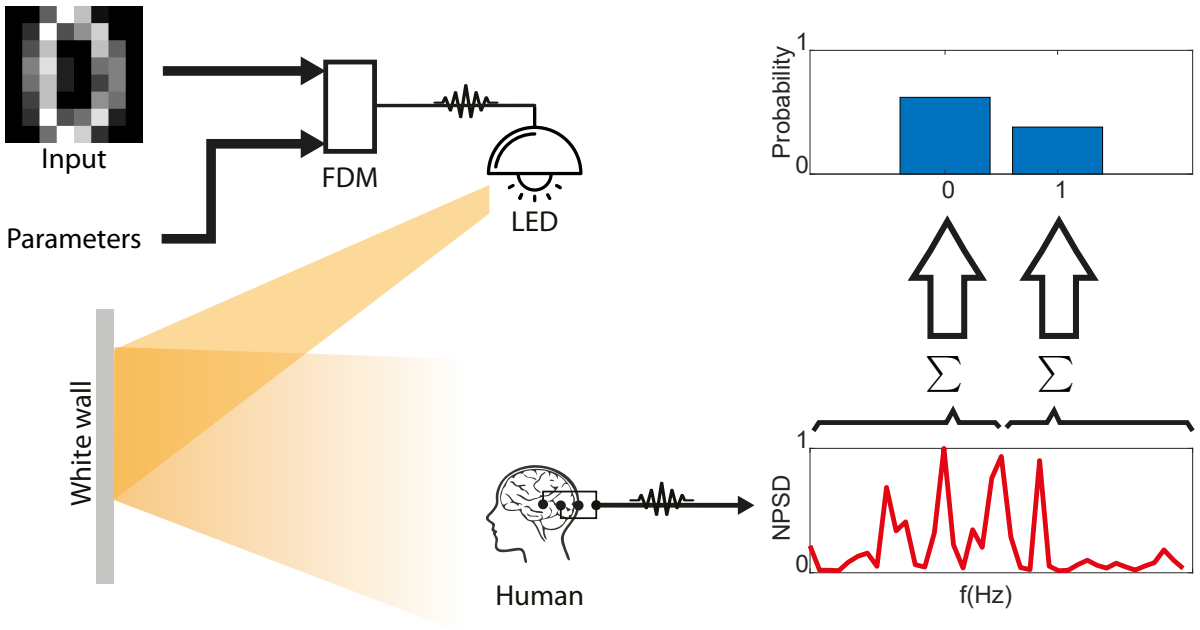

Figure 4.1: **BCI Setup.** Input data (shown is an example image of a handwritten digit "0" and a set of control parameters) are encoded in frequency division multiplexing. The frequency-encoded signal modulates the intensity of an LED light projected onto a white screen, which is observed by a participant. A 3-pole EEG device detects the steady-state visual evoked potential, with an active electrode placed at Oz (medial occipital electrode site) to capture the electric signal from the primary visual cortex, a reference electrode positioned above the left ear (M1 position), and a ground electrode located above the right ear (M2 position). The resulting normalized power spectrum density (NPSD) is utilized for image transfer or computational tasks. Figure taken from Ref. [4]

The sum of all these frequencies,

$$x(t) = \sum_{m=0}^{\mathrm{M}} A_m \cos(2\pi f_m t), \tag{4.1}$$

is then projected using an LED onto a white screen. We choose the frequencies to be $f_m = f_0 + m\delta f$, i.e. a set of M+1 frequencies, each separated by δf.
A participant equipped with an EEG device to record SSVEP signals [2] views light projected onto a white screen. Given that approximately M $\sim$ 200 different frequencies are encoded into the light modulation, the participant will perceive a light flicker that appears random rather than the standard periodic SSVEP signal typically encountered in conventional BCIs. Nonetheless, this flickering will exhibit a repeating pattern with a period $T = \frac{1}{\delta f}$.

The detected SSVEP manifests as a complex waveform, from which a normalized power spectral distribution (NPSD) can be derived, as illustrated in Fig. 4.1. This NPSD can then be utilized for either image reconstruction or neural network classification tasks.

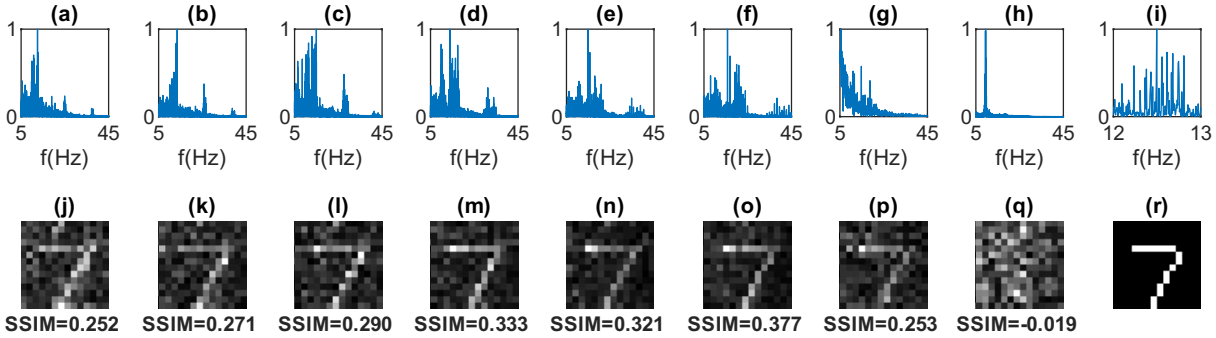

Figure 4.2: **BCI Image Transmission.** Experimental results are shown for a handwritten digit "7" image. The first row shows the SSVEP normalized power spectrum density (NPSD), produced by frequency division multiplexing following Eq. (4.1), with $f_0 = 12$ Hz, measurement time 196 seconds, and bandwidth a) 1 Hz, b) 2 Hz, c) 4 Hz, d) 8 Hz, e) 12 Hz, f) 16 Hz. g) is for 12 Hz bandwidth and a shorter measurement time of 16.3 seconds, while h) is for 12 Hz bandwidth with a blindfold (showing only an alpha wave peak at 10 Hz), and i) is a zoom of (a) from 12 to 13 Hz. The second row shows the reconstructed, grey-scale images corresponding to the data in the image directly above in the first. Each figure also shows the structural similarity index measure (SSIM) relative to the ground truth image, shown in (r). Figure taken from Ref. [4]

4.3 Image transmission

In this section, the transmission capabilities of our system are thoroughly examined using black-and-white 14×14 pixel handwritten images to evaluate its performance. Initially, the original 28×28 pixel handwritten digit images [201] are downsampled to a resolution of 14×14 pixels. Following this, the resulting image matrix is flattened into a vector, represented as $\left[A_0, ..., A_M\right]$, where the length of the vector is $\mathrm{M}+1 = 196$. The amplitudes A_m, which take on binary values of 0 or 1, are encoded into a time-domain signal. The maximum light intensity projected onto the screen by the red LED, which has a wavelength of 640 nm, is set to 8 cd.

The outcomes related to the transmission of the digit "7" are depicted in Figure 4.2 for a base frequency $f_0 = 12$ Hz and varying frequency spacings δf. These spacings correspond to total SSVEP bandwidths of 1, 2, 4, 8, 12, and 16 Hz and are respectively showcased in Figures 4.2(a) through (f). Figure 4.2(h) presents the measured signal with the participant blindfolded (no stimulus), where only the alpha peak at 10 Hz is observable. This 10 Hz alpha rhythm is a well-known neural oscillation typically associated with relaxed states or closed-eye conditions [202–204]. When the subject is blindfolded, the lack of visual stimuli leads to an increase in alpha wave activity in the brain, which is primarily detected over the occipital cortex. This confirms that the recorded signals in other figures, which include additional brain activity, are authentically generated by the brain and not influenced by external visual stimuli. An enlargement of the spectrum for a 1 Hz bandwidth is displayed in Figure 4.2(i). Figures 4.2(j) to (q) exhibit the reconstructed images, which are derived by utilizing the amplitude of each frequency component from the measured Noise Power Spectral Density (NPSD) and reallocating it to the

corresponding pixel in the image. It should be noted that for Figures 4.2(a) to (f), the data acquisition time was 196 seconds, which corresponds to a single full period, $T = 1/\delta f$, for the narrowest bandwidth of 1 Hz. More details about the image retrieval technique can be found in Chapter 4.7.

The Frequency Division Multiplexing (FDM) SSVEP method can successfully reconstruct the original image, known as the ground truth, as depicted in Figure 4.2(r). As the overall bandwidth increases, there is a noticeable reduction in noise, owing to the acquisition of multiple periods (from 1 Hz to 16 Hz across Figures 4.2(j) to (o)). Each figure also presents the SSIM, which quantifies the resemblance between the retrieved images and the ground truth. The SSIM indeed indicates a steady improvement in similarity with an increasing number of measurement periods. However, a comparison between the single period measurement results for 1 Hz (Figure 4.2(j)) and 12 Hz (Figure 4.2(p)) bandwidths reveals that the shorter 16.3-second acquisition time at 12 Hz bandwidth yields a reconstruction of comparable quality. These findings suggest a trade-off between the signal-to-noise ratio in the transmitted data, the acquisition time, and the bandwidth. There appears to be a distinct advantage to utilizing as broad bandwidth as feasible across the EEG spectrum for optimal results.

These considerations must be carefully balanced against the highly nonlinear nature of neuronal responses observed in these measurements. When the bandwidth exceeds $2 \times f_0$, harmonic and intermodulation signals are generated at frequencies that can overlap with the original input frequencies. In the subsequent analysis, we demonstrate how these intermodulation frequencies can be strategically utilized for more sophisticated computations by selectively determining the operating bandwidths.

4.4 Physical Neural Networks based on SSVEP-based BCI

In this section, we first demonstrate the image classification process to showcase the computational capabilities of the SSVEP-based BCI system.

This approach draws inspiration from previous research on reservoir computing and extreme learning machines, which have been effectively used for classifying complex data sets [117–120, 134,205–212]. Additionally, recent advancements have shown that physical systems, when combined with controllable parameters—often termed as learnable "weights"—can achieve similar outcomes [117]. These methods rely on the nonlinearity inherent in the system to mix input data with these parameters, and subsequently train the system to improve classification accuracy for new, unseen data. In our setup, we leverage this concept by encoding extensive data into a neural network framework, utilizing the nonlinearity of the neural response to perform mixed processing of the input data.

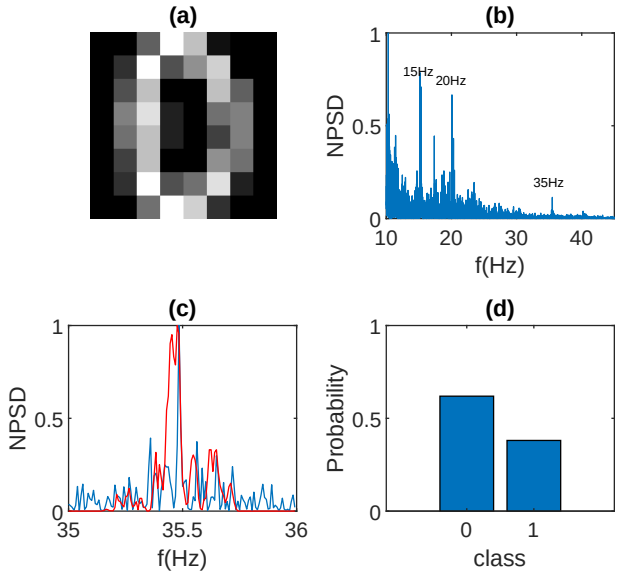

Figure 4.3: **BCI physical neural network Image Classification.** Experimental results from a single classification experiment of handwritten digits “0" and “1". a) An example of input data, a greyscale 8x8 pixel digit “0". b) Measured EEG signal NPSD with three highlighted frequency intervals: the input image frequency-encoded as 64 equidistant frequencies in the $[15.0, 15.5]$ Hz range; the control parameters (determined by a genetic algorithm(GA)) frequency-encoded as 64 frequencies in the $[20.0, 20.5]$ Hz range; and the 128 intermodulation frequencies in the $[35, 36]$ Hz range. There are several reasons to optimize the control parameters using a GA rather than a back-propagation (BP) algorithm. One key reason is that the control parameters are binary, which makes them well-suited for configuration via GA but challenging to handle effectively using BP. c) The decoded intermodulation signal in more detail; the blue curve is a magnification of the measured signal in (b), and the red curve is the synthetic (numerically simulated) data. d) The readout probability distribution over the two classes “0" and “1" showing a correct classification (highest probability) for “0". Figure taken from Ref. [4]

To demonstrate the feasibility of constructing a physical neural network classifier, we commence with the fundamental task of classifying the digits "0" and "1" from a dataset comprising 8x8 pixel handwritten digit images, as referenced in [213]. An illustrative example is depicted in Fig 4.3(a). By undertaking this task, we aim to explore the potential application of physically realized neural networks in the realm of pattern recognition.

Fig 4.2 illustrates a straightforward image transmission scenario. In contrast, our current focus shifts to the realm of image classification, which is grounded in the physical neural network framework. Within this framework, we integrate the input image with control parameters, the latter of which are encoded in an additional frequency band. As two bands—input data and control parameters—are utilized here, the overall frequency-encoded signal is accordingly defined as $X(f) + \alpha(f)$ over two distinct narrow bands. The mathematical formulation in the positive

frequency domain is expressed as:

$$\begin{aligned} X(f) &= \sum_{m=0}^{M} A_m \delta(f - f_m), \\ \alpha(f) &= \sum_{m=M+1}^{M+P} A_m \delta(f - f_m), \end{aligned} \tag{4.2}$$

with δ the Dirac delta function.

As illustrated in Eq. (4.2), $X(f)$ and $\alpha(f)$ represent the encoded image information and control parameters, respectively. The former is confined within the frequency band $[f_0, f_M]$, while the latter resides within the frequency band $[f_{M+1}, f_{M+P}]$. Additionally, the frequencies f_m are defined as in Eq. (4.1). More importantly, the two bands must be distinctly separated without any overlap, which will facilitate the simplification of the model. This separation ensures that the intermodulation frequency region, resulting from the mixing between the image and control parameter frequencies, does not coincide with any intervals of linear or second-harmonic signals.

The image encoding process mirrors that of the image transmission task. The identical methodology is applied to the α-signal, with comprehensive definitions furnished in Chapter 4.7. The input pixel matrix or vector is transformed into a one-dimensional greyscale vector, represented as $\left[A_0, ..., A_M\right]$, where the amplitudes A_m assume normalized values within the range $[0, 1]$. These values are proportional to the greyscale intensities, with black equating to 0 and white to 1.

Fig 4.3(b) presents an exemplary outcome of our experiment, where we selected bandwidths of 0.5 Hz for both X and α signals, each consisting of 64 frequency components. These components commence at frequencies $f_0 = 15$ Hz and 20 Hz, respectively. The spectral components within the input frequency ranges are denoted as '15' and '20' Hz, and we also emphasize the intermodulation frequency band at 35 Hz, which encompasses a total bandwidth of 1 Hz. It is observed that the second harmonic signals at 30 Hz and 40 Hz are just perceptible above the noise floor, while the intermodulation signal exhibits a considerably higher contrast. The intermodulation signal is shown in more detail in Fig. 4.3(c) where the blue line represents the measured NPSD and the red curve shows the numerically simulated NPSD, with a relatively good agreement between them, indicating that the physical neural network can be optimised using synthetic data from numerical simulations. The numerical model used in this work is described in Chapter 4.7 but in brief, this is based on the phenomenological observation that for a given set of input frequencies, the output SSVEP spectrum will contain the same input signals together with harmonics and intermodulation frequencies. The latter second-order frequencies are then weighted with a function $\tilde{\chi}^{(2)}$, as described in Chapter 4.7, whose shape is determined from measurements and is found to be universal (i.e. independent of the EEG user). This model can then be used to simulate a large number of different experiments using e.g. a set of MNIST digits, which in turn

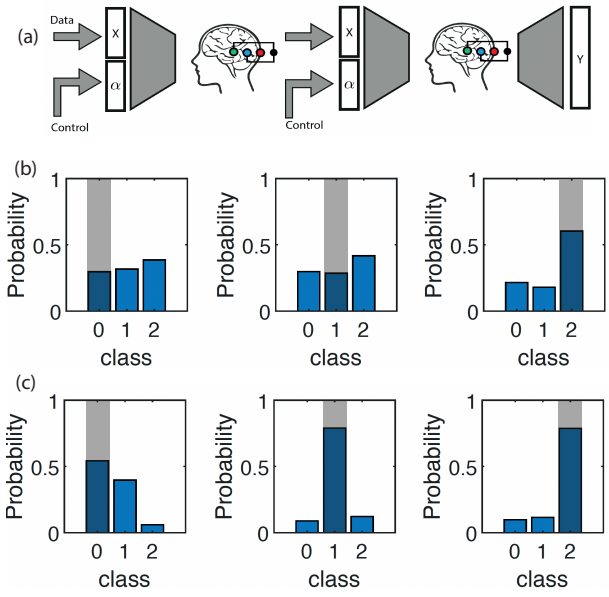

Figure 4.4: **Single and Multi-layer physical neural network classification.** (a) Schematic architecture of the two-layer PNN. (b) Classification probabilities for the single layer PNN applied to the Iris dataset with 3 classes. Correct classifications are indicated with gray bars. (c) Classification probabilities for the two-layer PNN applied to the same Iris dataset. All three classifications are now correct, and classification probabilities are significantly improved, from $\sim 50\%$ or less, now up to close to $\sim 80\%$. Figure taken from Ref. [4]

are then used to learn the optimal α parameters with a genetic algorithm [214]. These α values are then used in experiments where we now collect actual EEG data from unseen examples of out-of-sample digits and perform classification.

Fig 4.3(c) illustrates the intermodulation signal depicted by the blue line, alongside the numerically simulated NPSD represented by the red curve. Both exhibit a relatively good agreement, suggesting that the numerical model, detailed in Chapter 4.7, aligns well with the Physical Neural Network (PNN) model. This compatibility indicates that the PNN model can be refined using synthetic data derived from numerical simulations. The numerical model is founded on phenomenological observations, which can be succinctly summarized as follows: for a given ensemble of input frequencies, the resulting output steady-state visually evoked potential (SSVEP) spectrum will encompass the original input signals, along with their harmonics and intermodulation frequencies. These latter second-order frequencies are then weighted by a function $\tilde{\chi}^{(2)}$, as delineated in Chapter 4.7. The form of this function is ascertained from empirical measurements and is observed to be universal, meaning it remains consistent across different EEG users. Furthermore, this model can be employed to simulate a multitude of diverse experiments, for instance, utilizing a collection of MNIST digits. These simulations are subsequently leveraged to ascertain the optimal α parameters through a genetic algorithm, as referenced in [214]. The

identified α values are then implemented in experiments where actual EEG data is gathered from previously unseen exemplars of out-of-sample digits, facilitating the classification process. Fig. 4.3(d) illustrates the classification results for experimental data of unseen out-of-sample digits, where the classification probability over the two classes "0" and "1" is depicted. In general, within this work, classification probabilities are derived by segmenting the intermodulation frequency range into several segments that correspond to the number of classes. We then calculate the total power fraction within each frequency segment to represent the classification probability.

Several experiments are conducted and detailed in Chapter 4.7, where we demonstrate that the SSVEP-based physical neural network is adept at accurately classifying the digits "0" and "1". Furthermore, in Chapter 4.7, we exhibit supplementary instances of handwritten digit classification, in conjunction with other tasks associated with diverse data sets, including tumour biopsy data and classification endeavours. These scenarios are characterized by their simplicity as two-class classification tasks, and while the classification results are acceptable, there is room for improvement. In light of this, we have delved into strategies to augment the classification probability and broaden the spectrum of discernible classes.

4.5 Multi-layer physical neural network

To achieve enhanced capability and performance, one potential strategy is to increase the number of nodes in the SSVEP physical network by augmenting the number of frequencies subject to encoding. However, this approach may incur the disadvantage of increased bandwidth consumption and/or heightened frequency density, which could consequently prolong the measurement time. Taking this into account, we have devised an alternative approach: utilizing a single network layer but increasing the number of layers. This method maintains the simplicity of a single-layer experiment while potentially yielding superior results. We propose to use the output of the first layer as the input for the second layer, employing a distinct set of control parameters α' for the subsequent layer (as schematically depicted in Fig. 4.4). This secondary loop functions as the second layer within the overall network, utilizing two sets of control parameters, namely α and α'. Furthermore, the same numerical model can be applied to train these control parameters effectively.

It can be observed that the number of output elements from the first layer is approximately double the input size of that layer, which is the sum of the length of α and the length of x. To ensure compatibility with the second layer, the middle portion of the output is selected as the input to the second layer, allowing the number of elements to match accordingly.

The outcomes of this ‘connected brain’ methodology are delineated in Figure 4.4. It evidences a marked enhancement in the classification accuracy across three classes. The Iris flower dataset [215] serves as the basis for this experiment, engaging 5 input parameters. These parameters’

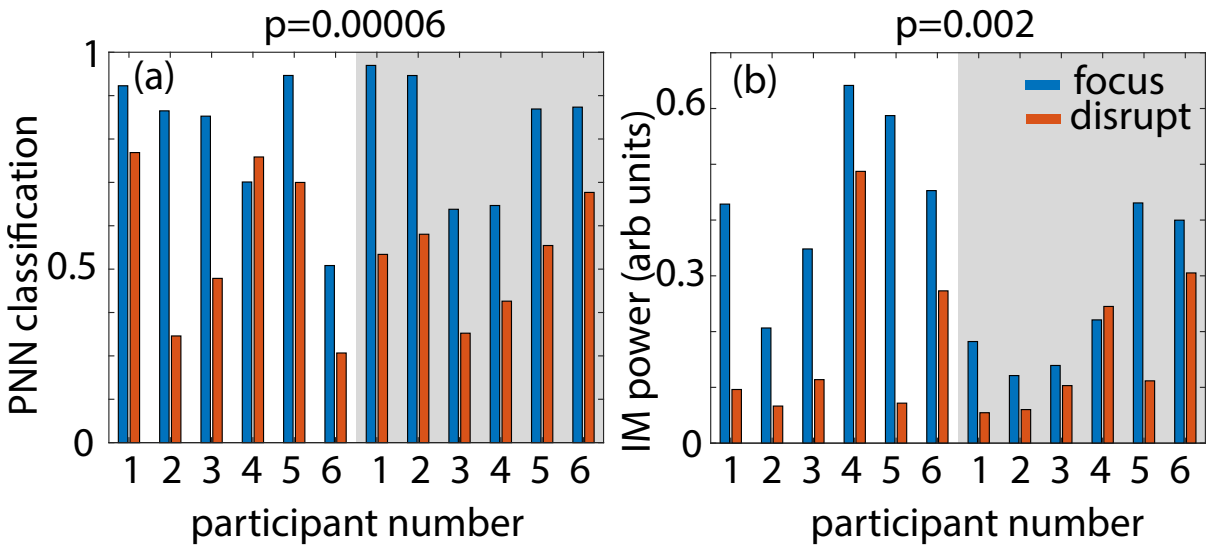

Figure 4.5: **Effect of attention on physical neural network classification and on the intermodulation (IM) frequency power.** (a) Classification for a two-layer (brain) PNN with 6 participants, each acting only as the second layer (the first layer is fixed, participant 1). Participants are asked to 'focus' attention on the light flicker or 'disrupt' attention by mentally performing mathematical operations (number additions, subtractions, divisions) for the duration of the light flicker (200 seconds). In all cases, participants fixate on the illuminated area of the screen. Each participant was measured twice, several minutes apart, inverting the order of the 'focus' and 'disrupt' condition, so as to exclude a possible confounding effect of the temporal order in which the conditions were performed. We found that PNN classification accuracy ($t(5)=6.29$, $p=0.00006$) and the intermodulation frequency power ($t(5)=4.18$, $p=0.002$) were statistically significantly reduced during the 'disrupt' compared to the 'focus' condition. These results indicate that indeed, human attention can directly modify the effectiveness of the multilayer brain connection and PNN computing efficiency. Figure taken from Ref. [4]

values were downsampled to a 2-bit depth and subsequently encoded into $5\times 2 = 10$ 1-bit frequency constituents. The performance of a single network layer is portrayed in Figure 4.4(b), where the classification accuracy approximates random guessing (correct classifications are demarcated with grey bars), and the overall classification probabilities are quite low (around 50% or less). Nevertheless, upon progression to a 2-layer network architecture, as illustrated in Figure 4.4(c), there is a noticeable amelioration in classification efficacy, with the classification probability elevated to 80% or higher.

As previously mentioned, the numerical model serves as a versatile tool for simulation, requiring no customization for different individuals. It is capable of emulating these experiments and training the physical neural network, which is both straightforward and robust. The two-layer network can be implemented by a single participant or two distinct participants. The detailed results are presented in Chapter 4.8.

In our final observation, we highlight that, while neural networks can manifest through diverse physical systems such as photonic, acoustic, and hydrodynamic ones, often yielding superior

outcomes [216–219], the distinctive attribute of a brain-based physical neural network is undoubtedly the integration of the human brain and related elements into the system. Notably, human attention significantly influences the SSVEP response, as demonstrated in [171]. This suggests that attention could directly alter the performance of a PNN. To test this, we conducted a two-layer classification task with six participants, each serving as the second layer of the network. In this experiment, we investigated the impact of attention and cognitive interference on classification accuracy and intermodulation frequency power during visual stimulation with a flickering light. The experimental setup is illustrated in Fig. 4.1. Participants were seated comfortably in front of a screen displaying a flickering stimulus, with their EEG signals recorded throughout the session.

Each participant underwent two distinct experimental conditions: *focus* and *disrupt*. In the *focus* condition, participants were instructed to direct their full attention to the flickering light, maintaining a consistent and intentional focus on the stimulus. Conversely, in the *disrupt* condition, participants engaged in mental arithmetic tasks (e.g., continuous subtraction or multiplication) while simultaneously observing the flickering light. These tasks were designed to impose cognitive load and divert attention away from the visual stimulus.

To mitigate potential temporal confounding effects, the order of the *focus* and *disrupt* conditions was alternated across participants, for example, *focus* and *disrupt* and then followed by *disrupt* and *focus*. Each condition lasted for 60 seconds, with sufficient rest intervals provided between trials to prevent fatigue. The EEG data were analysed to extract both the classification accuracy of the neural response patterns and the power of the intermodulation frequencies elicited by the flickering stimulus.

Statistical analysis of the results revealed significant differences between the two conditions. Classification accuracy was markedly reduced during the *disrupt* phase ($t(5) = 6.29$, $p = 0.00006$) compared to the *focus* phase. Similarly, the total power of intermodulation frequencies decreased significantly during the *disrupt* phase ($t(5) = 4.18$, $p = 0.002$). These findings suggest that the engagement of cognitive resources in tasks unrelated to the flickering light diminishes the brain's capacity to process and respond to the stimulus, as evidenced by reduced neural synchrony and intermodulation frequency power.

This study highlights the critical role of human attention in modulating the efficacy of multilayer brain connectivity and computational processes, with implications for understanding the interplay between attention, neural dynamics, and cognitive interference.

4.6 Conclusions

By embracing an approach analogous to that used in other domains, such as wavelength division multiplexing in optical telecommunication systems, we have demonstrated the potential to substantially expand the scope of SSVEP-based BCIs. Implementing a high-density frequency multiplexing strategy enables the parallel encoding and transmission of information across numerous channels, with the flexibility to customize this encoding for various applications. We have illustrated that image data can be effectively conveyed, achieving higher image quality with increased bandwidths. Conversely, employing narrow bandwidth encoding across a multitude of frequency channels efficiently stimulates and isolates intermodulation frequencies. This lays the groundwork for the development of SSVEP-based physical neural networks that leverage the capacity to multiply control parameters with input data, thereby creating a fully interconnected neural layer.

The foundational model for SSVEP has proven to be sufficiently straightforward and robust, applicable to any participant. This suggests that the same model can be utilized to extend this methodology to a multilayered structure, connecting multiple brains and enhancing the capabilities of the physical neural network. The progress in SSVEP generation through high-density frequency encoding presents considerable promise for applications in assistive and diagnostic technologies. Enhancing the robustness and scalability of SSVEP-based BCIs can lead to more seamless and efficient human-machine interactions.

Further exploration is warranted into the role of human attention within the combined human-AI computational capacity, particularly regarding its potential applications in diagnosing attention focus and fatigue. This could also extend to the auditory paradigm, offering new avenues for research and development in this field.

4.7 Methods

4.7.1 SSVEP Image Retrieval

In the previous sections, we detail the EEG measurements for Figs. 4.2(a)-(e), which are taken over a period $T = 196$ s. This measurement time is the inverse of the frequency resolution, specifically $T = \frac{1}{\delta f}$, and applies to the encoding signal with the longest duration as shown in Fig. 4.2(a), which has a bandwidth of 1 Hz. On the other hand, the measurement depicted in Fig. 4.2(f) is completed in a shorter time span of $T = 16$ s, corresponding to a bandwidth of 12 Hz. Additionally, as per the convention used throughout this paper, all EEG output spectra reported in Figs. 4.2(a)-(g) are normalized to the maximum output signal value. The greyscale reconstructed images are presented in the second row of Fig. 4.2. In this representation, the NPSD normalization constant is indicated by the colour white, while the absence of signal, or

zero value, is depicted by black. The intermediate shades of grey are calculated on a proportional basis. Specifically, for a given encoding frequency with Power Spectral Density (PSD) denoted by x, the corresponding grey tone is determined by the ratio $\frac{x}{x_{\max}}$. In this work, a unique instance is presented where the encoding and decoding processes for a specific task, due to its lower complexity, utilize an identical vector quantization strategy. This strategy involves representing the signals as linearly-indexed vectors of amplitudes that correspond to matched frequency distributions. As observed in the SSVEP NPSDs depicted in Figs. 4.2(a)-(f), higher-order harmonics emerge, with a significant focus on sum frequency generation (SFG) resonances. This observation is particularly noteworthy. Given the need to enhance information integration in more complex tasks, we opt to perform PNN decoding within the SFG regime. This choice is strategic, aiming to leverage the distinct characteristics of SFG resonances observed in the SSVEP NPSDs for effective decoding.

4.7.2 Our SSVEP Training Model

Inspired by established models in the field of nonlinear optics [192], we have developed a phenomenological model that encapsulates the intricacies of our SSVEP experiment.

In the frequency domain, Eq. (4.1) becomes

$$\tilde{x}(\omega) = \pi \sum_{m=0}^{M} A_m \left[\delta(\omega-\omega_m)+\delta(\omega+\omega_m)\right], \tag{4.3}$$

with the Fourier transform (FT)

$$\tilde{x}(\omega) = \int_{-\infty}^{+\infty} \mathrm{d}t\, x(t) e^{\iota\omega t},$$

the inverse Fourier transform (IFT)

$$x(t) = \frac{1}{2\pi} \int_{-\infty}^{+\infty} \mathrm{d}\omega\, \tilde{x}(\omega) e^{-\iota\omega t},$$

and $\omega = 2\pi f$.

As shown in Eq (4.4), we define the EEG signal as a sum of contributions from each harmonic amplitude, represented by $\tilde{\chi}^{(n)}(\omega)$, with the Fourier transform operator $\mathcal{F}$.

$$\tilde{y}(\omega) = \sum_{n=1}^{N} \tilde{\chi}^{(n)}(\omega) \mathcal{F}\left[x^n\right](\omega) = \sum_{n=1}^{N} \tilde{y}^{(n)}(\omega), \tag{4.4}$$

In some implementations of our BCI, a quadratic activation function is incorporated in the read-out process, yielding a final output that is the square of the norm of the signal, as shown in Eq (4.5).

$$y_{out}(\omega) = ||y(\omega)||^2. \tag{4.5}$$

Starting from Eq. (4.1) with $M \geq 1$ and FDM defined as

$$0 \ll \omega_a - \frac{\mathrm{d}\omega}{2} \leq \omega_0 \leq \omega_1 \leq ... \leq \omega_M \leq \omega_a + \frac{\mathrm{d}\omega}{2}, \tag{4.6}$$

such that it is confined into a narrow band, we get an SFG profile as

$$Y_{SFG}(\omega) = \frac{\pi}{2}\tilde{\chi}^{(2)}(\omega)[X * X](\omega). \tag{4.7}$$

More details about the derivation of the latter equation are reported in the SSVEP Phenomenon Model section.
Considering two distinct narrow bands involves defining a set of conditions as

$$\begin{gathered} 0 \ll \omega_a - \tfrac{\mathrm{d}\omega}{2} \leq \omega_0 \leq ... \leq \omega_M \leq \omega_a + \tfrac{\mathrm{d}\omega}{2}, \\ \omega_a + \mathrm{d}\omega < \omega_b < 2\omega_a - \mathrm{d}\omega, \\ \omega_b - \tfrac{\mathrm{d}\omega}{2} \leq \omega_{M+1} \leq ... \leq \omega_{M+P} \leq \omega_b + \tfrac{\mathrm{d}\omega}{2}. \end{gathered} \tag{4.8}$$

The corresponding input spectrum, when we remove the difference frequency generation (DFG) terms and then we impose $\omega > \mathrm{d}\omega$, is defined by $X(\omega) + \alpha(\omega) = \sum_{m=0}^{M+P} A_m \delta(\omega - \omega_m)$, with $X(\omega)$ and $\alpha(\omega)$ defined as

$$\begin{aligned} X(\omega) &= \sum_{m=0}^{M} A_m \delta(\omega - \omega_m), \\ \alpha(\omega) &= \sum_{m=M+1}^{M+P} A_m \delta(\omega - \omega_m), \end{aligned} \tag{4.9}$$

like in Eq (4.2), with the added constraint that $\sum_{m=0}^{M} A_m^2 = \sum_{m=M+1}^{M+P} A_m^2 = 1$ to ensure a balanced distribution of amplitudes between the two signals.
Eqs. (4.7,4.9) imply that the pure SFG profile, generated by sums of one input and one control frequency, is now given by

$$Y_{X+\alpha}(\omega) = \frac{\pi}{2}\tilde{\chi}^{(2)}(\omega)[X * \alpha](\omega), \tag{4.10}$$

as proven by Eq. (4.16) in the SSVEP Phenomenon Model section.
We wish to emphasize that, despite the superficial linearity of the equation, the system's physical behaviour is fundamentally nonlinear. This nonlinearity is primarily attributed to the overall amplitude coupling, given that all amplitudes are derived from a common LED source. To elucidate the mathematical implications of this inherent nonlinearity, let us consider a scenario where the signals are subjected to perturbative white noise, denoted by ξ, and potentially experience an amplification in LED intensity by a factor of σ. In such a case, the transformation of our signals can be described as follows:

$$X' = \sigma X + \xi, \;\; \alpha' = \sigma\alpha + \xi. \tag{4.11}$$

Subsequently, Eq. (4.10) can be expressed as:

$$Y_{X'+\alpha'} = \frac{\pi}{2}\tilde{\chi}^{(2)}\left[\sigma^2 X * \alpha + \sigma(X+\alpha) * \xi\right], \tag{4.12}$$

This formulation emphasizes the impact of noise and amplitude scaling on the signal transformation, which introduces additional uncertainty and perturbations into the system, in contrast to a simpler linear reservoir.

4.8 SSVEP Phenomenon Model

4.8.1 Derivation of SSVEP Model Equations

To derive Eq. (4.7), without loss of generalization, we show here the computation of the second-order EEG signal in Eq. (4.4) in the simplest case $M = 1$:

$$\begin{aligned}
\tilde{y}^{(2)}_{r,M=1}(\omega) &= \tilde{\chi}^{(2)}(\omega)\mathcal{F}\left[x^2_{M=1}\right](\omega) = \\
&= \tfrac{\pi}{2}\tilde{\chi}^{(2)}(\omega)\left\{2\left(A_0^2 + A_1^2\right)\delta(\omega) + \right. \\
&+ A_0^2\left[\delta(\omega - 2\omega_0) + \delta(\omega + 2\omega_0)\right] + A_1^2\left[\delta(\omega - 2\omega_1) + \delta(\omega + 2\omega_1)\right] \\
&+ \left. 2A_0A_1\left[\delta(\omega - \omega_0 - \omega_1) + \delta(\omega + \omega_0 - \omega_1) + \delta(\omega - \omega_0 + \omega_1) + \delta(\omega + \omega_0 + \omega_1)\right]\right\} \approx \\
&\approx \tfrac{\pi}{2}\left\{\tilde{\chi}^{(2)}(0)\left[2\left(A_0^2 + A_1^2\right)\delta(\omega) + 2A_0A_1\left(\delta(\omega + \omega_0 - \omega_1) + \delta(\omega - \omega_0 + \omega_1)\right)\right] + \right. \\
&+ \tilde{\chi}^{(2)}(2\omega_a)\left[A_0^2\left(\delta(\omega - 2\omega_0) + \delta(\omega + 2\omega_0)\right) + A_1^2\left(\delta(\omega - 2\omega_1) + \delta(\omega + 2\omega_1)\right) + \right. \\
&+ \left. \left. 2A_0A_1\left(\delta(\omega - \omega_0 - \omega_1) + \delta(\omega + \omega_0 + \omega_1)\right)\right]\right\}.
\end{aligned} \tag{4.13}$$

In Eq. (4.13), the function $\tilde{\chi}^{(n)}(\omega)$ is approximated to their values in $0, 2\omega_a$ because they are supposed to be symmetric with respect to $\omega = 0$ and $|\omega_{1,2} - \omega_a| \leq \mathrm{d}\omega$.
Let us now consider only $\omega > 0$. Eq. (4.13) gets reduced to

$$\begin{aligned}
\tilde{y}^{(2)}_{r,M=1}(\omega > 0) &= \frac{\pi}{2}\tilde{\chi}^{(2)}(\omega)\left\{A_0^2\delta(\omega - 2\omega_0) + A_2^2\delta(\omega - 2\omega_1) + 2A_0A_1\left[\delta(\omega - \omega_0 - \omega_1) + \delta(\omega + \omega_0 - \omega_1)\right.\right. \\
&\approx \frac{\pi}{2}\left\{\tilde{\chi}^{(2)}(0)\underbrace{\left[2A_0A_1\delta(\omega + \omega_0 - \omega_1)\right]}_{\text{DFG}} + \right. \\
&+ \left.\left.\tilde{\chi}^{(2)}(2\omega_a)\underbrace{\left[A_0^2\delta(\omega - 2\omega_0) + A_1^2\delta(\omega - 2\omega_1) + 2A_0A_1\delta(\omega - \omega_0 - \omega_1)\right]}_{\text{SFG (including SHG)}}\right\}.
\end{aligned} \tag{4.14}$$

If we consider just $\omega > \mathrm{d}\omega$, only the part referring to the SFG (with second harmonic generation (SHG) considered as an SFG from equal fundamental harmonics) remains.
The last step to get Eq. (4.7) is to exploit the convolution properties of the Dirac delta functions. Indeed, once defined redefined Eq. (4.3) as

$$X(\omega) = \sum_{m=0}^{M} A_m\delta(\omega - \omega_m), \tag{4.15}$$

one can see that Dirac delta functions allow us to move easily from continuous to discrete representations and back; that is, from Eq. (4.7) to Eq. (4.14) and vice versa.
The same holds true for the two narrow bands case described in Eq. (4.9):

$$\begin{aligned}
Y_{SFG}(\omega) &= \frac{\pi}{2}\tilde{\chi}^{(2)}(\omega)[(X + \alpha) * (X + \alpha)](\omega) = \\
&= \frac{\pi}{2}\tilde{\chi}^{(2)}(\omega)\left[\underbrace{X * X}_{\in[2\omega_a - \mathrm{d}\omega; 2\omega_a + \mathrm{d}\omega]} + 2\underbrace{\alpha * X}_{\in[\omega_a + \omega_b - \mathrm{d}\omega; \omega_a + \omega_b + \mathrm{d}\omega]} + \underbrace{\alpha * \alpha}_{\in[2\omega_b - \mathrm{d}\omega; 2\omega_b + \mathrm{d}\omega]}\right](\omega),
\end{aligned} \tag{4.16}$$

which implies Eq. (4.10).

4.8.2 Single-Layer SSVEP BCI Classifier: Further Results

The results of the handwritten digit image classification using our SSVEP-based BCI - shown

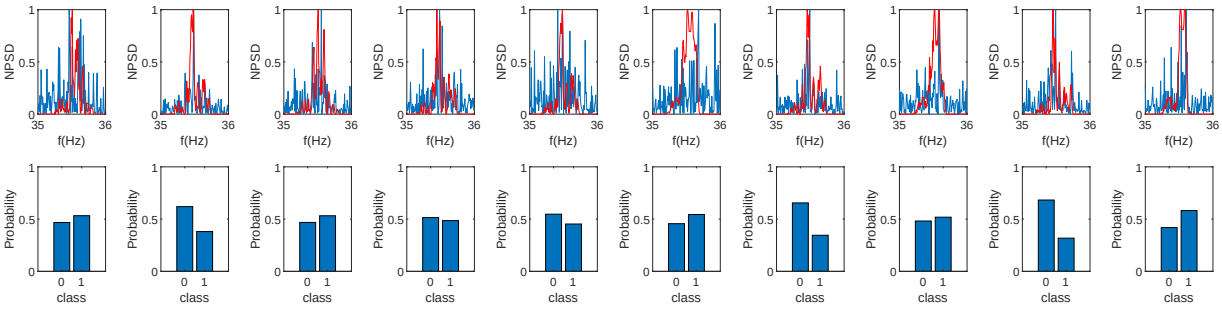

Figure 4.6: **BCI Image Classification: PNN Results.** Results of classification experiments of greyscale handwritten digits “0" and “1", downsampled to 8×8 pixels. EEG-measured spectra in the SFG regime are reported in blue in the first row, while red lines represent synthetic data. Corresponding readout probability distributions over the two classes “0" and “1" are shown in the second row. Each spectrum is correctly classified. Figure taken from Ref. [4]

Table 4.1: Example of one breast cancer dataset feature vector, extracted from a biopsy sample, and its encoding into a binary vector, as further detailed in Fig. 4.7. The first term, i.e. bias, is arbitrarily added.

No	Name	Value	Code
0	Bias	0.50	{1,0}
1	Clump thickness	0.44	{1,0}
2	Uniformity of cell size	1.00	{0,1}
3	Uniformity of cell shape	1.00	{0,1}
4	Marginal Adhesion	0.22	{0,0}
5	Single epithelial cell size	0.67	{1,0}
6	Bare nuclei	0.22	{0,0}
7	Bland chomatin	0.78	{0,1}
8	Normal nucleoli	1.00	{0,1}
9	Mitoses	0.11	{0,0}

in Fig. 4.3 - are more broadly presented in Fig. 4.6, demonstrating the effectiveness and limits of our approach in classifying handwritten digits “0" and “1".

To highlight the versatility of our SSVEP-based BCI in computational tasks, we demonstrate its capabilities as a classifier for a multivariate breast cancer dataset [220]. This further proves our PNN ability to handle various data types, from images to lists of numerical values.

In the breast cancer dataset, each datum is a 9-dimensional numerical feature vector, extracted from biopsy samples and labelled according to the nature of the breast cancer as either *benign* or *malignant*. In transforming feature vectors into frequency-encoded signals, we initiate a series of preprocessing steps, outlined in Table 4.1 and visualized in Fig. 4.7. This conversion begins with resizing each feature, denoted as x, to fit within a rescaled range of $[0,1]$. The formula for this normalization is $\frac{x-x_{\min}}{x_{\max}-x_{\min}}$, where $x_{\min}$ and $x_{\max}$ signify the minimum and maximum values

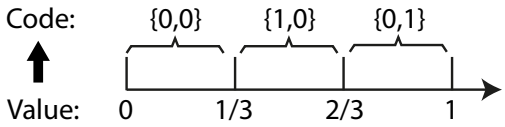

Figure 4.7: **Breast Cancer Dataset Encoding.** Strategy to encode the biopsy normalized parameters - like the one of a feature vector shown in Table 4.1 - in the first three classes of binary numbers. Figure taken from Ref. [4]

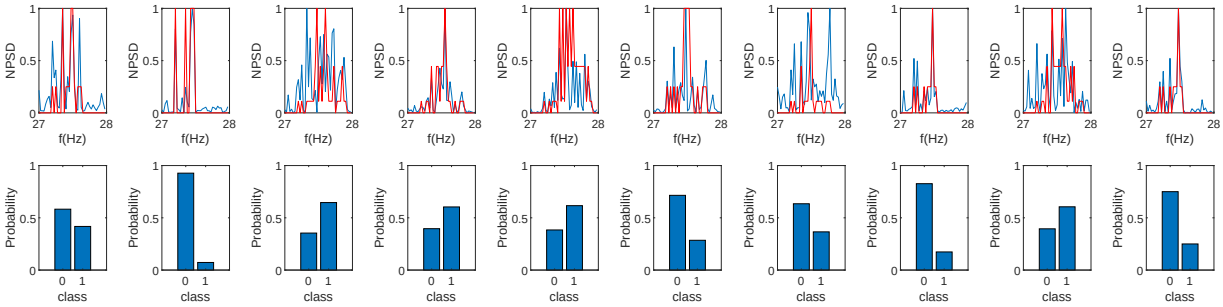

Figure 4.8: **BCI Breast Cancer Multivariate Dataset Classification: PNN Results.** Results of classification experiments of *benign* and *malignant* cancers. EEG-measured spectra in the SFG regime are reported in blue in the first row, while red lines represent synthetic data. Corresponding readout probability distributions over the two classes *benign* (labelled "0") and *malignant* (labelled "1") are shown in the second row. Only the seventh spectrum is not correctly classified. Figure taken from Ref. [4]

across the dataset, respectively. This ensures that the NPSD normalization constant is represented by white, the average background noise by black, and intermediate grey tones are determined in proportion. Following normalization, a vector quantization process is implemented, utilizing a 2-bit codebook that consists of the values $\{00, 10, 01\}$ and a partition scheme of $\{0, \frac{1}{3}, \frac{2}{3}, 1\}$, as shown in Fig. 4.7. To guarantee representation even when all feature vectors are encoded as zeros, a bias feature, coded as $\{10\}$, is appended to the dataset. For example, given the original feature values of $\{0.1, 0.4, 0.9\}$, the transformation results in a binary vector sequence $\{10001001\}$. This systematic conversion culminates in the original 9×1 feature vectors being expanded into binary feature vectors with dimensions of 20×1, thereby preparing them for the frequency encoding stage.

In the testing phase, encoding is applied comprehensively to both the test data and the control parameters. These are transformed into narrowband stimuli for modulation of an LED at frequencies of approximately 12 Hz and 15 Hz, respectively. This encoding strategy ensures that the stimuli are precisely controlled at the designated frequencies. The results of these encoding processes, which are crucial for the classification task, are elegantly depicted in Fig. 4.8, providing a visual representation of the outcomes. Our BCI setup, known for its robust SSVEPs enabled by high-density FDM, which facilitates the deployment of a Physical Neural Network (PNN), is further utilized to demonstrate the feasibility of implementing a feedforward RC architecture.

Specifically, we apply an Extreme Learning Machine (ELM) [221] in this context. By revisiting the classification task of the multivariate breast cancer dataset, we introduce a methodological shift; we remove the reliance on genetically algorithm-optimized control parameters and adopt an encoding strategy that relies exclusively on the input data. This approach ensures that the decoding process is streamlined, focusing on the evaluation of the squared absolute value of the output Noise Power Spectral Density (NPSD) within the Second Harmonic Generation (SHG) regime. For those seeking a deeper understanding of the methodology, Eqs. (4.5) and (4.7) in Chapter 4.7offer a comprehensive explanation. The results of this endeavour are meticulously detailed and presented in Fig. 4.9.

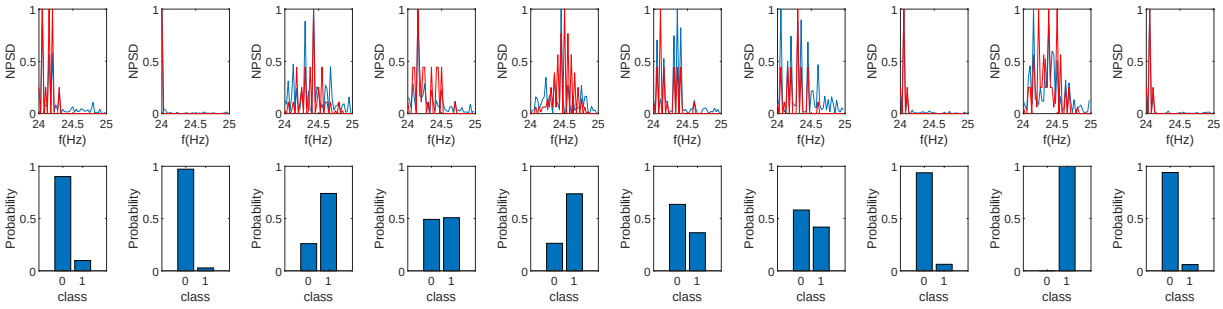

Figure 4.9: **BCI Breast Cancer Multivariate Dataset Classification: ELM Results.** Results of classification experiments of *benign* and *malignant* cancers. EEG-measured spectra in the SHG regime are reported in blue in the first row, while red lines represent synthetic data. Corresponding readout probability distributions over the two classes *benign* (labelled “0") and *malignant* (labelled “1") are shown in the second row. Only the seventh spectrum is not correctly classified. Figure taken from Ref. [4]

4.8.3 Multi-Layer SSVEP BCI: Probability Tables

Figure 4.10 presents the classification probabilities for a two-layer Physical Neural Network (PNN). In scenario (a), the same participant contributes to both layers, while in scenario (b) to (d), participant 1 is responsible for the first layer, and three additional participants constitute the second layer. The classification outcomes are notably similar across all configurations, which underscores the potential for generalizing this methodology to various individuals.

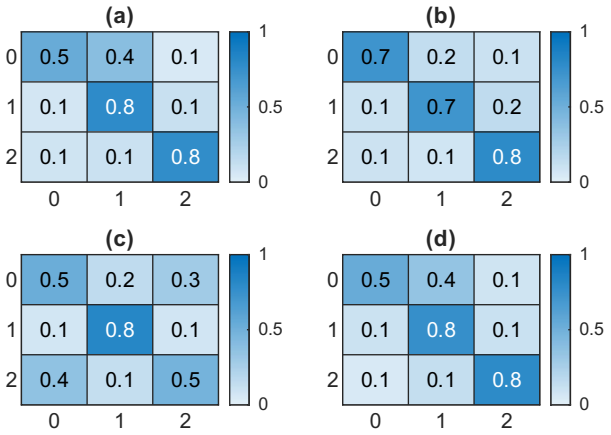

Figure 4.10: **Multi-layer PNN Probability Tables.** Classification probability distributions for different combinations of multi-layer PNN experiments on four participants for the same image classification task, i.e., classification of 3 classes Iris flower, “0", “1", and “2". In these tables, the y-axis represents the target value to be predicted, and the x-axis represents the classes of the readout probability distributions for testing experiments whose first layer is Participant number 1 and the second layer is (a) Participant number 1, (b) Participant number 2, (c) Participant number 3, (d) Participant number 4. Network training is performed employing synthetic data produced by the same phenomenological model described in Chapter 4.7. Figure taken from Ref. [4]

Chapter 5

Image Transmission with Brain Decoder

5.1 Introduction

In the chapter dedicated to brain models, we introduced various models encompassing narrowband and broadband conditions. In this chapter, we shift our focus to the broadband condition, which holds potential for applications in image transmission, particularly by leveraging the nonlinear effects of brain responses and the advancements in DNN decoding techniques.

Brain-computer interfaces (BCIs) extend human capability by enabling direct brain-machine communication and robot control, as well as providing routes for neurotechnology research focused on cognitive abilities, decision-making, memory enhancement, etc. [160–169]. Visual evoked potentials (VEPs) are widely adopted as a protocol for visual control of BCIs. A specific example of this is the steady-state visual evoked potential (SSVEP) that is observed when the light signal is periodically modulated in time, typically in the 3-30 Hz region and that can be read out either by implanted electrodes or more readily, using an electroencephalogram (EEG) [146, 170–172]. The key feature of the SSVEP signal is the formation after ~ 1 second of stimulation of a strong and relatively stable, periodic EEG signal that makes SSVEP particularly attractive, for example, for BCIs. However, the SSVEP signal also exhibits a strong nonlinearity in the form of multiple harmonics in the output power spectrum [173–175].
When using only one frequency modulation for the input light, these nonlinearities only generate second and third-harmonic signals, hence having little consequence for most applications. However, suppose multiple light-modulation frequencies are observed at the same time. In that case, these will mix and generate sum and difference frequency terms, which could in turn overlap with the input modulation frequencies (i.e., the fundamental harmonics), thus hindering the concept of multi-frequency or, using an optical telecommunications industry terminology, wavelength-division-multiplexing (WDM) in BCIs and in general for the transmission and control of information with SSVEP across broad frequency bandwidths. Indeed, the concept of WDM was

originally introduced in fibre-optic communication systems to parallelise the transmission of independent streams of data across multiple (e.g., hundreds or thousands) simultaneous (frequency) channels, and thus increase data transmission rates by orders of magnitudes.

In this work, we show that it is possible to stimulate the human visual system simultaneously with hundreds of frequencies in Chapter 4, similar to wavelength or frequency-division multiplexing (FDM) utilised in radio and optical telecommunication systems. The modulation frequencies can also extend over a broad range, that is, over more than an octave, such that their nonlinearly mixed signals overlap with the original input frequencies. After statistical analysis of experimental data, a brain model is built to study/simulate the input-output response of the brain under different light stimuli. The model can then be inverted as a DNN trained using the synthetic data created by the brain model. We demonstrate an application where each pixel from an image is encoded into a different light-modulation frequency. Then, the various light modulations are projected simultaneously and read out as an SSVEP signal that can be correctly decoded back into an image either directly from the fundamental harmonic amplitudes for narrow FDM bandwidths or using the DNN decoder for broadband FDM.

5.2 Method

5.2.1 Setup

The SSVEP signal is monitored in the frequency domain after performing a Fourier transform of the recorded signal. In most experiments to date, only single frequency modulations are used, with only a few experiments investigating the use of two simultaneous frequency modulations [188, 190, 199].

A schematic overview of our set-up is shown in Fig. 5.1. The light emitted from a single LED is modulated in time with a signal that is generated on the computer and can contain many frequencies simultaneously. Specifically, we encode black and white images into the frequency domain so that each pixel of the image corresponds to a different frequency. A black pixel has zero intensity, and a white pixel corresponds to the maximal amplitude of the respectively designated frequency modulation. All the signals are then summed together and used as a waveform that modulates the LED light intensity. The light from the LED is projected onto a white wall, which is observed by the participant wearing the EEG device. We stress that the observer is obscured from direct line-of-sight to the LED during the entire experiment. Therefore, depending on the specific image, the observer does not see a periodic modulation on the wall, as typical in most SSVEP experiments and applications, but instead observes a somewhat randomly flickering light. Moreover, the signal corresponding to the encoded image is projected on the screen

for a total time $T \geq 1/\delta f$, where δf is the separation between the uniformly spaced modulation frequencies.

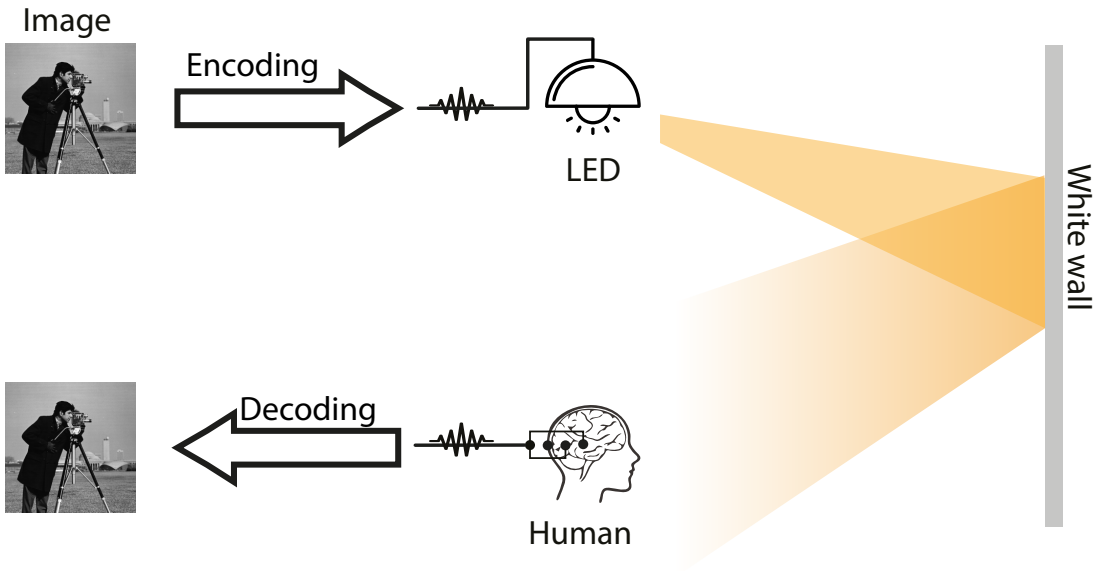

Figure 5.1: Schematic overview of the setup used for steady-state visually evoked potential frequency-division multiplexing.

5.2.2 Frequency-division multiplexing of images

The frequency encoding tags each i-th pixel value A_i of the image (composed of $N = n \times n$ pixels) with a unique frequency f_i. Therefore, the LED emission signal is:

$$\begin{aligned} S_{LED}(t) &= \sum_{i=1}^{N} A_i \cos(2\pi f_i t); \\ f_i &= f_1 + (i-1)\delta f; \\ f_{Band} &= N\delta f. \end{aligned} \tag{5.1}$$

where f_1 is the lowest value of the frequency band f_{Band}, and δf is the frequency resolution. In the experiments, the downsampled 14×14 pixel MNIST digit image "7" was frequency-division multiplexed encoded as a stimulus with $f_1 = 12$ Hz, and the corresponding SSVEP response was collected. And then the normalized power density spectrum (NPSD) were shown in Fig. 5.2 and Fig. 5.3. The NPSD is mapping minimum and maximum values of the power density spectrum to [0 1].

Fig. 5.2(a,b,c,d,e,f) and Fig. 5.3(a,b,c,d,e,f) show the NPSD of EEG under 6 different bandwidths f_{band} =1, 2, 4, 8, 12 and 16 Hz. Fig. 5.2 is for the different measuring time corresponding to

the frequency band, while Fig. 5.3 is for a fixed measuring time (196 seconds). In addition, Fig. 5.2(g) and Fig. 5.3(g) are the zoom-in of Fig. 5.2(a) and Fig. 5.3(a) respectively, from 12 Hz to 13 Hz. Fig. 5.2(h, i, j, k, l, m) and Fig. 5.3(h, i, j, k, l, m) are the images/matrixes retrieved from each i-th pixel intensity A_i, evaluated from the NPSD value at each frequency f_i. Fig. 5.2(n) and Fig. 5.3(n) are the ground truth image. In addition, the image retrieve is that these images are reconstructed/reshaped from the corresponding NPSD vectors $\begin{bmatrix} x_1 & x_2 & \dots & x_N \end{bmatrix}$ via linear indices, as shown in Eq. (5.2).

$$\begin{bmatrix} x_1 & x_2 & \dots & x_N \end{bmatrix} = \begin{bmatrix} x_1 & x_{n+1} & \dots & x_{(n-1)n} \\ x_2 & x_{n+2} & \dots & x_{(n-1)n+1} \\ \vdots & \vdots & \ddots & \vdots \\ x_n & x_{2n} & \dots & x_N \end{bmatrix} \tag{5.2}$$

, where the resolution $N = n \times n$.

The results in Fig. 5.2 show that it is possible to massively parallelize the transmission of frequency-encoded information and successfully reconstruct the information from the SSVEP signal's NPSD, despite the typical noise of EEG. However, we also note a gradual degradation of the image quality as we increase the total bandwidth used for the frequency multiplexing. We interpret this to be a result of the higher noise, also clearly visible in the spectra in Fig. 5.2c and d, which in turn is a result of the shorter total measurement times.

We also note that for example in Fig. 5.2a), the second harmonic (at 24-26 Hz) and third harmonic signals (at 36-39 Hz) are visible and are the result of the strong nonlinearity of the SSVEP. This nonlinearity can be neglected when reconstructing images from narrowband FDM signals but becomes important in broadband modulation.

5.2.3 Broadband frequency-domain multiplexing

When the frequency range is very broad, specifically more than one octave, nonlinear harmonic signals overlap with fundamental harmonic signals. An underlying assumption in the image reconstructions in Fig. 5.2 was the existence of a linear relation between the projected frequency intensities and the SSVEP frequency spectrum amplitudes. However, in the presence of SSVEP spectral peaks that contain energy contributions from all possible combinations of the light modulation frequencies, it is necessary to first determine the nonlinear mapping function.

Thus, the primary step involves determining the mapping function of the SSVEP readout under various stimuli. Given that the brain's response is inherently nonlinear and potentially chaotic, and considering the weak nature of EEG signals, the readout can become unstable and exceedingly noisy. Consequently, it is essential to initially establish the statistical properties of the

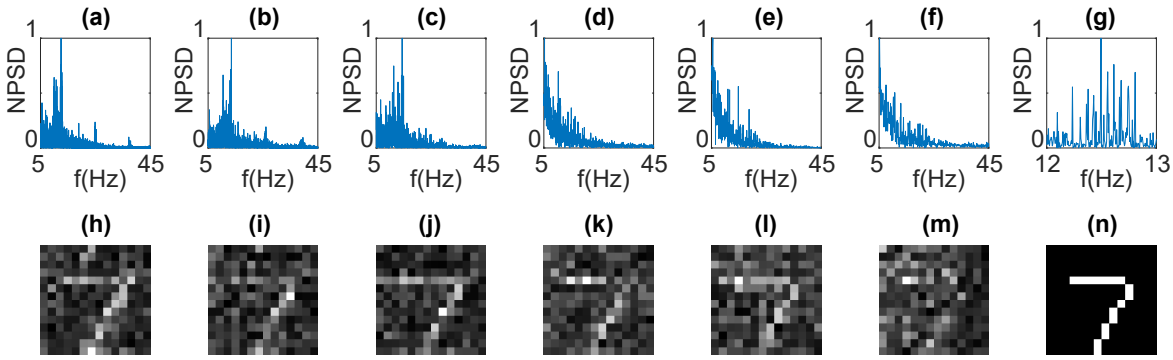

Figure 5.2: Frequency-division multiplexed encoding of an image with different frequency encoding bandwidths. a) and h) are the SSVEP power spectrum and the reconstructed image with $f_1 = 12$ Hz (and is the same for all other images), $f_{band} = 1$ Hz and measurement time $T = N/f_{band} = 196$ s, $SSIM = 0.255$; in b) and i) $f_{band} = 2$ Hz and measurement time $T = 98$ s, $SSIM = 0.218$; in c) and j) $f_{band} = 4$ Hz and measurement time $T = 32.7$ s, $SSIM = 0.278$; in d) and k) $f_{band} = 8$ Hz and measurement time $T = 16.3$ s, $SSIM = 0.238$; in e) and l) $f_{band} = 12$ Hz and measurement time $T = 16.3$ s, $SSIM = 0.224$; in f) and m) $f_{band} = 16$ Hz and measurement time $T = 16.3$ s, $SSIM = 0.153$; g) is the 1 Hz band NPSD in a) from 12 Hz to 13 Hz; n) is the ground truth image.

SSVEP spectral distribution. This statistical foundation empowers the Deep Neural Network (DNN) to accurately map the measured spectral density back to the original image.

5.2.4 Image encoder

In this section, the image is encoded into a signal that modulates the intensity of the LED. Subsequently, a DNN is designed to perform inverse mapping by decoding the brain signal back into the original image. Image encoding is achieved using FDM, as demonstrated in Eq. (5.1). The light source has limited power, denoted as P_s, which is assumed to be distributed throughout the brain response. As a result of the nonlinear effect of the brain, the harmonics of SSVEP occupy multiple frequency channels in the response signal.

To simplify the analysis, this study utilized a random binary image. The power of the received EEG signal for each positive pixel channel denoted as P_e, and its corresponding signal-to-noise

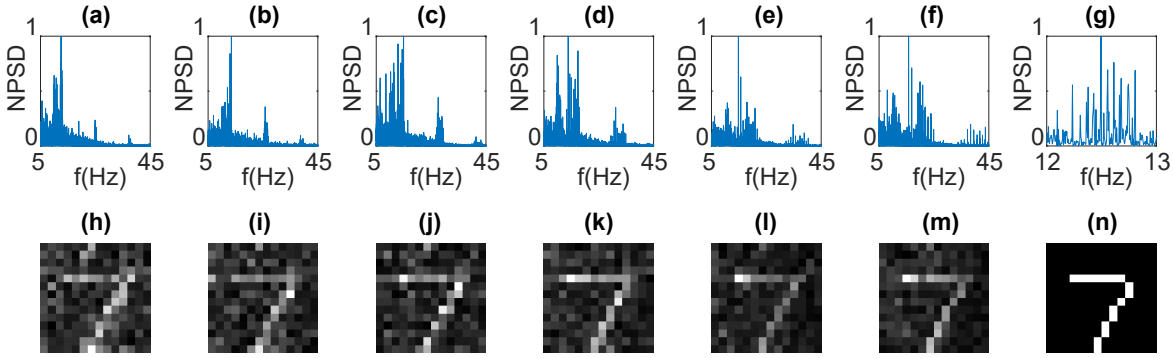

Figure 5.3: Frequency-division multiplexed encoding of an image with different frequency encoding bandwidths. a) and h) are the SSVEP power spectrum and the reconstructed image with $f_1 = 12$ Hz (and is the same for all other images), $f_{band} = 1$ Hz and measurement time $T = 196$ s, $SSIM = 0.255$; in b) and i) $f_{band} = 2$ Hz and measurement time $T = 196$ s, $SSIM = 0.270$; in c) and j) $f_{band} = 4$ Hz and measurement time $T = 196$ s, $SSIM = 0.293$; in d) and k) $f_{band} = 8$ Hz and measurement time $T = 196$ s, $SSIM = 0.332$; in e) and l) $f_{band} = 12$ Hz and measurement time $T = 196$ s, $SSIM = 0.315$; in f) and m) $f_{band} = 16$ Hz and measurement time $T = 196$ s, $SSIM = 0.368$; g) is the 1 Hz band NPSD in a) from 12 Hz to 13 Hz; n) is the ground truth image.

ratio (SNR) is presented in Eq. (5.3).

$$
\begin{aligned}
P_e &= \frac{P_s}{n_e}; P_b(t) = \frac{\tau}{t} P_b; \\
n_s &= \frac{n_1}{m}; n_e \approx n_s^2 = (\frac{n_1}{m})^2; \\
B &= \frac{aN\delta f}{m}; \\
t &= 1/\delta f > t_{min}; T = mt \geq \frac{N}{B_{max}}; \\
SNR &= \frac{P_e}{P_b(t)} = \frac{P_s t}{n_e P_b \tau} \approx \frac{P_s T}{P_b \tau n_1^2} m.
\end{aligned}
\tag{5.3}
$$

where P_s is the LED power; n_e is the number of total occupied frequency channels in the EEG signal; P_e is the average power of the occupied frequency channel; n_s is the number of total occupied frequency channels in LED signal, as F_{mix} will lead to n_s^2 frequencies when $n = 1; m = 1; N = n_s$ in Eq. (3.9), so we simply set $n_e \approx n_s^2$; n_1 represents the number of non-zero pixels; m is the number of blocks of the image divided, and $m = 1$ means to encode the whole image into one trial while $m = N$ means to encode one pixel in one trial and N trial in total; $P_b(t)$ is the related background noise power introduced; P_b is the related background noise power introduced at τ timescale; B is the bandwidth; δf is the frequency resolution; t is the acquisition time for each trial; T is the total acquisition time for an image;

When T is fixed, the range of m is shown in Eq. (5.4).

$$1 \leq m = \frac{T}{t} \leq \frac{T}{t_{min}}. \tag{5.4}$$

Eq. (5.3) shows that if we increase m, it will increase the SNR in the EEG frequency channel.

To generate a random binary image, the image indices are randomized using a random matrix M, as shown in Eq. 5.5. This process allows for the distribution of white pixels randomly, rather than having them concentrated within the central writing area.

$$\hat{I}_{N\times 1} = M_{N\times N} I_{N\times 1} \tag{5.5}$$

Here, I and $\hat{I}$ are $N \times 1$ vector reshaped from the $\sqrt{N} \times \sqrt{N}$ image; $\hat{I}$ is the randomized image N represents the total number of pixels in the image; M is a full rank matrix where each row contains 0 (representing $N-1$ pixels) and 1 (representing 1 pixel).

In the experiment, we plan to transmit one 16×16 image spending around 1 min, like $T = 64$ seconds. And then we also use $t_{min} = 4$, which offers enough time for SSVEP to establish. As a result, $m = \frac{T}{t_{min}} = 16$ for a high SNR. Then the bandwidth is $B = a\frac{N}{T} = 4a$ and the frequency mixing results are shown in Eq. 5.6.

In this study, the successful application of the decoder relies on frequency mixing. It is recommended that these bands cover the focused response frequency range of $(0, 50)$ Hz. Additionally, it is preferable for these bands to overlap at least half of their bandwidth with others and for f_0 not to be set at a low frequency since SSVEP is focused. For simplicity purposes, f_0 and a should be positive integers, where a is scale parameters.

$$\begin{cases} f \in [f_0, f_0 + 4a]; \\ f_d \in [0, 4a]; \\ f_s \in [2f_0, 2(f_0 + 4a)]; \end{cases}$$
$$\arg\min_{f_0, a} 50 - 2(f_0 + 4a), \text{ subject to: } \begin{cases} 2(f_0 + 4a) < 50; \\ 4a \geq f_0 + 2a; \\ 2f_0 \leq f_0 + 2a; \\ f_0 > 4. \end{cases} \tag{5.6}$$

Then the only solution of Eq. 5.6 is shown in Eq. 5.7.

$$f_0 = 8Hz; a = 4Hz; f \in [8, 24]Hz; \tag{5.7}$$

Then the frequency band for input stimulus is $[8,24]Hz$, and the image was divided into $m = 16$ parts. Each strip can be represented as a vector of size $\sqrt{N} \times 1$. A 16×1 strip vector was then mapped into the frequency band of $[8-24)$ Hz with a resolution of $\delta f = 1Hz$ in Eq. (5.1). Each strip corresponds to a 4-second signal that sums all the cosine waves used together. For an entire image, this results in a 64-second signal, which modulates the intensity of LEDs.

5.2.5 Image decoder

The MNIST dataset was preprocessed into 16×16 binary images, with 60,000 images for train data and 10,000 images for test data. Each image is randomized and divided into 16 strips, and each strip comes into a spectrum input of the brain model (shown in Eq. (3.29)) to get the output spectrum distribution. In this way, each image comes into 16 trial spectrum distributions, forming a spectrum matrix distribution.

In this experiment, each image tags with 50 spectrum matrices sampled from each spectrum matrix distribution. In this way, $50 \times 60000 = 3 \times 10^6$ pairs of spectrum matrix to image set were prepared for training DNN. Then, the DNN structure is shown in Fig. 5.4, where CNN_1 and CNN_2 is a single CNN layer with 32 and 64 channels respectively, aiming to extract the features of the spectrum. The fully connected layer(fC Layer) is mapping these features into the image domain(16×16). And then go into the DCNN [83] to reconstruct the image. After training,

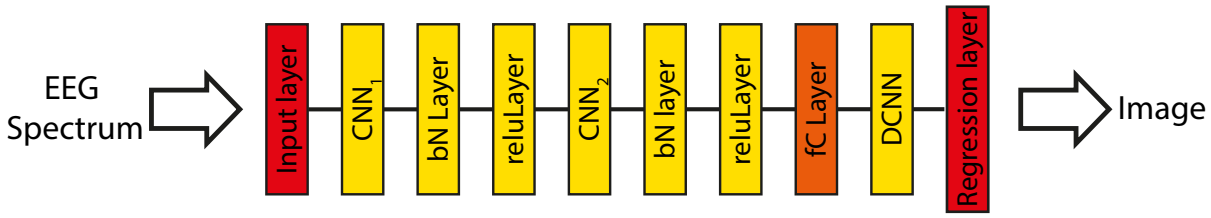

Figure 5.4: DNN structure.

10 images in the test dataset were selected to create a stimulus signal via FDM to stimulate the brain. And then 10 trials of experimental EEG data were collected, and their spectrum was fed into the DNN to reconstruct the image. The outputs of DNN are shown in Fig. 5.5. Most digital numbers can be reconstructed well with several pixels is missed. To test the repeatability of the experiment, the first image reconstruction experiment was repeated 10 times and 10 outputs are shown in Fig. 5.6(e) and the ground truth image is Fig. 5.6(a). In addition, the average and the standard deviation images were shown in Fig. 5.6(b) and c respectively. Then Fig. 5.6(d) is the output of using averaged 10 input. As shown in Fig. 5.6(e), most of the reconstructed images are clear, but the last 3 have several pixels miss or error locations.

Figure 5.5: CNN results. a) is the ground truth images; b) is the reconstructed images.

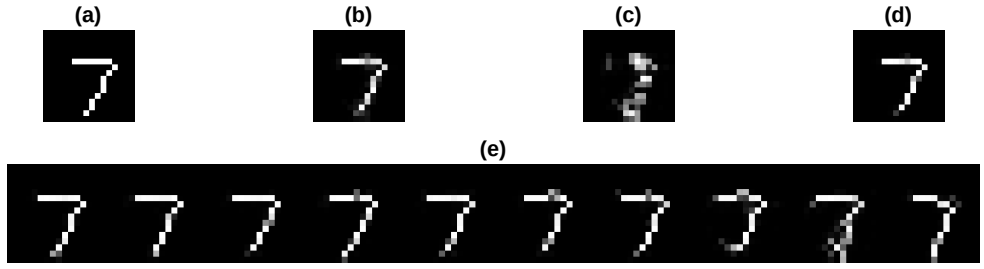

Figure 5.6: a) ground truth image; b) average of 10 output; c) std of 10 output; d) the output with averaged input; e) 10 output with 10 input.

5.3 Conclusion

We have demonstrated that it is feasible to perform simple image transmission relying on a FDM encoder and a DNN decoder. Typically, the fundamental harmonic of the SSVEP can be used to transmit the image directly, which can be approximated as a linear model. However, due to limitations in input power and the presence of internal brain noise, a prolonged measurement time is required to achieve adequate noise suppression. To enhance the signal-to-noise ratio (SNR) in SSVEP and improve transmission quality, the image was randomized and segmented into several strips before being encoded into a broadband signal. The resulting SSVEP response spectrum was then input into a trained DNN for image decoding.
Furthermore, the distribution model of brain responses can be extended for further developments, such as by employing Multi-Frequency tag identification (MFID), grey-scale image transmission, or VAE.

5.3.1 Multi-Frequency tag identification

MFID involves identifying tags using brain readouts when the brain is under frequency-tagged stimuli, particularly visual stimuli. MFID can be approached in two ways: indirectly and directly. Indirect approaches focus on higher-level visual processes, such as object, face, or scene perception, and even working memory. Direct approaches range from low-level responses, like populations of neurons reacting to contrast changes, to high-level responses, such as populations of neurons associated with shape recognition. These methods not only enhance human capabili-

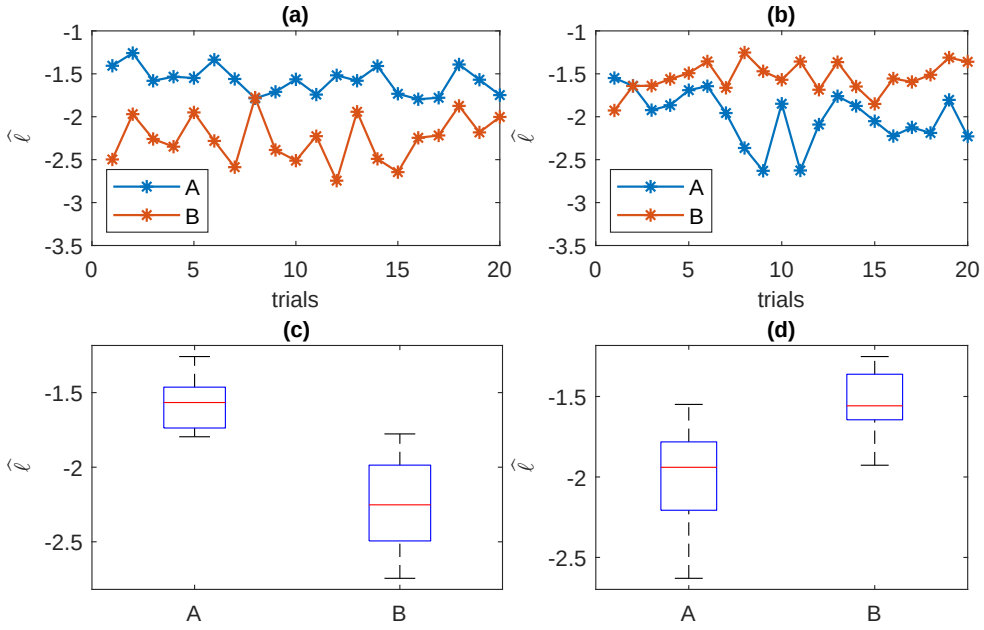

Figure 5.7: the curve and the box-plot of the object function values using 20 trials under stimulus A (12 Hz+19 Hz) and B (12 Hz+ 20 Hz) respectively. a) and c) is the curve/box-plot of object function values under stimulus A; b) and d) is the curve/box-plot of object function values under stimulus B.

ties in daily life but also expand the avenues for investigating the brain's operational workflows.

However, normally, one or two frequency and their harmonics or the basic sum/different frequency have been focused via PSD or Canonical correlation analysis (CCA). So, this study may show a new approach to using all possible mixing frequencies, the tagged stimulus of which may have three or more frequency's superpositions, it can increase the number of tags using several frequencies' superpositions. For example, an SSVEP-BCI keyboard, realized by a 60 Hz refresh rate monitor, can increase the number of tags, instead of using a single flashing frequency, like 6 Hz, 12 Hz, and 20 Hz. So, two methods can be applied, one is based on deep learning, and the other is based on conditional probability (Maximum Likelihood Estimation or Bayesian Estimation).

Deep learning approach, like our approach, but for classification. So, we only need to convert the Regression Network into the Classification Network by Replacing the Final Layers. So, after training, if we feed the EEG spectrum into the DNN, the classification results tell which tag it is.

Conditional probability approach, like Maximum Likelihood Estimation(MLE). The goal is maxing the objective function $\widehat{\ell}(\lambda; x)$, a function of λ_i, as shown in Eq. (5.8) $\mathrm{f}(x_i \mid \lambda_i)$ is the probability density function(pdf) from the brain model, x_i is the spectrum power at frequency f_i. Moreover, the tag is known, and all possible Λ can be obtained. For example, if there are 10

different tags and each tag is a frequency superposition, it means 10 kinds of λ are in the Λ set.

$$\begin{aligned} \widehat{\ell}(\lambda; x) &= \frac{1}{n}\sum_{i=1}^{n} \ln \mathrm{f}(x_i \mid \lambda_i), \\ \mathrm{f}(x_i \mid \lambda_i) &= \lambda_i e^{-\lambda_i x_i} \\ \lambda &= [\lambda_1, \lambda_2, \ldots \lambda_n]^T \in \Lambda. \end{aligned} \tag{5.8}$$

To demonstrate this method, Stimulus A (12 Hz + 19 Hz) and Stimulus B (12 Hz + 20 Hz) were assigned to two different keys. When the subject focuses on Stimulus A, the curves and the box-plot of the objective function's values $\widehat{\ell}$ for 20 trials are depicted in Figure 5.7a and c, respectively. Figures 5.7b and d illustrate the same metrics when the subject is focusing on Stimulus B. Over 95% of the trials can be accurately classified. However, when designing the frequency tags, it is essential to verify the mixing frequencies. If the list of mixing frequencies, calculated using Eq. (3.9), is too similar for two frequency tags, it may confound the objective function in Eq. (5.8). This consideration extends the applicability of frequency tag technology.

5.3.2 Greyscale Image Transmission

Greyscale image transmission can be effectively achieved using the bit plane strategy. This method involves dividing an 8-bit greyscale image into eight constituent binary images, as illustrated in Figure 5.8a. Each bit plane represents a binary image derived from one of the eight bits per pixel, resulting in a total of eight distinct bit planes.

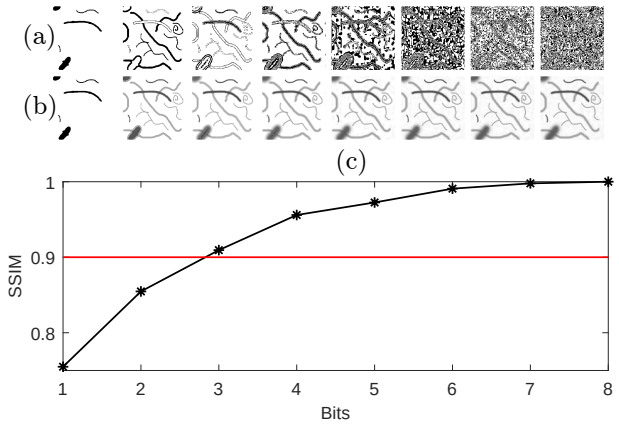

Figure 5.8: Bit plane analysis: (a) Binary images extracted from different bit planes; (b) Eight images, each representing a different bit plane, ranging from the least significant bit to the most significant bit; (c) Structural Similarity Index (SSIM) between the eight images in (b) and the reference image.

Figure 5.8b) displays the eight binary images, each corresponding to a different bit plane, while Figure 5.8c) presents the Structural Similarity Index (SSIM) between these eight images and a reference image. It is observed that even when only three bits are utilized, the image can

be satisfactorily reconstructed with an $SSIM > 0.9$. Furthermore, Vector Quantization offers additional options for greyscale images by employing efficient lossy compression techniques, thereby expanding the range of possibilities for image transmission.

5.3.3 Normal distribution for Variational Autoencoder

After training a Variational Autoencoder (VAE), it enables the generation of novel images by sampling from a normal distribution, producing content not present in the original training dataset. In this thesis, a DNN-based brain decoder is employed to map distributional samples into target images for transmission. These two functionalities—image generation and image reconstruction—offer an intriguing opportunity for integration. The generated images could potentially serve as representations of brain states, such as indicating levels of brain fatigue.

Specifically, the brain's EEG spectrum, when interpreted as a probabilistic distribution, can be mapped to a normal distribution. This mapping enables the seamless integration of EEG-derived distributions with a VAE decoder to produce novel images that were not part of the original training set.

In practice, new images can be generated by passing randomly sampled encodings, representing brain readouts, through the VAE decoder. This approach not only extends the utility of brain decoding techniques but also underscores the potential for synthesizing novel images directly from neural activity. Such advancements open exciting new possibilities for creativity and exploration in neural signal processing, showcasing the potential for bridging brain decoding with generative modelling techniques.

$$
\begin{aligned}
X &\sim \mathrm{Exp}(\lambda) \\
Y = F(X;\lambda) = 1 - e^{-\lambda X} &\sim \mathrm{U}(0,1) \\
or \quad Y = \frac{X_i}{X_i + X_j} &\sim \mathrm{U}(0,1) \\
\theta &= 2\pi Y_1 \\
\rho &= \sqrt{-2\log(Y_2)} \\
Z_1 = \rho \times \cos(\theta) &\sim \mathrm{N}(0,1) \\
Z_2 = \rho \times \sin(\theta) &\sim \mathrm{N}(0,1)
\end{aligned}
\tag{5.9}
$$

As detailed in Eq. (5.9), the process involves two main steps: First, the cumulative distribution function (CDF) is used to transform $X \sim \mathrm{Exp}(\lambda)$ into $Y \sim U(0,1)$; second, the Box-Muller-Wiener algorithm is applied to convert $Y \sim U(0,1)$ into $Z \sim N(0,1)$. The results generated by the VAE decoder utilizing the EEG spectrum are depicted in Figure 5.9. It is observed that the

distribution-normalized spectrum yields superior results compared to using the raw spectrum. This approach enables the brain to produce normally distributed random numbers, which can be utilized within the VAE's decoder or potentially extended to other applications.

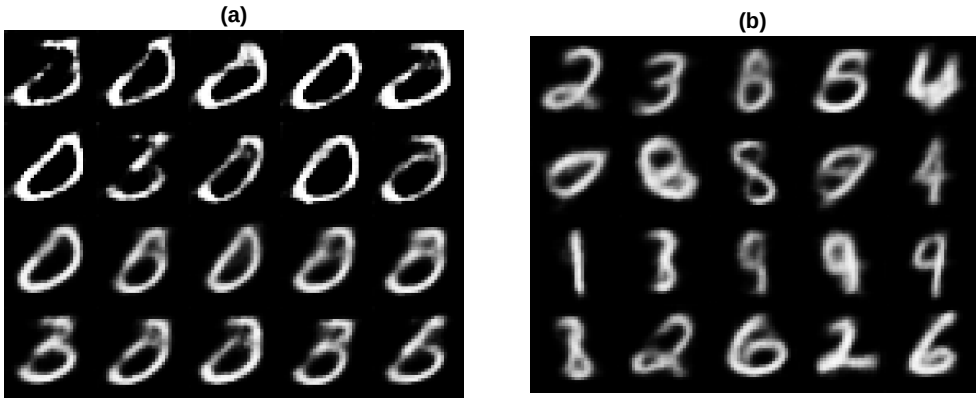

Figure 5.9: The results generated by the VAE decoder. a) is the output of the VAE decoder using the original spectrum; b) is the generated images of the VAE decoder using the distribution normalized spectrum.

5.3.4 Frequency encoded computational Imaging

Frequency encoding can be extended to the realm of computational imaging when patterns are Time-Frequency encoded. According to the brain model, the brain can be considered a unique detector that exhibits nonlinear characteristics and processes stationary signals in the frequency domain. This concept allows us to expand computational imaging into the time-frequency domain, with a particular focus on ghost imaging [2].

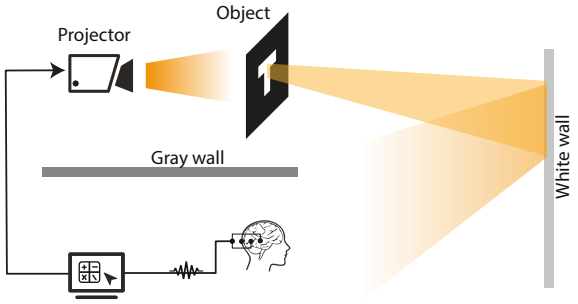

Figure 5.10: Frequency encoded Computational imaging integrated with the brain.

Chapter 6

Conclusions

This thesis has explored and demonstrated computational imaging with the human brain across several facets, including ghost imaging, physical neuromorphic systems, and broadband image transmission, with the latter two grounded in a phenomenological brain model. In doing so, it has contributed to advancing our understanding of SSVEP phenomena, modelling human brain responses, and developing novel applications in neuromorphic and communication systems.

In Chapter 2, the human brain was employed as a nonlinear detector in the context of computational imaging tasks. On one hand, this research has demonstrated the brain's ability to function as a biological detector within computational ghost imaging protocol. However, general ghost imaging protocols are limited by slow imaging speeds and significant noise from brain signals. To address these challenges, this work introduced the carving ghost imaging method to enhance imaging speed and employed a DNN-based ghost imaging method to map SSVEP powers into images, effectively mitigating noise. The primary contributions include boosting ghost imaging performance, modelling EEG's power characteristics, and developing anti-noise algorithms. These advances significantly enrich the field of ghost imaging and provide a deeper characterization of brain-generated noise. On the other hand, the human brain's nonlinear detection capabilities were shown to reflect cognitive information processing states. A novel method was developed to explore the conscious and unconscious states of the human brain using an SSVEP-based detector. This approach enables a deeper understanding of the interaction between different levels of cognitive processing. Key contributions include investigating human brain information processing and differentiating between conscious and unconscious states, which have implications for diagnosing and understanding brain consciousness.

Chapter 3 explored the complexity of SSVEP phenomena, presenting a phenomenological model for SSVEP under both narrowband and broadband scenarios. Developing a mathematical description of SSVEP responses is essential for better understanding and practical applications. Under the narrowband scenario, a mathematical model was derived using approximations suited to

narrowband conditions. This simplified model successfully predicts response behaviours within the band. Under the broadband scenario, a statistical model was developed to describe SSVEP responses under complex multi-frequency stimuli. The model incorporates nonlinear frequency mixing terms and provides predictive capabilities for statistical parameters across collected data. The contributions of this chapter include modelling the nonlinear behaviour of SSVEP, predicting response trends, and advancing BCI development, thereby enriching both theoretical understanding and practical applications of SSVEP.

In Chapter 4, the application of the narrowband brain model was extended to create physical neuromorphic systems. This involved using the human brain to implement a neural network structure, demonstrating its potential for performing AI tasks. By employing high-density Frequency Division Multiplexing (FDM), this research encoded data into light stimuli, stimulating the brain to elicit SSVEPs. The intermodulation response under high-density FDM was modelled and applied to predict SSVEP readouts, involving hundreds of frequencies. These findings demonstrated the brain's capacity for parallel information encoding and neural network implementation. Moreover, the neuromorphic system was shown to be influenced by brain states, such as 'focus' and 'disrupt,' which significantly affected output classification performance. The contributions of this chapter include Development of high-density FDM techniques for neuromorphic systems. Demonstration of multi-brain scalability for neural network layers. Investigation of brain state effects on neuromorphic performance. These advancements open pathways for assistive technologies, cognitive enhancement tools, and diagnostic methods for attention focus and fatigue.

Chapter 5 explored the application of broadband brain models to enable image transmission through the human brain as a communication channel. This study demonstrated the feasibility of broadband FDM, stimulating the human visual system with a wide range of frequencies. A DNN trained on synthetic data was employed to decode images encoded into light-modulation frequencies. This broadband approach enabled accurate image reconstruction and surpassed the bandwidth limitations of traditional narrowband SSVEP BCIs. Key contributions include Demonstration of broadband FDM for neural signal transmission. Development of DNN-based encoding and decoding techniques. Advancement of real-time image transmission through neural interfaces. These findings pave the way for advanced cognitive enhancements and sophisticated human-machine interaction technologies.

The findings of this thesis contribute new insights into SSVEP-based BCIs, computational imaging, and brain modelling. The integration of computational imaging with BCIs introduces novel methods for studying cognitive processes and implementing neuromorphic systems. These contributions are expected to inform future advancements in neural interface technologies, assistive devices, and cognitive augmentation.

In conclusion, this thesis has demonstrated significant advancements in SSVEP-based computational imaging, neuromorphic systems, and broadband communication. Bridging theoretical modelling with experimental validation lays a solid foundation for future research and innovation in neural interface technologies.

While there are challenges and limitations to address, the findings presented in this thesis emphasize the unique potential of using the BCI not only as a communication channel but also as a platform for exploring cognitive neuroscience and neural augmentation. We hope that this work inspires further exploration and contributes to the continued advancement of brain-computer interface systems, computational imaging, and the broader understanding of brain functionality.

Chapter 7

Limitations and Future Work

While this thesis presents significant advancements in the field of computational imaging and brain-computer interfaces (BCI), several limitations must be acknowledged to contextualize the findings and guide future research.

7.1 Temporal and Intensity Variations

Figures 2.7, 2.8, 2.10, and 2.11 demonstrate the relationship between screen intensity and response over an extended period. However, the sequential nature of the measurements introduces potential confounding factors, such as temporal variations (e.g., subject fatigue, photoreceptor bleaching) intertwined with intensity variations. These could explain the unusual negative gradients observed in the transfer function.

To address this limitation in future experiments:

- **Randomized measurement order**: Intensity measurements should be randomized in time to eliminate potential biases from sequential measurement order.
- **Reverse-order measurement**: Performing the measurements in reverse order would help identify and isolate temporal effects.
- **Dynamic control conditions**: Implementing frequent breaks and varying the order of stimuli would help account for adaptation and fatigue effects.

These refinements would enhance the reliability of the measurements and clarify the contribution of temporal variations to the observed results.

7.2 Conscious vs Nonconscious Protocols

The conscious/nonconscious experimental protocols, while insightful, are subject to potential confounds:

- **Photoreceptor adaptation**: Actions like looking away from the screen to type or disruptions from speaking may influence the results independently of the conscious or nonconscious states being measured.
- **Task-specific disruptions**: Conscious activity, such as typing, might introduce unaccounted disruptions or influence photoreceptor activity.

Future protocols should explicitly control for these confounds. For example, participants should maintain a consistent gaze during all tasks, and alternative input methods (e.g., counting the number of typing one key) could replace typing to minimize disruptions. If such controls are not feasible, this limitation should be explicitly acknowledged to ensure the validity of conclusions.

7.3 Potential Experimenter Bias

The expectations of the researcher could unintentionally impact the results, particularly during subjective evaluations or manual calibration steps. This potential bias should be minimized through:

- **Blinded experimental protocols**: Ensuring that the experimenter is unaware of the condition being tested during data collection and analysis.
- **Automation**: Automating stimulus presentation and data collection wherever possible to reduce human involvement and potential bias.

Implementing these steps would strengthen the methodological rigour of future studies.

7.4 Sample Size Limitations

Some of the experiments reported in this thesis involve small sample sizes (e.g., 1-3 participants), which limits the generalizability of the findings. While small sample sizes are sometimes justified for proof-of-concept studies, larger participant pools are essential for robust statistical analyses, particularly for ERP studies and other brain signal measurements.

Future work should:

- **Expand sample sizes**: Recruitment of larger, more diverse participant groups to improve the reliability and generalizability of the findings.

- **Standardize protocols**: Employ consistent protocols to facilitate comparisons across studies and populations.

7.5 Opportunities for Future Research

Addressing these limitations provides several avenues for future research:

- Investigating the impact of randomized intensity measurement on the accuracy and reliability of transfer functions.
- Designing more robust protocols for conscious/nonconscious state experiments to isolate relevant factors.
- Expanding sample sizes to validate findings and explore inter-subject variability.
- Developing fully automated and blinded experimental setups to eliminate bias.
- Modeling the human brain requires accounting for its dynamic nature, as it is a nonlinear and time-varying system.

Appendix A

Spectrum verification

Spectrum distribution and Frequency mixing verification are demonstrated here. To verify the assumption (each frequency's power is independent exponential distribution), as well as to verify the Eq. (3.9), different kinds of stimuli were tested, and there are seven experiment results in total shown: Fig. A.2, Fig. A.3, Fig. A.4, Fig. A.5, Fig. A.6, Fig. A.7, Fig. A.8, Fig. A.9, and Fig. A.10.

Throughout these experiments results, all distributions fit the exponential distribution well, and the sum and difference frequencies can also be found as peaks. The average slope (Mean vs Std) is shown in Eq. (A.1).

$$slope = \frac{Std}{Mean} = 0.98 \pm 0.16. \tag{A.1}$$

Throughout these experiments, almost all the mixing frequencies are picked up correctly and the result of λ is shown in Eq. (A.2).

$$\begin{aligned} \beta_N &= \frac{1}{\lambda_N} = 1.26 \pm 0.15 \\ \beta_P &= \frac{1}{\lambda_P} = 4.14 \pm 0.97 \\ \frac{\beta_P}{\beta_N} &\approx 3.29. \end{aligned} \tag{A.2}$$

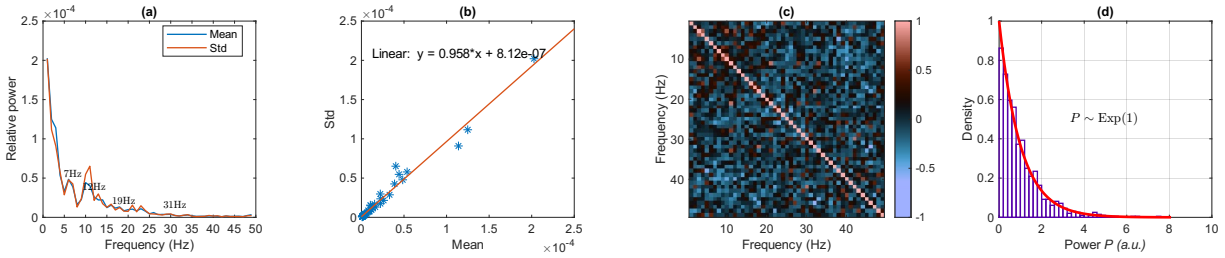

Figure A.1: EEG spectrum analysis under baseline state. a) Mean and standard deviation of the spectrum under the baseline state; b) Fitting between the mean and standard deviation of the spectrum under the baseline state; c) Mean and standard deviation of the spectrum under the stimulus state; d) Fitting between the mean and standard deviation of the spectrum under the stimulus state.

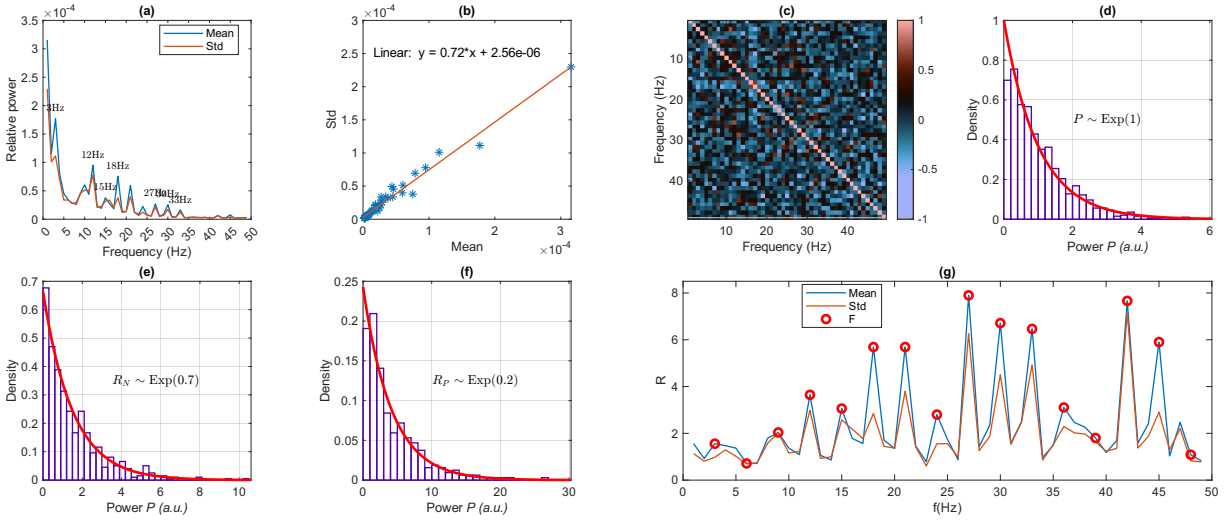

Figure A.2: EEG spectrum analysis under stimulus state (12 Hz + 15 Hz + 18 Hz). a) Mean and standard deviation of the spectrum; b) Fitting between the mean and standard deviation of the spectrum; c) Mean and standard deviation of the spectrum; d) Fitting between the mean and standard deviation of the spectrum; e) EEG spectrum correlation coefficients; f) Normalized EEG spectrum histogram; g) EEG spectrum ratio histogram at non-peak parts; h) EEG spectrum ratio histogram at peak parts; i) EEG spectrum mean and standard deviation of the ratio for each frequency, with the ratio comparing the stimulus state to the baseline state.

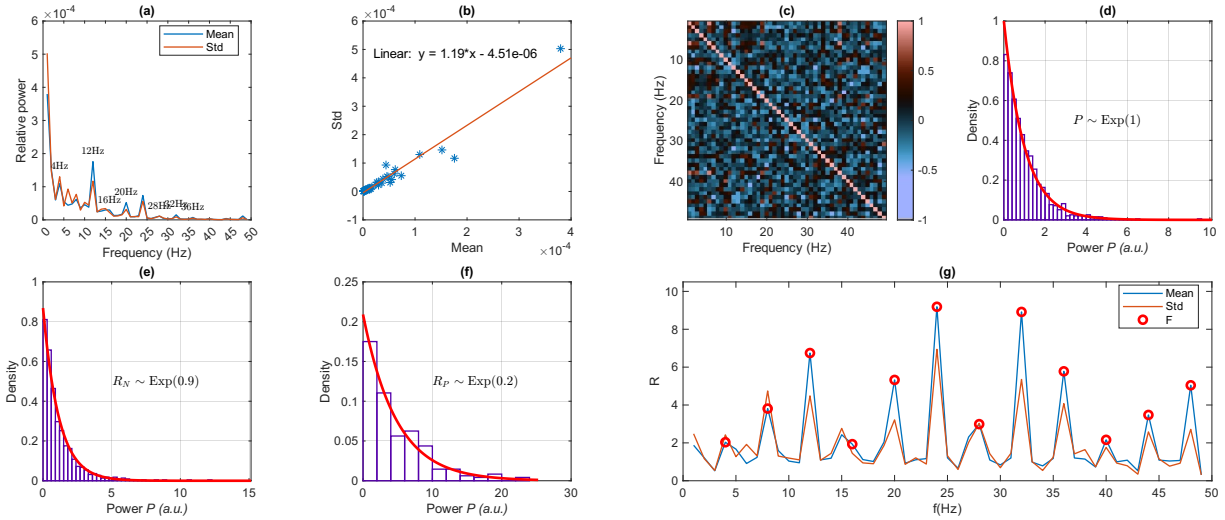

Figure A.3: EEG spectrum analysis under stimulus state (12 Hz + 16 Hz + 20 Hz). a) Mean and standard deviation of the spectrum; b) Fitting between the mean and standard deviation of the spectrum; c) Mean and standard deviation of the spectrum; d) Fitting between the mean and standard deviation of the spectrum; e) EEG spectrum correlation coefficients; f) Normalized EEG spectrum histogram; g) EEG spectrum ratio histogram at non-peak parts; h) EEG spectrum ratio histogram at peak parts; i) EEG spectrum mean and standard deviation of the ratio for each frequency, with the ratio comparing the stimulus state to the baseline state.

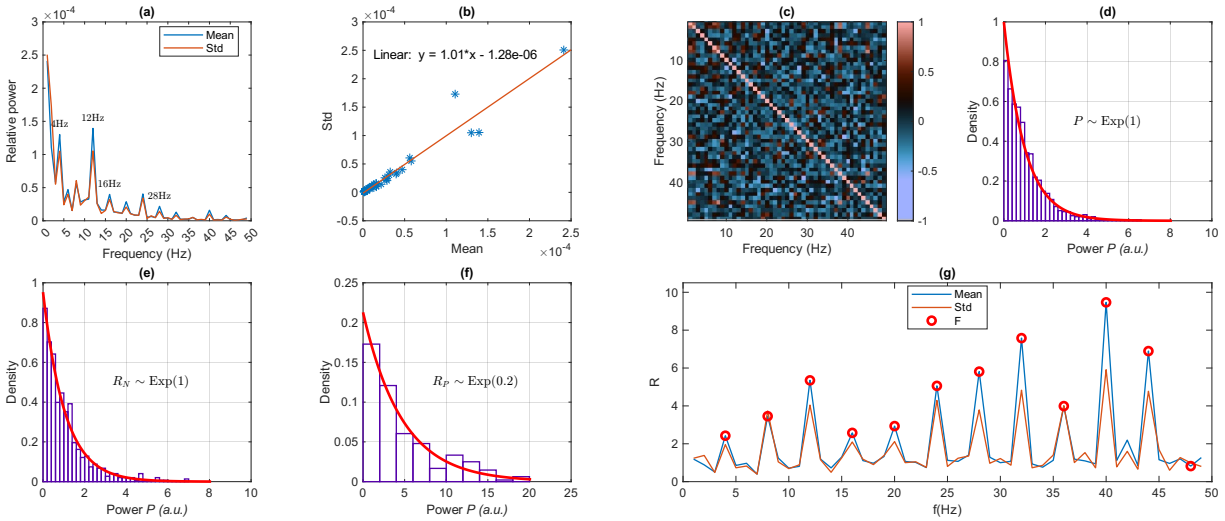

Figure A.4: EEG spectrum analysis under stimulus state (12 Hz + 16 Hz). a) Mean and standard deviation of the spectrum; b) Fitting between the mean and standard deviation of the spectrum; c) Mean and standard deviation of the spectrum; d) Fitting between the mean and standard deviation of the spectrum; e) EEG spectrum correlation coefficients; f) Normalized EEG spectrum histogram; g) EEG spectrum ratio histogram at non-peak parts; h) EEG spectrum ratio histogram at peak parts; i) EEG spectrum mean and standard deviation of the ratio for each frequency, with the ratio comparing the stimulus state to the baseline state.

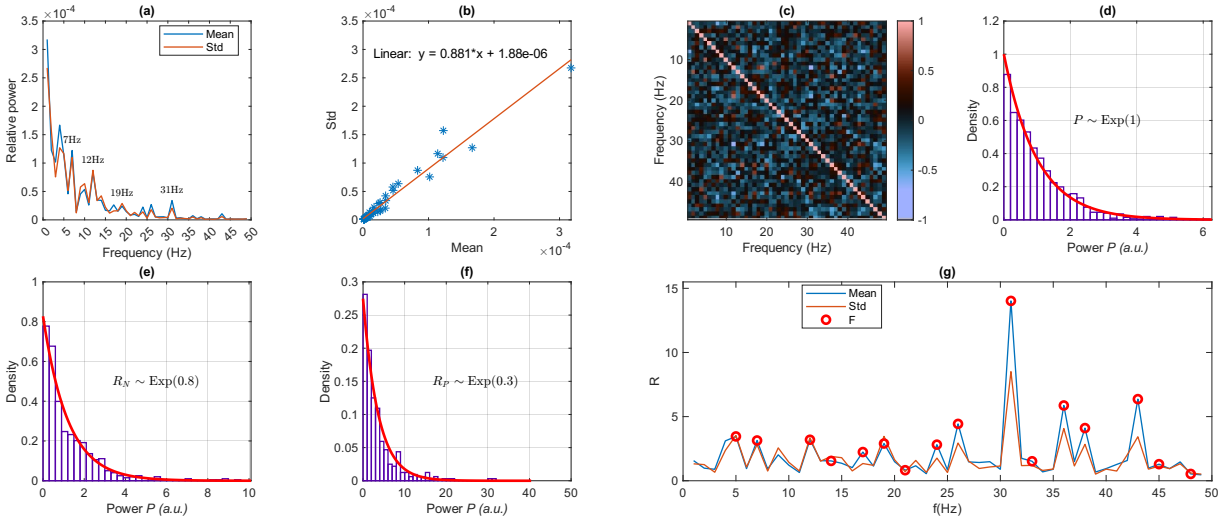

Figure A.5: EEG spectrum analysis under stimulus state (12 Hz + 19 Hz). a) Mean and standard deviation of the spectrum; b) Fitting between the mean and standard deviation of the spectrum; c) Mean and standard deviation of the spectrum; d) Fitting between the mean and standard deviation of the spectrum; e) EEG spectrum correlation coefficients; f) Normalized EEG spectrum histogram; g) EEG spectrum ratio histogram at non-peak parts; h) EEG spectrum ratio histogram at peak parts; i) EEG spectrum mean and standard deviation of the ratio for each frequency, with the ratio comparing the stimulus state to the baseline state.

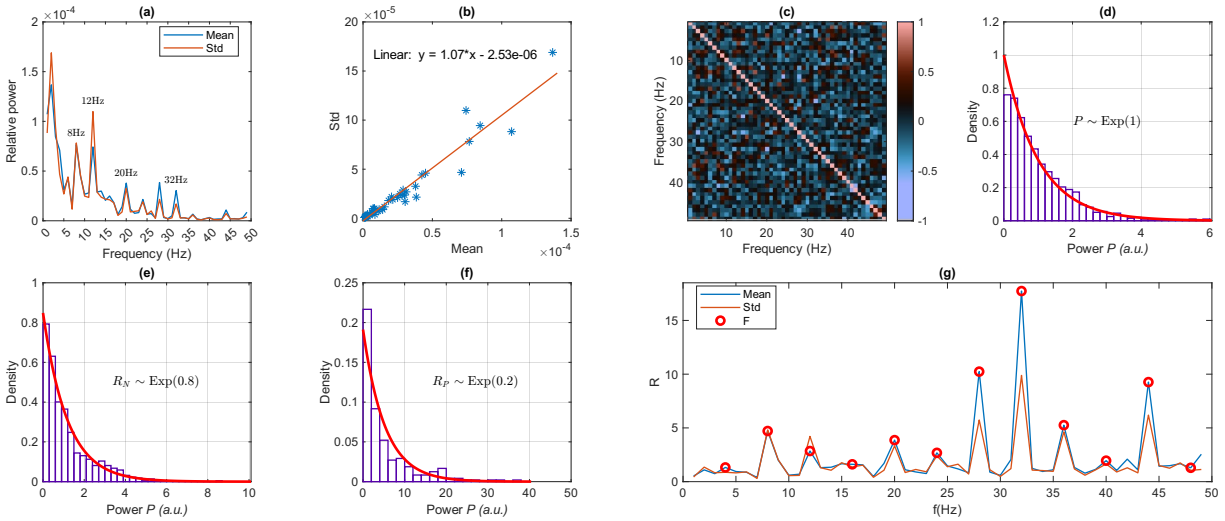

Figure A.6: EEG spectrum analysis under stimulus state (12 Hz + 20 Hz). a) Mean and standard deviation of the spectrum; b) Fitting between the mean and standard deviation of the spectrum; c) Mean and standard deviation of the spectrum; d) Fitting between the mean and standard deviation of the spectrum; e) EEG spectrum correlation coefficients; f) Normalized EEG spectrum histogram; g) EEG spectrum ratio histogram at non-peak parts; h) EEG spectrum ratio histogram at peak parts; i) EEG spectrum mean and standard deviation of the ratio for each frequency, with the ratio comparing the stimulus state to the baseline state.

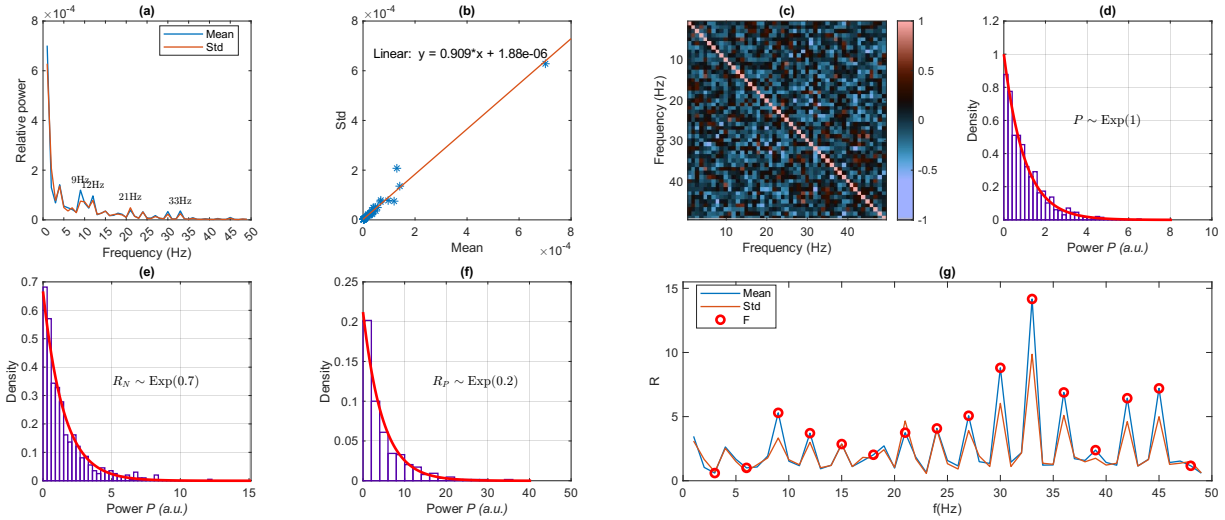

Figure A.7: EEG spectrum analysis under stimulus state (12 Hz + 21 Hz). a) Mean and standard deviation of the spectrum; b) Fitting between the mean and standard deviation of the spectrum; c) Mean and standard deviation of the spectrum; d) Fitting between the mean and standard deviation of the spectrum; e) EEG spectrum correlation coefficients; f) Normalized EEG spectrum histogram; g) EEG spectrum ratio histogram at non-peak parts; h) EEG spectrum ratio histogram at peak parts; i) EEG spectrum mean and standard deviation of the ratio for each frequency, with the ratio comparing the stimulus state to the baseline state.

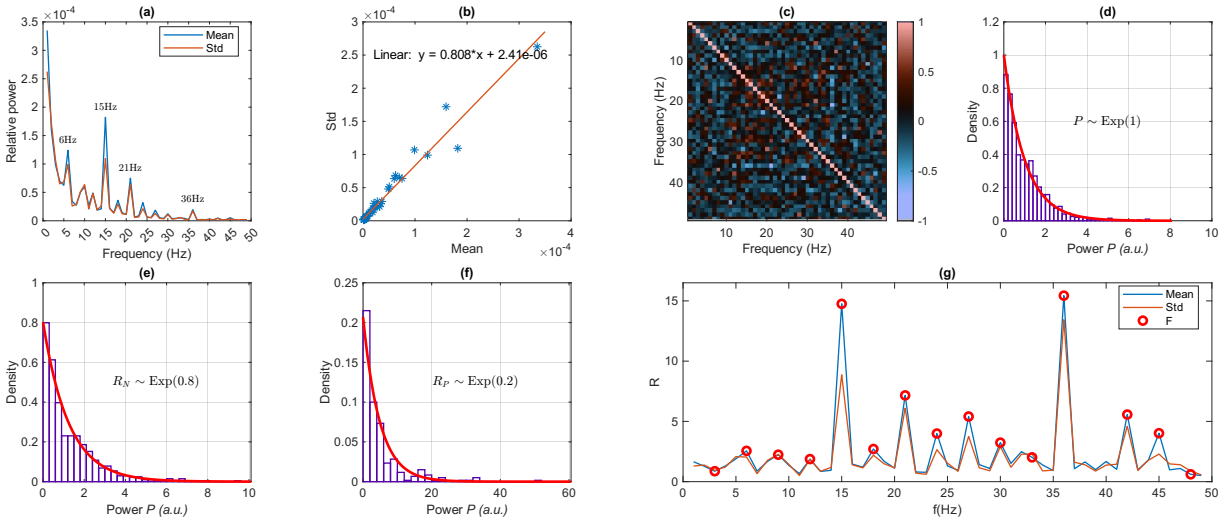

Figure A.8: EEG spectrum analysis under stimulus state (15 Hz + 21 Hz). a) Mean and standard deviation of the spectrum; b) Fitting between the mean and standard deviation of the spectrum; c) Mean and standard deviation of the spectrum; d) Fitting between the mean and standard deviation of the spectrum; e) EEG spectrum correlation coefficients; f) Normalized EEG spectrum histogram; g) EEG spectrum ratio histogram at non-peak parts; h) EEG spectrum ratio histogram at peak parts; i) EEG spectrum mean and standard deviation of the ratio for each frequency, with the ratio comparing the stimulus state to the baseline state.

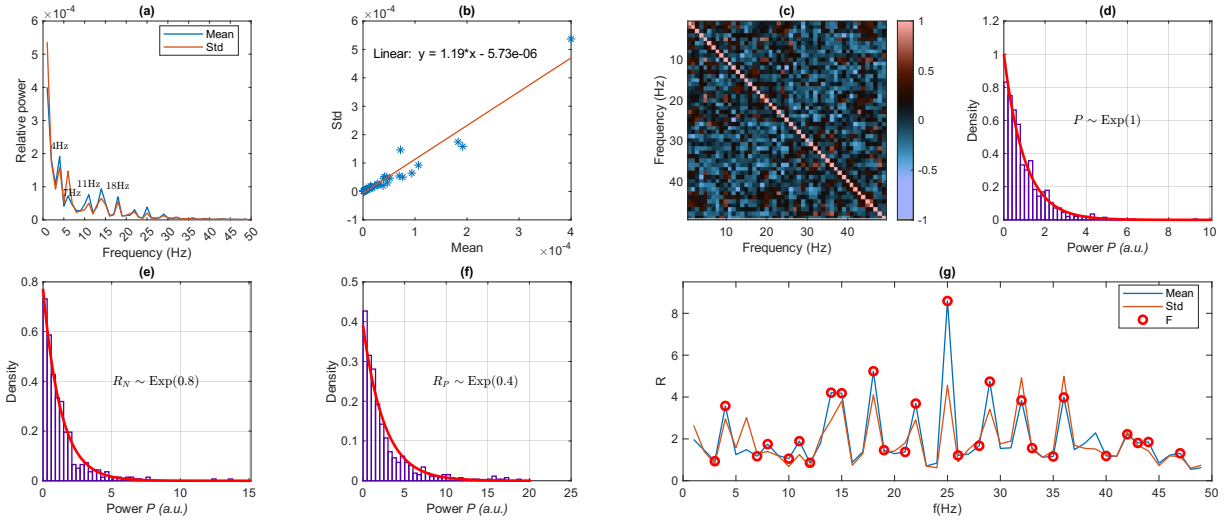

Figure A.9: EEG spectrum analysis under stimulus state (7 Hz + 11 Hz). a) Mean and standard deviation of the spectrum; b) Fitting between the mean and standard deviation of the spectrum; c) Mean and standard deviation of the spectrum; d) Fitting between the mean and standard deviation of the spectrum; e) EEG spectrum correlation coefficients; f) Normalized EEG spectrum histogram; g) EEG spectrum ratio histogram at non-peak parts; h) EEG spectrum ratio histogram at peak parts; i) EEG spectrum mean and standard deviation of the ratio for each frequency, with the ratio comparing the stimulus state to the baseline state.

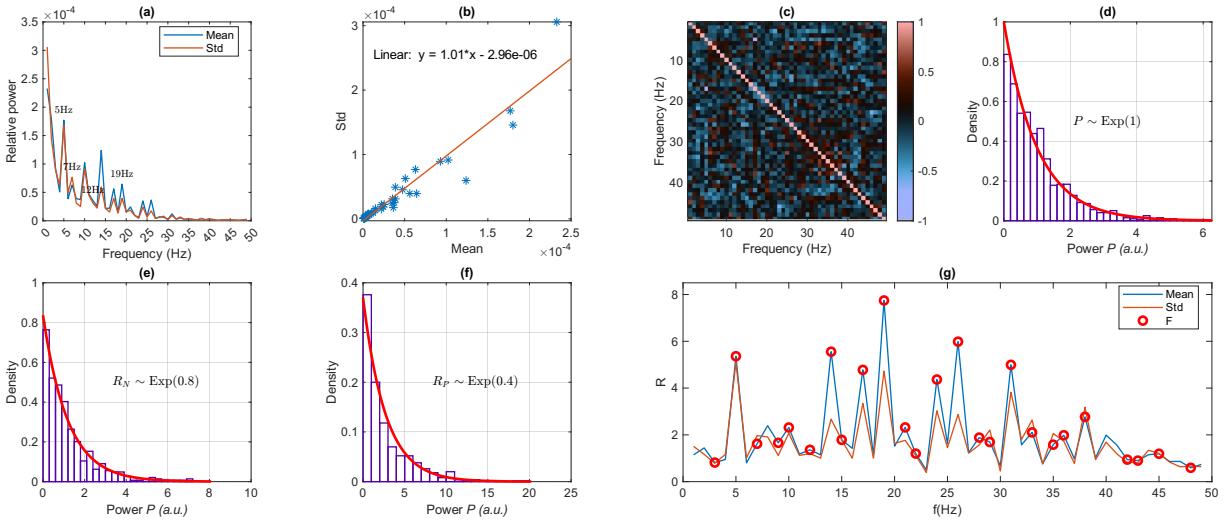

Figure A.10: EEG spectrum analysis under stimulus state (7 Hz + 12 Hz). a) Mean and standard deviation of the spectrum; b) Fitting between the mean and standard deviation of the spectrum; c) Mean and standard deviation of the spectrum; d) Fitting between the mean and standard deviation of the spectrum; e) EEG spectrum correlation coefficients; f) Normalized EEG spectrum histogram; g) EEG spectrum ratio histogram at non-peak parts; h) EEG spectrum ratio histogram at peak parts; i) EEG spectrum mean and standard deviation of the ratio for each frequency, with the ratio comparing the stimulus state to the baseline state.

Appendix B

Ethical approval

University of Glasgow | College of Science & Engineering

Institute of Neuroscience and Psychology
School of Psychology

Prof Lawrence W. Barsalou

62 Hillhead Street
Glasgow G12 8QB
United Kingdom

Phone: +44 (0) 141 330 3035
Email: lawrence.barsalou@glasgow.ac.uk

24 Aug 2021

Ethical approval for:

Application Number: 300210003

Project Title: Ghost imaging protocol with the human visual system

Lead Researcher: Professor Daniele Faccio

This is to confirm that the College of Science and Engineering Ethics Committee has reviewed the above application and **approved** it. Please download the approval letter from the Research Ethics System for your records.

Please note that if your proposal involves face-to-face research, approval to carry out this research is only granted when one of the following two conditions has been met:

(a) You have a performed a risk assessment of your research protocol in your research facility, had it approved by your Head of School / Director of Institute, and received permission to proceed with this specific research project, or

(b) The University has generally lifted its social distancing restrictions on face-to-face interaction, including research.

In either case, your approval for this project lasts for 6 months from the date you are allowed to proceed with data collection.

If your research collects data in a format that **does not require social contact** (e.g., online research), you may begin data collection now.

Also please download and read the Collated Comments associated your application. This document contains all the reviews of your application and can be found below your approval letter on the Research Ethics System. These reviews may contain useful suggestions and observations about your research protocol for strengthening it. Good luck with your research.

Sincerely,

Lawrence W. Barsalou

Ethics Officer
College of Science and Engineering
University of Glasgow

Bibliography

[1] G. M. Gibson, S. D. Johnson, and M. J. Padgett, "Single-pixel imaging 12 years on: a review," *Optics express*, vol. 28, no. 19, pp. 28190–28208, 2020.

[2] G. Wang and D. Faccio, "Computational Ghost Imaging with the Human Brain," *Intelligent Computing*, vol. 2, p. 0014, Jan. 2023.

[3] "EEG Click." http://www.mikroe.com/eeg-click.

[4] G. Wang, G. Marcucci, B. Peters, M. C. Braidotti, L. Muckli, and D. Faccio, "Human-centred physical neuromorphics with visual brain-computer interfaces," *Nature Communication*, 2024.

[5] L. Wang and K.-J. Yoon, "Deep learning for hdr imaging: State-of-the-art and future trends," *IEEE transactions on pattern analysis and machine intelligence*, vol. 44, no. 12, pp. 8874–8895, 2021.

[6] M. Brown and D. G. Lowe, "Automatic panoramic image stitching using invariant features," *International journal of computer vision*, vol. 74, pp. 59–73, 2007.

[7] D. B. Plewes and W. Kucharczyk, "Physics of mri: a primer," *Journal of magnetic resonance imaging*, vol. 35, no. 5, pp. 1038–1054, 2012.

[8] P. J. Withers, C. Bouman, S. Carmignato, V. Cnudde, D. Grimaldi, C. K. Hagen, E. Maire, M. Manley, A. Du Plessis, and S. R. Stock, "X-ray computed tomography," *Nature Reviews Methods Primers*, vol. 1, no. 1, p. 18, 2021.

[9] M. Long, Y. Soubo, S. Cong, N. Weiping, and L. Tong, "Learning deconvolutions for astronomical images," *Monthly Notices of the Royal Astronomical Society*, vol. 504, no. 1, pp. 1077–1083, 2021.

[10] H. Luo, Z. Qi, Y. Yu, and S. Liao, "Research on theoretical method of computational imaging astrometry," in *Optics Frontier Online 2020: Optics Imaging and Display*, vol. 11571, pp. 235–242, SPIE, 2020.

[11] R. Lukac, *Computational photography: methods and applications*. CRC press, 2017.

[12] G. Wu, B. Masia, A. Jarabo, Y. Zhang, L. Wang, Q. Dai, T. Chai, and Y. Liu, "Light field image processing: An overview," *IEEE Journal of Selected Topics in Signal Processing*, vol. 11, no. 7, pp. 926–954, 2017.

[13] V. Katkovnik and J. Astola, "Compressive sensing computational ghost imaging," *Journal of the Optical Society of America A*, vol. 29, p. 1556, Aug. 2012.

[14] Y. Shechtman, Y. C. Eldar, O. Cohen, H. N. Chapman, J. Miao, and M. Segev, "Phase retrieval with application to optical imaging: a contemporary overview," *IEEE signal processing magazine*, vol. 32, no. 3, pp. 87–109, 2015.

[15] J. H. Shapiro, "Ghost imaging: A theme with variations," in *Imaging and Applied Optics 2015*, COSI, p. CT4F.4, OSA, 2015. https://doi.org/10.1364/COSI.2015.CT4F.4.

[16] M. J. Padgett and R. W. Boyd, "An introduction to ghost imaging: quantum and classical," *Philosophical Transactions of the Royal Society A: Mathematical, Physical and Engineering Sciences*, vol. 375, p. 20160233, June 2017. https://doi.org/10.1098/rsta.2016.0233.

[17] R. S. Bennink, S. J. Bentley, and R. W. Boyd, ""two-photon" coincidence imaging with a classical source," *Physical Review Letters*, vol. 89, Aug. 2002. https://doi.org/10.1103/PHYSREVLETT.89.113601.

[18] L. A. Lugiato, ""ghost imaging": Fundamental and applicative aspects," *Istituto Lombardo - Accademia di Scienze e Lettere - Rendiconti di Scienze*, July 2015. https://doi.org/10.4081/SCIE.2013.169.

[19] P.-A. Moreau, E. Toninelli, T. Gregory, and M. J. Padgett, "Ghost Imaging Using Optical Correlations," *Laser & Photonics Reviews*, vol. 12, p. 1700143, Jan. 2018.

[20] S. Denis, P.-A. Moreau, F. Devaux, and E. Lantz, "Temporal ghost imaging with twin photons," *Journal of Optics*, vol. 19, p. 034002, Mar. 2017.

[21] D. Faccio, "Temporal ghost imaging," *Nature Photonics*, vol. 10, pp. 150–152, Mar. 2016.

[22] W. Gong and S. Han, "High-resolution far-field ghost imaging via sparsity constraint," *Scientific Reports*, vol. 5, p. 9280, Mar. 2015.

[23] S. M. Mahdi Khamoushi, Y. Nosrati, and S. H. Tavassoli, "Sinusoidal ghost imaging," *Optics Letters*, vol. 40, p. 3452, Aug. 2015.

[24] M. J. Padgett and R. W. Boyd, "An introduction to ghost imaging: Quantum and classical," *Philosophical Transactions of the Royal Society A: Mathematical, Physical and Engineering Sciences*, vol. 375, p. 20160233, Aug. 2017.

[25] P.-A. Moreau, E. Toninelli, P. A. Morris, R. S. Aspden, T. Gregory, G. Spalding, R. W. Boyd, and M. J. Padgett, "Resolution limits of quantum ghost imaging," *Optics Express*, vol. 26, p. 7528, Mar. 2018.

[26] J. Wu, Z. Xie, Z. Liu, W. Liu, Y. Zhang, and S. Liu, "Multiple-image encryption based on computational ghost imaging," *Optics Communications*, vol. 359, pp. 38–43, Jan. 2016.

[27] D.-J. Zhang, H.-G. Li, Q.-L. Zhao, S. Wang, H.-B. Wang, J. Xiong, and K. Wang, "Wavelength-multiplexing ghost imaging," *Physical Review A*, vol. 92, p. 013823, July 2015.

[28] B. I. Erkmen, "Computational ghost imaging for remote sensing," *Journal of the Optical Society of America A*, vol. 29, p. 782, Apr. 2012. https://doi.org/10.1364/JOSAA.29.000782.

[29] W. Chen and X. Chen, "Ghost imaging for three-dimensional optical security," *Applied Physics Letters*, vol. 103, p. 221106, Nov. 2013. https://doi.org/10.1063/1.4836995.

[30] Z. Sun, F. Tuitje, and C. Spielmann, "A review of high-resolution microscopic ghost imaging with a low-dose pseudothermal light," *Journal of Microscopy*, vol. 284, p. 3–11, Aug. 2021. https://doi.org/10.1111/jmi.13048.

[31] W. Gong and S. Han, "Ghost imaging lidar: principle, progress and prospect," *Journal of Optics*, vol. 26, p. 123001, Nov. 2024. https://doi.org/10.1088/2040-8986/ad8147.

[32] M.-Q. Li, R.-M. Lan, X.-F. Liu, X.-R. Yao, and G.-J. Zhai, "Acoustical ghost imaging," *Applied Physics Letters*, vol. 117, Aug. 2020. https://doi.org/10.1063/5.0015810.

[33] Z. Gao, X. Cheng, J. Yue, and Q. Hao, "Extendible ghost imaging with high reconstruction quality in strong scattering medium," *Optics Express*, vol. 30, p. 45759, Dec. 2022. https://doi.org/10.1364/oe.474579.

[34] D. Davenport, A. Eshun, B. Demory, P. Mos, L. Yang, S. Jeppson, A. Wilson, S. Kiannejad, T. Bond, M. Rushford, C. Boley, E. Charbon, C. Bruschini, and T. Laurence, "Ghost imaging using two spad array detectors: a parameter study towards the realization of a 3d quantum microscope," in *Quantum Effects and Measurement Techniques in Biology and Biophotonics* (C. Aiello, S. V. Polyakov, and P. Derr, eds.), p. 18, SPIE, Mar. 2024. https://doi.org/10.1117/12.3002965.

[35] J. H. Shapiro, "Computational ghost imaging," *Physical Review A*, vol. 78, p. 061802, Dec. 2008.

[36] Y. Zhang, Y. Zhang, C. Chang, S. Sun, and W. Liu, "Multiple description coding ghost imaging," *Frontiers in Physics*, vol. 11, p. 1277299, 2023.

[37] G. Wu, T. Li, J. Li, B. Luo, and H. Guo, "Ghost imaging under low-rank constraint," *Optics Letters*, vol. 44, no. 17, pp. 4311–4314, 2019.

[38] M. Aβmann and M. Bayer, "Compressive adaptive computational ghost imaging," *Scientific reports*, vol. 3, no. 1, p. 1545, 2013.

[39] G. M. Gibson, B. Sun, M. P. Edgar, D. B. Phillips, N. Hempler, G. T. Maker, G. P. A. Malcolm, and M. J. Padgett, "Real-time imaging of methane gas leaks using a single-pixel camera," *Optics Express*, vol. 25, p. 2998, Feb. 2017.

[40] E. Candes and M. Wakin, "An introduction to compressive sampling," *IEEE Signal Processing Magazine*, vol. 25, p. 21–30, Mar. 2008. https://doi.org/10.1109/MSP.2007.914731.

[41] T. W. Du Bosq and B. L. Preece, "Performance assessment of a single-pixel compressive sensing imaging system," in *Infrared Imaging Systems: Design, Analysis, Modeling, and Testing XXVII* (G. C. Holst and K. A. Krapels, eds.), vol. 9820, p. 98200F, SPIE, May 2016. https://doi.org/10.1117/12.2227816.

[42] W. Zhao, L. Gao, A. Zhai, and D. Wang, "Comparison of common algorithms for single-pixel imaging via compressed sensing," *Sensors*, vol. 23, p. 4678, May 2023. https://doi.org/10.3390/s23104678.

[43] A. Boccolini, A. Fedrizzi, and D. Faccio, "Ghost imaging with the human eye," *Optics Express*, vol. 27, p. 9258, Mar. 2019.

[44] G. Wang, H. Zheng, Z. Tang, Y. Zhou, H. Chen, J. Liu, Y. He, Y. Yuan, F. Li, and Z. Xu, "All-Optical Naked-Eye Ghost Imaging," *Scientific Reports*, vol. 10, p. 2493, Feb. 2020.

[45] G. Wang, H. Zheng, Z. Tang, Y. He, Y. Zhou, H. Chen, J. Liu, Y. Yuan, F. Li, and Z. Xu, "Naked-eye ghost imaging via photoelectric feedback," *Chinese Optics Letters*, vol. 18, no. 9, p. 091101, 2020.

[46] D. Pelliccia, A. Rack, M. Scheel, V. Cantelli, and D. M. Paganin, "Experimental X-Ray Ghost Imaging," *Physical Review Letters*, vol. 117, p. 113902, Sept. 2016.

[47] A.-X. Zhang, Y.-H. He, L.-A. Wu, L.-M. Chen, and B.-B. Wang, "Tabletop x-ray ghost imaging with ultra-low radiation," *Optica*, vol. 5, p. 374, Apr. 2018.

[48] R. I. Khakimov, B. M. Henson, D. K. Shin, S. S. Hodgman, R. G. Dall, K. G. H. Baldwin, and A. G. Truscott, "Ghost imaging with atoms," *Nature*, vol. 540, pp. 100–103, Dec. 2016.

[49] S. Li, F. Cropp, K. Kabra, T. J. Lane, G. Wetzstein, P. Musumeci, and D. Ratner, "Electron Ghost Imaging," *Physical Review Letters*, vol. 121, p. 114801, Sept. 2018.

[50] X. Sun, H. Chen, B. Qiu, G. Wang, W. Xu, S. Luo, Y. Yuan, B. Chen, H. Zheng, Y. He, and Z. Xu, "High-speed ghost imaging by an unpredictable optical phased array," *Frontiers in Physics*, vol. 10, p. 1072482, Dec. 2022.

[51] M. Xi, H. Chen, Y. Yuan, G. Wang, Y. He, Y. Liang, J. Liu, H. Zheng, and Z. Xu, "Bi-frequency 3D ghost imaging with Haar wavelet transform," *Optics Express*, vol. 27, p. 32349, Oct. 2019.

[52] Y. He, G. Wang, G. Dong, S. Zhu, H. Chen, A. Zhang, and Z. Xu, "Ghost Imaging Based on Deep Learning," *Scientific Reports*, vol. 8, p. 6469, Apr. 2018.

[53] T. B. Pittman, Y. H. Shih, D. V. Strekalov, and A. V. Sergienko, "Optical imaging by means of two-photon quantum entanglement," *Physical Review A*, vol. 52, pp. R3429–R3432, Nov. 1995.

[54] D.-Z. Cao and K. Wang, "Sub-wavelength interference in macroscopic observation," *Physics Letters A*, vol. 333, pp. 23–29, Nov. 2004.

[55] J. Cheng and S. Han, "Incoherent Coincidence Imaging and Its Applicability in X-ray Diffraction," *Physical Review Letters*, vol. 92, p. 093903, Mar. 2004.

[56] D. Zhang, Y.-H. Zhai, L.-A. Wu, and X.-H. Chen, "Correlated two-photon imaging with true thermal light," *Optics Letters*, vol. 30, p. 2354, Sept. 2005.

[57] Z.-H. Xu, W. Chen, J. Penuelas, M. Padgett, and M.-J. Sun, "1000 fps computational ghost imaging using LED-based structured illumination," *Optics Express*, vol. 26, p. 2427, Feb. 2018.

[58] W. Zhao, H. Chen, Y. Yuan, H. Zheng, J. Liu, Y. Zhou, and Z. Xu, "Ultra-high-speed color imaging with single-pixel detectors under low light level," *arXiv preprint arXiv:1907.09517*, 2019.

[59] Z. Zhang, X. Ma, and J. Zhong, "Single-pixel imaging by means of Fourier spectrum acquisition," *Nature Communications*, vol. 6, p. 6225, Feb. 2015.

[60] Z. Zhang, X. Wang, G. Zheng, and J. Zhong, "Hadamard single-pixel imaging versus Fourier single-pixel imaging," *Optics Express*, vol. 25, p. 19619, Aug. 2017.

[61] B. Sun, M. P. Edgar, R. Bowman, L. E. Vittert, S. Welsh, A. Bowman, and M. J. Padgett, "3D Computational Imaging with Single-Pixel Detectors," *Science*, vol. 340, pp. 844–847, May 2013.

[62] Y. Zhang, M. P. Edgar, B. Sun, N. Radwell, G. M. Gibson, and M. J. Padgett, "3D single-pixel video," *Journal of Optics*, vol. 18, p. 035203, Mar. 2016.

[63] W. Gong, C. Zhao, H. Yu, M. Chen, W. Xu, and S. Han, "Three-dimensional ghost imaging lidar via sparsity constraint," *Scientific Reports*, vol. 6, p. 26133, May 2016.

[64] M.-J. Sun, M. P. Edgar, G. M. Gibson, B. Sun, N. Radwell, R. Lamb, and M. J. Padgett, "Single-pixel three-dimensional imaging with time-based depth resolution," *Nature Communications*, vol. 7, p. 12010, July 2016.

[65] X. Liu, J. Shi, X. Wu, and G. Zeng, "Fast first-photon ghost imaging," *Scientific Reports*, vol. 8, p. 5012, Mar. 2018.

[66] F. Devaux, P.-A. Moreau, S. Denis, and E. Lantz, "Computational temporal ghost imaging," *Optica*, vol. 3, p. 698, July 2016.

[67] P. Ryczkowski, M. Barbier, A. T. Friberg, J. M. Dudley, and G. Genty, "Ghost imaging in the time domain," *Nature Photonics*, vol. 10, pp. 167–170, Mar. 2016.

[68] F. Ferri, D. Magatti, L. A. Lugiato, and A. Gatti, "Differential Ghost Imaging," *Physical Review Letters*, vol. 104, p. 253603, June 2010.

[69] B. Sun, S. S. Welsh, M. P. Edgar, J. H. Shapiro, and M. J. Padgett, "Normalized ghost imaging," *Optics Express*, vol. 20, p. 16892, July 2012.

[70] X.-R. Yao, W.-K. Yu, X.-F. Liu, L.-Z. Li, M.-F. Li, L.-A. Wu, and G.-J. Zhai, "Iterative denoising of ghost imaging," *Optics Express*, vol. 22, p. 24268, Oct. 2014.

[71] C. F. Higham, R. Murray-Smith, M. J. Padgett, and M. P. Edgar, "Deep learning for real-time single-pixel video," *Scientific Reports*, vol. 8, p. 2369, Feb. 2018.

[72] M. Lyu, W. Wang, H. Wang, H. Wang, G. Li, N. Chen, and G. Situ, "Deep-learning-based ghost imaging," *Scientific Reports*, vol. 7, p. 17865, Dec. 2017.

[73] T. Shimobaba, Y. Endo, T. Nishitsuji, T. Takahashi, Y. Nagahama, S. Hasegawa, M. Sano, R. Hirayama, T. Kakue, A. Shiraki, and T. Ito, "Computational ghost imaging using deep learning," *Optics Communications*, vol. 413, pp. 147–151, Apr. 2018.

[74] I. Goodfellow, Y. Bengio, and A. Courville, *Deep Learning*. MIT Press, 2016.

[75] M. A. W. Saduf and A. Wani, "Comparative study of back propagation learning algorithms for neural networks," *International Journal of Advanced Research in Computer Science and Software Engineering*, vol. 3, no. 12, pp. 1151–1156, 2013.

[76] N. M. Nawi, R. S. Ransing, and N. A. Hamid, "Bpgd-ag: A new improvement of back-propagation neural network learning algorithms with adaptive gain," *Journal of Science and Technology*, vol. 2, 2010. https://www.semanticscholar.org/paper/70969a09c1ddff34fd7c3f862dc340e722b85ef9.

[77] N. M. Nawi, N. A. Hamid, R. Ransing, R. Ghazali, and M. N. M. Salleh, "Enhancing back propagation neural network algorithm with adaptive gain on classification problems," *International Journal of Database Theory and Application*, vol. 4, no. 2, pp. 65–76, 2011.

[78] F. Jin and G. Shu, "Back propagation neural network based on artificial bee colony algorithm," in *2012 7th International Forum on Strategic Technology (IFOST)*, p. 1–4, IEEE, Sept. 2012. https://doi.org/10.1109/IFOST.2012.6357623.

[79] J. Jiang, J. Zhang, G. Yang, D. Zhang, and L. Zhang, "Application of back propagation neural network in the classification of high resolution remote sensing image: Take remote sensing image of beijing for instance," in *2010 18th International Conference on Geoinformatics*, p. 1–6, IEEE, June 2010. https://doi.org/10.1109/GEOINFORMATICS.2010.5568228.

[80] P. Zhang, J. Liu, C. Chen, and Y. Q. Li, "The algorithm study for using the back propagation neural network in ct image segmentation," in *International Conference on Innovative Optical Health Science* (X. Li and Q. Luo, eds.), vol. 10245, p. 102450B, SPIE, Jan. 2017. https://doi.org/10.1117/12.2267070.

[81] Q. Chen, J. Xu, and V. Koltun, "Fast image processing with fully-convolutional networks," in *Proceedings of the IEEE International Conference on Computer Vision*, pp. 2497–2506, 2017.

[82] M. Grubinger, P. Clough, H. Müller, and T. Deselaers, "The iapr tc-12 benchmark: A new evaluation resource for visual information systems," in *International Workshop ontoImage*, vol. 2, 2006.

[83] K. Zhang, W. Zuo, Y. Chen, D. Meng, and L. Zhang, "Beyond a Gaussian Denoiser: Residual Learning of Deep CNN for Image Denoising," *IEEE Transactions on Image Processing*, vol. 26, pp. 3142–3155, July 2017.

[84] L. A. Gatys, A. S. Ecker, and M. Bethge, "A neural algorithm of artistic style," *arXiv preprint arXiv:1508.06576*, 2015.

[85] J. Johnson, A. Alahi, and L. Fei-Fei, "Perceptual losses for real-time style transfer and super-resolution," in *Computer Vision–ECCV 2016: 14th European Conference, Amsterdam, the Netherlands, October 11-14, 2016, Proceedings, Part II 14*, pp. 694–711, Springer, 2016.

[86] J. Kim, J. K. Lee, and K. M. Lee, "Accurate image super-resolution using very deep convolutional networks," in *Proceedings of the IEEE Conference on Computer Vision and Pattern Recognition*, pp. 1646–1654, 2016.

[87] Y.-H. Tsai, W.-C. Hung, S. Schulter, K. Sohn, M.-H. Yang, and M. Chandraker, "Learning to adapt structured output space for semantic segmentation," in *Proceedings of the IEEE Conference on Computer Vision and Pattern Recognition*, pp. 7472–7481, 2018.

[88] R. Kemker, C. Salvaggio, and C. Kanan, "High-resolution multispectral dataset for semantic segmentation," *arXiv preprint arXiv:1703.01918*, 2017.

[89] O. Ronneberger, P. Fischer, and T. Brox, "U-net: Convolutional networks for biomedical image segmentation," in *Medical Image Computing and Computer-Assisted Intervention–MICCAI 2015: 18th International Conference, Munich, Germany, October 5-9, 2015, Proceedings, Part III 18*, pp. 234–241, Springer, 2015.

[90] R. Kemker, C. Salvaggio, and C. Kanan, "Algorithms for semantic segmentation of multispectral remote sensing imagery using deep learning," *ISPRS Journal of Photogrammetry and Remote Sensing*, vol. 145, pp. 60–77, Nov. 2018.

[91] F. Isensee, P. Kickingereder, W. Wick, M. Bendszus, and K. H. Maier-Hein, "Brain tumor segmentation and radiomics survival prediction: Contribution to the brats 2017 challenge," in *Brainlesion: Glioma, Multiple Sclerosis, Stroke and Traumatic Brain Injuries: Third International Workshop, BrainLes 2017, Held in Conjunction with MICCAI 2017, Quebec City, QC, Canada, September 14, 2017, Revised Selected Papers 3*, pp. 287–297, Springer, 2018.

[92] C. You, Q. Yang, H. Shan, L. Gjesteby, G. Li, S. Ju, Z. Zhang, Z. Zhao, Y. Zhang, W. Cong, *et al.*, "Structurally-sensitive multi-scale deep neural network for low-dose CT denoising," *IEEE access : practical innovations, open solutions*, vol. 6, pp. 41839–41855, 2018.

[93] C. Stringer, T. Wang, M. Michaelos, and M. Pachitariu, "Cellpose: A generalist algorithm for cellular segmentation," *Nature Methods*, vol. 18, pp. 100–106, Jan. 2021.

[94] S. Ren, K. He, R. Girshick, and J. Sun, "Faster r-cnn: Towards real-time object detection with region proposal networks," *Advances in neural information processing systems*, vol. 28, 2015.

[95] R. Girshick, J. Donahue, T. Darrell, and J. Malik, "Rich feature hierarchies for accurate object detection and semantic segmentation," in *Proceedings of the IEEE Conference on Computer Vision and Pattern Recognition*, pp. 580–587, 2014.

[96] Y. Wang, T. Shi, P. Yun, L. Tai, and M. Liu, "Pointseg: Real-time semantic segmentation based on 3d lidar point cloud," *arXiv preprint arXiv:1807.06288*, 2018.

[97] A. H. Lang, S. Vora, H. Caesar, L. Zhou, J. Yang, and O. Beijbom, "Pointpillars: Fast encoders for object detection from point clouds," in *Proceedings of the IEEE/CVF Conference on Computer Vision and Pattern Recognition*, pp. 12697–12705, 2019.

[98] M. Hahner, D. Dai, A. Liniger, and L. Van Gool, "Quantifying data augmentation for lidar based 3d object detection," *arXiv preprint arXiv:2004.01643*, 2020.

[99] A. Mousavi, A. B. Patel, and R. G. Baraniuk, "A deep learning approach to structured signal recovery," in *2015 53rd Annual Allerton Conference on Communication, Control, and Computing (Allerton)*, pp. 1336–1343, IEEE, Sept. 2015.

[100] K. J. Lee and B. Lee, "End-to-end deep learning architecture for separating maternal and fetal ecgs using w-net," *IEEE access : practical innovations, open solutions*, vol. 10, pp. 39782–39788, 2022.

[101] H. Zhang, M. Zhao, C. Wei, D. Mantini, Z. Li, and Q. Liu, "EEGdenoiseNet: A benchmark dataset for end-to-end deep learning solutions of EEG denoising," July 2021.

[102] M. Ravanelli and Y. Bengio, "Speaker Recognition from Raw Waveform with SincNet," in *2018 IEEE Spoken Language Technology Workshop (SLT)*, (Athens, Greece), pp. 1021–1028, IEEE, Dec. 2018.

[103] O. Ernst, S. E. Chazan, S. Gannot, and J. Goldberger, "Speech Dereverberation Using Fully Convolutional Networks," in *2018 26th European Signal Processing Conference (EUSIPCO)*, (Rome), pp. 390–394, IEEE, Sept. 2018.

[104] Y. Luo and N. Mesgarani, "Conv-TasNet: Surpassing Ideal Time–Frequency Magnitude Masking for Speech Separation," *IEEE/ACM Transactions on Audio, Speech, and Language Processing*, vol. 27, pp. 1256–1266, Aug. 2019.

[105] D. Liu, P. Smaragdis, and M. Kim, "Experiments on deep learning for speech denoising," in *Interspeech 2014*, pp. 2685–2689, ISCA, Sept. 2014.

[106] S. R. Park and J. Lee, "A Fully Convolutional Neural Network for Speech Enhancement," 2016.

[107] A. Hannun, C. Case, J. Casper, B. Catanzaro, G. Diamos, E. Elsen, R. Prenger, S. Satheesh, S. Sengupta, A. Coates, and A. Y. Ng, "Deep Speech: Scaling up end-to-end speech recognition," 2014.

[108] N. P. Jouppi, C. Young, N. Patil, D. Patterson, G. Agrawal, R. Bajwa, S. Bates, S. Bhatia, N. Boden, A. Borchers, *et al.*, "In-datacenter performance analysis of a tensor processing unit," in *Proceedings of the 44th annual international symposium on computer architecture*, pp. 1–12, 2017.

[109] A. Boutros, E. Nurvitadhi, and V. Betz, "Specializing for efficiency: Customizing ai inference processors on fpgas," in *2021 International Conference on Microelectronics (ICM)*, p. 62–65, IEEE, Dec. 2021. https://doi.org/10.1109/ICM52667.2021.9664938.

[110] Y. Hu, Y. Liu, and Z. Liu, "A survey on convolutional neural network accelerators: Gpu, fpga and asic," in *2022 14th International Conference on Computer Research and Development (ICCRD)*, pp. 100–107, IEEE, 2022.

[111] B. Ahn, "Special-purpose hardware architecture for neuromorphic computing," in *2015 International SoC Design Conference (ISOCC)*, p. 209–210, IEEE, Nov. 2015. https://doi.org/10.1109/ISOCC.2015.7401792.

[112] J. Zhou, X. He, L. Sun, J. Xu, X. Chen, Y. Chu, L. Zhou, X. Liao, B. Zhang, S. Afvari, and X. Gao, "Pre-trained multimodal large language model enhances dermatological diagnosis using SkinGPT-4," *Nature Communications*, vol. 15, p. 5649, July 2024.

[113] D. Marković, A. Mizrahi, D. Querlioz, and J. Grollier, "Physics for neuromorphic computing," *Nature Reviews Physics*, vol. 2, pp. 499–510, July 2020.

[114] J. Zhu, T. Zhang, Y. Yang, and R. Huang, "A comprehensive review on emerging artificial neuromorphic devices," *Applied Physics Reviews*, vol. 7, p. 011312, Mar. 2020.

[115] G. Wetzstein, A. Ozcan, S. Gigan, S. Fan, D. Englund, M. Soljačić, C. Denz, D. A. B. Miller, and D. Psaltis, "Inference in artificial intelligence with deep optics and photonics," *Nature*, vol. 588, pp. 39–47, Dec. 2020.

[116] Q. Xia and J. J. Yang, "Memristive crossbar arrays for brain-inspired computing," *Nature Materials*, vol. 18, pp. 309–323, Apr. 2019.

[117] L. G. Wright, T. Onodera, M. M. Stein, T. Wang, D. T. Schachter, Z. Hu, and P. L. McMahon, "Deep physical neural networks trained with backpropagation," *Nature*, vol. 601, pp. 549–555, Jan. 2022.

[118] G. Van Der Sande, D. Brunner, and M. C. Soriano, "Advances in photonic reservoir computing," *Nanophotonics*, vol. 6, pp. 561–576, May 2017.

[119] L. Butschek, A. Akrout, E. Dimitriadou, A. Lupo, M. Haelterman, and S. Massar, "Photonic reservoir computer based on frequency multiplexing," *Optics Letters*, vol. 47, p. 782, Feb. 2022.

[120] A. Lupo, E. Picco, M. Zajnulina, and S. Massar, "Fully analog photonic deep Reservoir Computer based on frequency multiplexing," *arXiv:2305.08892*, 2023.

[121] H. Nomura, K. Tsujimoto, M. Goto, N. Samura, R. Nakatani, and Y. Suzuki, "Reservoir computing with two-bit input task using dipole-coupled nanomagnet array," *Japanese Journal of Applied Physics*, vol. 59, p. SEEG02, Apr. 2020.

[122] F. Abreu Araujo, M. Riou, J. Torrejon, S. Tsunegi, D. Querlioz, K. Yakushiji, A. Fukushima, H. Kubota, S. Yuasa, M. D. Stiles, and J. Grollier, "Role of non-linear data processing on speech recognition task in the framework of reservoir computing," *Scientific Reports*, vol. 10, p. 328, Jan. 2020.

[123] L. C. G. Govia, G. J. Ribeill, G. E. Rowlands, H. K. Krovi, and T. A. Ohki, "Quantum reservoir computing with a single nonlinear oscillator," *Physical Review Research*, vol. 3, p. 013077, Jan. 2021.

[124] Q. H. Tran and K. Nakajima, "Higher-Order Quantum Reservoir Computing," 2020.

[125] C. Du, F. Cai, M. A. Zidan, W. Ma, S. H. Lee, and W. D. Lu, "Reservoir computing using dynamic memristors for temporal information processing," *Nature Communications*, vol. 8, p. 2204, Dec. 2017.

[126] L. Appeltant, M. Soriano, G. Van Der Sande, J. Danckaert, S. Massar, J. Dambre, B. Schrauwen, C. Mirasso, and I. Fischer, "Information processing using a single dynamical node as complex system," *Nature Communications*, vol. 2, p. 468, Sept. 2011.

[127] P. Antonik, *Application of FPGA to Real-Time Machine Learning: Hardware Reservoir Computers and Software Image Processing*. Springer, 2018.

[128] E. Torres, K. Nakajima, and I. S. Godage, "Information Processing Capability of Soft Continuum Arms," in *2019 2nd IEEE International Conference on Soft Robotics (RoboSoft)*, (Seoul, Korea (South)), pp. 441–447, IEEE, Apr. 2019.

[129] K. Goto, K. Nakajima, and H. Notsu, "Computing with vortices: Bridging fluid dynamics and its information-processing capability," 2020.

[130] D. Nikolić, S. Häusler, W. Singer, and W. Maass, "Distributed Fading Memory for Stimulus Properties in the Primary Visual Cortex," *PLoS Biology*, vol. 7, p. e1000260, Dec. 2009.

[131] M. R. Dranias, H. Ju, E. Rajaram, and A. M. J. VanDongen, "Short-Term Memory in Networks of Dissociated Cortical Neurons," *The Journal of Neuroscience*, vol. 33, pp. 1940–1953, Jan. 2013.

[132] T. Kubota, K. Nakajima, and H. Takahashi, "Echo State Property of Neuronal Cell Cultures," in *Artificial Neural Networks and Machine Learning – ICANN 2019: Workshop and Special Sessions* (I. V. Tetko, V. Kůrková, P. Karpov, and F. Theis, eds.), vol. 11731, pp. 137–148, Cham: Springer International Publishing, 2019.

[133] K. Nakajima and I. Fischer, eds., *Reservoir Computing: Theory, Physical Implementations, and Applications*. Natural Computing Series, Singapore: Springer Singapore, 2021.

[134] G. Tanaka, T. Yamane, J. B. Héroux, R. Nakane, N. Kanazawa, S. Takeda, H. Numata, D. Nakano, and A. Hirose, "Recent advances in physical reservoir computing: A review," *Neural Networks*, vol. 115, pp. 100–123, July 2019.

[135] L. F. Nicolas-Alonso and J. Gomez-Gil, "Brain Computer Interfaces, a Review," *Sensors*, vol. 12, pp. 1211–1279, Jan. 2012.

[136] H. H. Jasper, "The ten-twenty electrode system of the International Federation," *Electroencephalography and Clinical Neurophysiology*, vol. 10, pp. 370–375, 1958.

[137] Department of Electrical and Electronic Engineering, Assiut University, Assiut, Egypt, M. Abo-Zahhad, S. M. Ahmed, and S. N. Abbas, "A New EEG Acquisition Protocol for Biometric Identification Using Eye Blinking Signals," *International Journal of Intelligent Systems and Applications*, vol. 7, pp. 48–54, May 2015.

[138] Jinghai Yin, Derong Jiang, and Jianfeng Hu, "Design and application of brain-computer interface web browser based on VEP," in *2009 International Conference on Future BioMedical Information Engineering (FBIE)*, (Sanya, China), pp. 77–80, IEEE, Dec. 2009.

[139] D. Regan, "Human brain electrophysiology: evoked potentials and evoked magnetic fields," *Science and Medicine. New York: University of Toronto, Elsevier*, 1989.

[140] Xiaorong Gao, Dingfeng Xu, Ming Cheng, and Shangkai Gao, "A BCI-based environmental controller for the motion-disabled," *IEEE Transactions on Neural Systems and Rehabilitation Engineering*, vol. 11, pp. 137–140, June 2003.

[141] J. V. Odom, M. Bach, C. Barber, M. Brigell, M. F. Marmor, A. P. Tormene, and G. E. Holder, "Visual evoked potentials standard (2004)," *Documenta Ophthalmologica*, vol. 108, pp. 115–123, Mar. 2004.

[142] S. Nagel and M. Spüler, "World's fastest brain-computer interface: Combining EEG2Code with deep learning," *PLOS ONE*, vol. 14, p. e0221909, Sept. 2019.

[143] J. R. Wolpaw, H. Ramoser, D. J. McFarland, and G. Pfurtscheller, "Eeg-based communication: improved accuracy by response verification," *IEEE transactions on Rehabilitation Engineering*, vol. 6, no. 3, pp. 326–333, 1998.

[144] G. Bin, X. Gao, Y. Wang, B. Hong, and S. Gao, "VEP-based brain-computer interfaces: Time, frequency, and code modulations [Research Frontier," *IEEE Computational Intelligence Magazine*, vol. 4, pp. 22–26, Nov. 2009.

[145] P.-L. Lee, J.-C. Hsieh, C.-H. Wu, K.-K. Shyu, and Y.-T. Wu, "Brain computer interface using flash onset and offset visual evoked potentials," *Clinical Neurophysiology*, vol. 119, pp. 605–616, Mar. 2008.

[146] Yijun Wang, Xiaorong Gao, Bo Hong, Chuan Jia, and Shangkai Gao, "Brain-Computer Interfaces Based on Visual Evoked Potentials," *IEEE Engineering in Medicine and Biology Magazine*, vol. 27, pp. 64–71, Sept. 2008.

[147] D. Zhu, J. Bieger, G. Garcia Molina, and R. M. Aarts, "A Survey of Stimulation Methods Used in SSVEP-Based BCIs," *Computational Intelligence and Neuroscience*, vol. 2010, pp. 1–12, 2010.

[148] N. R. Galloway, "Human Brain Electrophysiology: Evoked Potentials and Evoked Magnetic Fields in Science and Medicine," *British Journal of Ophthalmology*, vol. 74, pp. 255–255, Apr. 1990.

[149] I. Minenko, V. Popova, and A. Dmitriev, "Temporal and spatial parameters dynamics of ssvep during long-term low-frequency led-stimulation: Pilot study," in *2021 Ural Symposium on Biomedical Engineering, Radioelectronics and Information Technology (USBEREIT)*, pp. 0141–0144, IEEE, 2021.

[150] W. M. Perlstein, M. A. Cole, M. Larson, K. Kelly, P. Seignourel, and A. Keil, "Steady-state visual evoked potentials reveal frontally-mediated working memory activity in humans," *Neuroscience Letters*, vol. 342, pp. 191–195, May 2003.

[151] M. Gray, A. Kemp, R. Silberstein, and P. Nathan, "Cortical neurophysiology of anticipatory anxiety: An investigation utilizing steady state probe topography (SSPT)," *NeuroImage*, vol. 20, pp. 975–986, Oct. 2003.

[152] C. C. Muth, "Eye emergencies," *JAMA*, vol. 318, p. 676, Aug. 2017. https://doi.org/10.1001/jama.2017.9899.

[153] B. Patil and T. Dowd, "Physiological functions of the eye," *Current Anaesthesia & Critical Care*, vol. 11, p. 293–298, Dec. 2000. https://doi.org/10.1054/CACC.2000.0295.

[154] L. G. Valiant, "Accidental algorthims," in *2006 47th Annual IEEE Symposium on Foundations of Computer Science (FOCS'06)*, p. 509–517, IEEE, Oct. 2006. https://doi.org/10.1109/FOCS.2006.7.

[155] D. H. Foster, "Colour vision," *Contemporary Physics*, vol. 25, p. 477–497, Sept. 1984. https://doi.org/10.1080/00107518408210723.

[156] S. M. Wu, "Synaptic transmission in the outer retina," *Annual Review of Physiology*, vol. 56, no. Volume 56,, pp. 141–168, 1994.

[157] R. A. Weale, "Observations on photochemical reactions in living eyes," *British Journal of Ophthalmology*, vol. 41, p. 461–474, Aug. 1957. https://doi.org/10.1136/bjo.41.8.461.

[158] O. Hassan, M. A. Georgeson, and S. T. Hammett, "Brightening and dimming aftereffects at low and high luminance," *Vision*, vol. 2, no. 2, p. 24, 2018.

[159] W. N. Charman, "Light on the peripheral retina," *Ophthalmic and Physiological Optics*, vol. 9, p. 91–92, Jan. 1989. https://doi.org/10.1111/j.1475-1313.1989.tb00815.x.

[160] C. Cinel, D. Valeriani, and R. Poli, "Neurotechnologies for Human Cognitive Augmentation: Current State of the Art and Future Prospects," *Frontiers in Human Neuroscience*, vol. 13, p. 13, Jan. 2019.

[161] R. Raisamo, I. Rakkolainen, P. Majaranta, K. Salminen, J. Rantala, and A. Farooq, "Human augmentation: Past, present and future," *International Journal of Human-Computer Studies*, vol. 131, pp. 131–143, Nov. 2019.

[162] Y. Lelievre, Y. Washizawa, and T. M. Rutkowski, "Single trial BCI classification accuracy improvement for the novel virtual sound movement-based spatial auditory paradigm," in *2013 Asia-Pacific Signal and Information Processing Association Annual Summit and Conference*, pp. 1–6, IEEE, Oct. 2013.

[163] A. Vourvopoulos and F. Liarokapis, "Robot Navigation Using Brain-Computer Interfaces," in *2012 IEEE 11th International Conference on Trust, Security and Privacy in Computing and Communications*, pp. 1785–1792, IEEE, June 2012.

[164] B. Van De Laar, H. Gurkok, D. Plass-Oude Bos, M. Poel, and A. Nijholt, "Experiencing BCI Control in a Popular Computer Game," *IEEE Transactions on Computational Intelligence and AI in Games*, vol. 5, pp. 176–184, June 2013.

[165] L. Bi, X.-A. Fan, and Y. Liu, "EEG-Based Brain-Controlled Mobile Robots: A Survey," *IEEE Transactions on Human-Machine Systems*, vol. 43, pp. 161–176, Mar. 2013.

[166] Wei Wang, A. D. Degenhart, G. P. Sudre, D. A. Pomerleau, and E. C. Tyler-Kabara, "Decoding semantic information from human electrocorticographic (ECoG) signals," in *2011 Annual International Conference of the IEEE Engineering in Medicine and Biology Society*, pp. 6294–6298, IEEE, Aug. 2011.

[167] J. S. Brumberg, A. Nieto-Castanon, P. R. Kennedy, and F. H. Guenther, "Brain–computer interfaces for speech communication," *Speech Communication*, vol. 52, pp. 367–379, Apr. 2010.

[168] N. Prataksita, Yi-Tseng Lin, Hung-Chyun Chou, and Chung-Hsien Kuo, "Brain-robot control interface: Development and application," in *2014 IEEE International Symposium on Bioelectronics and Bioinformatics (IEEE ISBB 2014)*, pp. 1–4, IEEE, Apr. 2014.

[169] S. N. Abdulkader, A. Atia, and M.-S. M. Mostafa, "Brain computer interfacing: Applications and challenges," *Egyptian Informatics Journal*, vol. 16, pp. 213–230, July 2015.

[170] J. R. Wolpaw, "Chapter 6 - Brain–computer interfaces," in *Neurological Rehabilitation* (M. P. Barnes and D. C. Good, eds.), vol. 110 of *Handbook of Clinical Neurology*, pp. 67–74, Elsevier, 2013.

[171] A. M. Norcia, L. G. Appelbaum, J. M. Ales, B. R. Cottereau, and B. Rossion, "The steady-state visual evoked potential in vision research: A review," *Journal of Vision*, vol. 15, p. 4, May 2015.

[172] F.-B. Vialatte, M. Maurice, J. Dauwels, and A. Cichocki, "Steady-state visually evoked potentials: Focus on essential paradigms and future perspectives," *Progress in Neurobiology*, vol. 90, pp. 418–438, Apr. 2010.

[173] Y. Tuncel, T. Başaklar, and Y. Z. Ider, "A model based investigation of the period doubling behavior in human steady-state visual evoked potentials," *Biomedical Physics & Engineering Express*, vol. 5, p. 045030, July 2019.

[174] Y.-J. Kim, M. Grabowecky, K. A. Paller, and S. Suzuki, "Differential Roles of Frequency-following and Frequency-doubling Visual Responses Revealed by Evoked Neural Harmonics," *Journal of Cognitive Neuroscience*, vol. 23, pp. 1875–1886, Aug. 2011.

[175] M. Labecki, R. Kus, A. Brzozowska, T. Stacewicz, B. S. Bhattacharya, and P. Suffczynski, "Nonlinear Origin of SSVEP Spectra—A Combined Experimental and Modeling Study," *Frontiers in Computational Neuroscience*, vol. 10, p. 129, Dec. 2016.

[176] F. Auger and P. Flandrin, "Improving the readability of time-frequency and time-scale representations by the reassignment method," *IEEE Transactions on Signal Processing*, vol. 43, pp. 1068–1089, May 1995.

[177] S. A. Fulop and K. Fitz, "Algorithms for computing the time-corrected instantaneous frequency (reassigned) spectrogram, with applications," *The Journal of the Acoustical Society of America*, vol. 119, pp. 360–371, Jan. 2006.

[178] S. D. Johnson, P.-A. Moreau, T. Gregory, and M. J. Padgett, "How many photons does it take to form an image?," *Applied Physics Letters*, vol. 116, p. 260504, June 2020.

[179] Y. Tuncel, T. Başaklar, and Y. Z. Ider, "Period doubling behavior in human steady state visual evoked potentials," *Biomedical Physics & Engineering Express*, vol. 4, p. 025024, Feb. 2018.

[180] S. Coelli, G. Tacchino, E. Visani, F. Panzica, S. Franceschetti, and A. M. Bianchi, "Higher order spectral analysis of scalp EEG activity reveals non-linear behavior during rhythmic visual stimulation," *Journal of Neural Engineering*, vol. 16, p. 056028, Sept. 2019.

[181] B. Solf, S. Schramm, M.-C. Blum, and S. Klee, "The Influence of the Stimulus Design on the Harmonic Components of the Steady-State Visual Evoked Potential," *Frontiers in Human Neuroscience*, vol. 14, p. 343, Sept. 2020.

[182] D. H. Kelly, "Frequency Doubling in Visual Responses*†," *Journal of the Optical Society of America*, vol. 56, p. 1628, Nov. 1966.

[183] F. Lopes Da Silva, A. Van Rotterdam, W. Storm Van Leeuwen, and A. Tielen, "Dynamic characteristics of visual evoked potentials in the dog. II. Beta frequency selectivity in evoked potentials and background activity," *Electroencephalography and Clinical Neurophysiology*, vol. 29, pp. 260–268, Sept. 1970.

[184] J. Roberts and P. Robinson, "Quantitative theory of driven nonlinear brain dynamics," *NeuroImage*, vol. 62, pp. 1947–1955, Sept. 2012.

[185] C. S. Herrmann, M. M. Murray, S. Ionta, A. Hutt, and J. Lefebvre, "Shaping Intrinsic Neural Oscillations with Periodic Stimulation," *The Journal of Neuroscience*, vol. 36, pp. 5328–5337, May 2016.

[186] H. Sohanian Haghighi and A. H. D. Markazi, "A new description of epileptic seizures based on dynamic analysis of a thalamocortical model," *Scientific Reports*, vol. 7, p. 13615, Oct. 2017.

[187] S. Zhang, X. Han, X. Chen, Y. Wang, S. Gao, and X. Gao, "A study on dynamic model of steady-state visual evoked potentials," *Journal of Neural Engineering*, vol. 15, p. 046010, Aug. 2018.

[188] T. M. S. Mukesh, V. Jaganathan, and M. R. Reddy, "A novel multiple frequency stimulation method for steady state VEP based brain computer interfaces," *Physiological Measurement*, vol. 27, pp. 61–71, Jan. 2006.

[189] S. Ge, Y. Jiang, M. Zhang, R. Wang, K. Iramina, P. Lin, Y. Leng, H. Wang, and W. Zheng, "SSVEP-Based Brain-Computer Interface With a Limited Number of Frequencies Based on Dual-Frequency Biased Coding," *IEEE Transactions on Neural Systems and Rehabilitation Engineering*, vol. 29, pp. 760–769, 2021.

[190] J. Mu, D. B. Grayden, Y. Tan, and D. Oetomo, "Frequency Superposition – A Multi-Frequency Stimulation Method in SSVEP-based BCIs," in *2021 43rd Annual International Conference of the IEEE Engineering in Medicine & Biology Society (EMBC)*, pp. 5924–5927, IEEE, Nov. 2021.

[191] B. dos Santos Pês, E. Oroski, J. G. Guimarães, and M. J. Bonfim, "A hammerstein–wiener model for single-electron transistors," *IEEE Transactions on Electron Devices*, vol. 66, no. 2, pp. 1092–1099, 2018.

[192] R. W. Boyd, *Nonlinear Optics*. San Diego: Academic Press is an imprint of Elsevier, 4 ed., 2019.

[193] D. Allen, A. M. Norcia, and C. W. Tyler, "Comparative Study of Electrophysiological and Psychophysical Measurement of the Contrast Sensitivity Function in Humans:," *Optometry and Vision Science*, vol. 63, pp. 442–449, June 1986.

[194] D. Chizhik, J. Ling, P. Wolniansky, R. Valenzuela, N. Costa, and K. Huber, "Multiple-input - multiple-output measurements and modeling in Manhattan," *IEEE Journal on Selected Areas in Communications*, vol. 21, pp. 321–331, Apr. 2003.

[195] M. Cheng, X. Gao, S. Gao, and D. Xu, "Design and implementation of a brain-computer interface with high transfer rates," *IEEE Transactions on Biomedical Engineering*, vol. 49, p. 1181, 2002.

[196] S. Nagel and M. Spüler, "World's fastest brain-computer interface: Combining EEG2Code with deep learning," *PLOS ONE*, vol. 14, p. e0221909, Sept. 2019.

[197] X. Chen, Y. Wang, M. Nakanishi, X. Gao, T.-P. Jung, and S. Gao, "High-speed spelling with a noninvasive brain–computer interface," *Proceedings of the National Academy of Sciences of the United States of America*, pp. E6058–E6067, 2015.

[198] J. Mu, D. B. Grayden, Y. Tan, and D. Oetomo, "Frequency set selection for multi-frequency steady-state visual evoked potential-based brain-computer interfaces," *Frontiers in Neuroscience*, vol. 16, p. 1057010, Dec. 2022.

[199] K.-K. Shyu, P.-L. Lee, Y.-J. Liu, and J.-J. Sie, "Dual-frequency steady-state visual evoked potential for brain computer interface," *Neuroscience Letters*, vol. 483, pp. 28–31, Oct. 2010.

[200] K. Koch, J. McLean, R. Segev, M. A. Freed, M. J. Berry, V. Balasubramanian, and P. Sterling, "How Much the Eye Tells the Brain," *Current Biology*, vol. 16, pp. 1428–1434, July 2006.

[201] Y. LeCun, C. Cortes, and C. J. C. Burges, "THE MNIST DATABASE of handwritten digits."

[202] S. Valipour, A. Shaligram, G. Kulkarni, *et al.*, "Spectral analysis of eeg signal for detection of alpha rhythm with open and closed eyes," *International Journal of Engineering and Innovative Technology (IJEIT)*, vol. 3, no. 6, pp. 1–4, 2013.

[203] D. A. Paskewitz, "Eeg alpha activity and its relationship to altered states of consciousness," *Annals of the New York Academy of Sciences*, vol. 296, no. 1, pp. 154–161, 1977.

[204] R. I. Goldman, J. M. Stern, J. Engel Jr, and M. S. Cohen, "Simultaneous eeg and fmri of the alpha rhythm," *Neuroreport*, vol. 13, no. 18, pp. 2487–2492, 2002.

[205] Y. Shen, N. C. Harris, S. Skirlo, M. Prabhu, T. Baehr-Jones, M. Hochberg, X. Sun, S. Zhao, H. Larochelle, D. Englund, and M. Soljačić, "Deep learning with coherent nanophotonic circuits," *Nature Photonics*, vol. 11, pp. 441–446, July 2017.

[206] J. Bueno, S. Maktoobi, L. Froehly, I. Fischer, M. Jacquot, L. Larger, and D. Brunner, "Reinforcement learning in a large-scale photonic recurrent neural network," *Optica*, vol. 5, p. 756, June 2018.

[207] M. Rafayelyan, J. Dong, Y. Tan, F. Krzakala, and S. Gigan, "Large-Scale Optical Reservoir Computing for Spatiotemporal Chaotic Systems Prediction," *Physical Review X*, vol. 10, p. 041037, Nov. 2020.

[208] G. Marcucci, D. Pierangeli, and C. Conti, "Theory of Neuromorphic Computing by Waves: Machine Learning by Rogue Waves, Dispersive Shocks, and Solitons," *Physical Review Letters*, vol. 125, p. 093901, Aug. 2020.

[209] D. Pierangeli, G. Marcucci, and C. Conti, "Photonic extreme learning machine by free-space optical propagation," *Photonics Research*, vol. 9, p. 1446, Aug. 2021.

[210] A. Lupo, L. Butschek, and S. Massar, "Photonic extreme learning machine based on frequency multiplexing," *Optics Express*, vol. 29, p. 28257, Aug. 2021.

[211] I. Oguz, J. L. Hsieh, N. Ulas Dinc, U. Teğin, M. Yildirim, C. Gigli, C. Moser, and D. Psaltis, "Programming nonlinear propagation for efficient optical learning machines," *arXiv:2208.04951*, 2022.

[212] F. Xia, Z. Wang, L. G. Wright, T. Onodera, M. M. Stein, J. Hu, P. L. McMahon, and S. Gigan, "Hardware-efficient, large-scale reconfigurable optical neural network (ONN) with backpropagation," in *AI and Optical Data Sciences IV* (K.-i. Kitayama and B. Jalali, eds.), vol. 12438, p. 8, SPIE, Mar. 2023.

[213] C. K. E. Alpaydin, "Optical Recognition of Handwritten Digits," 1998.

[214] A. Pierro, K. Heiney, S. Shrivastava, G. Marcucci, and S. Nichele, "Optimization of a Hydrodynamic Computational Reservoir through Evolution," *Proc. GECCO '23*, pp. 202–210, July 2023.

[215] R. A. Fisher, "Iris." UCI Machine Learning Repository, 1988.

[216] C. Gallicchio, A. Micheli, and L. Pedrelli, "Deep reservoir computing: A critical experimental analysis," *Neurocomputing*, vol. 268, pp. 87–99, Dec. 2017.

[217] S. Nichele and A. Molund, "Deep reservoir computing using cellular automata," *arXiv:1703.02806*, 2017.

[218] M. Goldmann, F. Köster, K. Lüdge, and S. Yanchuk, "Deep time-delay reservoir computing: Dynamics and memory capacity," *Chaos: An Interdisciplinary Journal of Nonlinear Science*, vol. 30, p. 093124, Sept. 2020.

[219] G. Marcucci, P. Caramazza, and S. Shrivastava, "A new paradigm of reservoir computing exploiting hydrodynamics," *Physics of Fluids*, vol. 35, p. 071703, July 2023.

[220] M. Kelly, R. Longjohn, and K. Nottingham, "The UCI machine learning repository."

[221] G.-B. Huang, Q.-Y. Zhu, and C.-K. Siew, "Extreme learning machine: Theory and applications," *Neurocomputing*, vol. 70, pp. 489–501, Dec. 2006.